

**SELF-DISCHARGE OF CARBON MATERIALS-BASED
ELECTROCHEMICAL CAPACITORS**

by

Qing Zhang

A dissertation submitted to the Faculty of the University of Delaware in partial fulfillment of the requirements for the degree of Doctor of Philosophy in Mechanical Engineering

Spring 2014

© 2014 Qing Zhang
All Rights Reserved

UMI Number: 3631223

All rights reserved

INFORMATION TO ALL USERS

The quality of this reproduction is dependent upon the quality of the copy submitted.

In the unlikely event that the author did not send a complete manuscript and there are missing pages, these will be noted. Also, if material had to be removed, a note will indicate the deletion.



UMI 3631223

Published by ProQuest LLC (2014). Copyright in the Dissertation held by the Author.

Microform Edition © ProQuest LLC.

All rights reserved. This work is protected against unauthorized copying under Title 17, United States Code



ProQuest LLC.
789 East Eisenhower Parkway
P.O. Box 1346
Ann Arbor, MI 48106 - 1346

**SELF-DISCHARGE OF CARBON MATERIALS-BASED
ELECTROCHEMICAL CAPACITORS**

by

Qing Zhang

Approved:

Suresh G. Advani, Ph.D.
Chair of the Department of Mechanical Engineering

Approved:

Babatunde A. Ogunnaike, Ph.D.
Dean of the College of Engineering

Approved:

James G. Richards, Ph.D.
Vice Provost for Graduate and Professional Education

I certify that I have read this dissertation and that in my opinion it meets the academic and professional standard required by the University as a dissertation for the degree of Doctor of Philosophy.

Signed:

Bingqing Wei, Ph.D.
Professor in charge of dissertation

I certify that I have read this dissertation and that in my opinion it meets the academic and professional standard required by the University as a dissertation for the degree of Doctor of Philosophy.

Signed:

Joshua Hertz, Ph.D.
Member of dissertation committee

I certify that I have read this dissertation and that in my opinion it meets the academic and professional standard required by the University as a dissertation for the degree of Doctor of Philosophy.

Signed:

Ajay K. Prasad, Ph.D.
Member of dissertation committee

I certify that I have read this dissertation and that in my opinion it meets the academic and professional standard required by the University as a dissertation for the degree of Doctor of Philosophy.

Signed:

Chaoying Ni, Ph.D.
Member of dissertation committee

ACKNOWLEDGMENTS

There are many experiences that I remember of the last five years. I want to give thanks with my whole heart for all the encouragement and help that carried me through.

First of all, I want to thank Dr. Bingqing Wei, my advisor of the PhD program, for giving me the opportunity to study and research in electrochemistry. I am grateful for his mentorship, enduring help and guidance over the last five years.

I would like to thank Dr. Joshua Hertz, Dr. Chaoying Ni, and Dr. Ajay Prasad for serving my committee for the PhD candidacy defense and now the PhD dissertation defense. They have provided valuable discussion and suggestions for my project. I want to thank Dr. Suresh Advani for choosing me as his teaching assistant for the two courses, “Thermodynamics” and “Heat Transfer”. I am grateful for his recognition. I would like to thank the US National Science Foundation (NSF) and the Semiconductor Research Corporation (SRC) for funding.

I would like to thank my professional friends and colleagues, and the post-doctorate and visiting scholars in Dr. Wei’s group for their help and accompaniment throughout my graduate life. I want to thank Mr. Jiepeng Rong for training me using the lab equipment and answering my questions. I want to thank Dr. Jinwen Qin for teaching me how to make the graphene samples and being one of my best friends during her one-year visit at the University of Delaware. I want to thank Ms. Kathryn Scrafford for her help with the graphene oxide film preparation. I want to thank Mr.

Taoli Gu, Mr. Zeyuan Cao, Mr. Xin Li, Mr. Kun Liang and Dr. Changsheng Shan for helping me in the lab and providing useful discussion.

I would like to thank my collaborators, Prof. Pulickel M. Ajayan, and Dr. Wei Gao from Rice University, and Prof. Dongsheng Ma from University of Texas at Dallas, for their contribution and helping in this dissertation. Especially, I want to thank Prof. Zhenhai Xia and Dr. Mingtao Li for their excellent modeling work which helped us interpret the experiment observations. I would like to thank Dr. Fei Deng, Mr. Frank Kriss for teaching me the TEM, SEM, AFM and FIB. I want to thank Dr. Guangjin Hou, Mr. Zachary Voras, Mr. Robert Forest, Mr. Trong Pham, and Mr. Steven Sauerbrunn for their kindness and help with characterizing my samples using various techniques such as NMR, XPS, BET, TGA, etc. I would like to thank Mr. Roger Stahl for helping me with instrument problems in our lab, especially for his help on setting up the laser equipment. I would like to thank Mr. Steven L. Beard for his help with the equipment in the machine shop. I would like to thank the administrative staff from Department of Mechanical Engineering, especially Ms. Lisa M. Katzmire, Ms. Letitia Toto, Ms. Ann Conor for answering my questions and helping me adapt to the graduate life, Ms. Corinne Hamed from the Center for Composite Materials for helping me on obtaining the access to the equipments in the center.

I want to thank all my dear friends, Ms. Yue Wu, Ms. Yingying Ye, Ms. Jie Fu, Ms. Qing Sun, and Mr. Zheng Chen for their accompaniment during my graduate life. I want to thank my dear cousin Mengxue Huang for always being the dearest sister of mine. I want to thank Mr. Ke Xiong, for his love and support. Finally, I want to thank my dearest, dearest parents, for their unconditional love and care.

To all these and many more, thank you!

DEDICATION

To my late maternal grandfather Zeyu Wang.

TABLE OF CONTENTS

| | |
|--------------------------------------------------------------------------------|-------|
| LIST OF TABLES | xi |
| LIST OF FIGURES | xii |
| LIST OF ABBREVIATIONS | xviii |
| ABSTRACT | xx |
| Chapter | |
| 1 INTRODUCTION | 1 |
| 1.1 General | 1 |
| 1.2 Electrochemical Capacitors | 2 |
| 1.2.1 Brief history of electrochemical capacitors | 2 |
| 1.2.2 Principle of electrochemical capacitors | 4 |
| 1.2.3 Double layer models in ECs | 5 |
| 1.2.4 Electrodes and electrolytes for ECs | 8 |
| 1.3 Self-discharge in ECs | 13 |
| 1.3.1 Driving forces of self-discharge | 14 |
| 1.3.2 Mechanisms of self-discharge | 15 |
| 1.3.3 Influencing factors of self-discharge | 16 |
| 1.4 Dissertation Scope | 17 |
| REFERENCES | 20 |
| 2 SELF-DISCHARGE IN ACTIVATED CARBON BASED ELECTROCHEMICAL CAPACITORS | 24 |
| 2.1 Introduction | 24 |
| 2.2 Activated Carbon | 24 |
| 2.3 Experimental Section | 26 |
| 2.3.1 Sample preparation and EC assembly | 26 |
| 2.3.2 Electrochemical testing | 27 |
| 2.4 Results and Discussion | 28 |

| | | |
|------------------|-----------------------------------------------------------------------------------------------------------------------------------------------|----|
| 2.4.1 | Self-discharge curves with organic electrolyte: 1M LiPF ₆ in EC:DEC | 28 |
| 2.4.2 | Self-discharge curves with organic electrolyte: 1M TEABF ₄ in PC | 30 |
| 2.4.3 | Self-discharge models | 32 |
| 2.4.3.1 | Diffusion control model for ACF-LiPF ₆ (EC:DEC)..... | 32 |
| 2.4.3.2 | Dual mechanism model of ACF-TEABF ₄ (PC) | 35 |
| 2.4.3.3 | Self-discharge at extended temperature range..... | 38 |
| 2.5 | Conclusions | 39 |
| REFERENCES | | 42 |
| 3 | SELF-DISCHARGE OF SINGLE-WALLED CARBON NANOTUBE BASED ELECTROCHEMICAL CAPACITORS | 44 |
| 3.1 | Introduction | 44 |
| 3.2 | Single-walled Carbon Nanotube..... | 45 |
| 3.3 | Experimental Section..... | 46 |
| 3.3.1 | Sample preparation and EC assembly | 46 |
| 3.3.2 | Self-discharge testing | 48 |
| 3.4 | Results and Discussion | 49 |
| 3.4.1 | Self-discharge curves..... | 49 |
| 3.4.2 | Self-discharge model | 50 |
| 3.4.2.1 | Divided potential driving model and single potential driving model..... | 52 |
| 3.4.2.2 | Origins of the divided potential driving model | 54 |
| 3.4.2.3 | Self-discharge at extended temperature range..... | 56 |
| 3.5 | Conclusions | 57 |
| REFERENCES | | 59 |
| 4 | TUNING SELF-DISCHARGE: EFFECTS OF FUNCTIONAL GROUPS ON SELF-DISCHARGE OF SINGLE-WALLED CARBON NANOTUBE BASED ELECTROCHEMICAL CAPACITORS | 61 |
| 4.1 | Introduction | 61 |
| 4.2 | Functional Groups | 62 |
| 4.3 | Experimental Section..... | 65 |

| | | |
|------------|---------------------------------------------------------------------------------------------------|-----|
| 4.3.1 | Sample preparation | 65 |
| 4.3.2 | Sample characterizations | 65 |
| 4.3.3 | Self-discharge testing | 66 |
| 4.4 | Results and Discussion | 67 |
| 4.4.1 | SWNT microstructure and chemical identification analysis | 67 |
| 4.4.2 | Tuning self-discharge | 72 |
| 4.4.3 | Electrochemical impedance spectroscopy | 76 |
| 4.4.4 | Cyclic voltammetry | 78 |
| 4.5 | Conclusions | 79 |
| REFERENCES | | 81 |
| 5 | SELF-DISCHARGE OF GRAPHENE BASED ELECTROCHEMICAL CAPACITORS | 84 |
| 5.1 | Introduction | 84 |
| 5.2 | Graphene..... | 85 |
| 5.3 | Experimental Section..... | 87 |
| 5.3.1 | Sample preparation | 87 |
| 5.3.2 | Near infrared laser workstation set-up | 88 |
| 5.3.3 | Characterizations and electrochemical testing | 90 |
| 5.4 | Results and Discussion | 90 |
| 5.4.1 | Microstructure and composition analysis | 90 |
| 5.4.2 | Electrochemical Capacitive behaviors of the LR-GO EC | 95 |
| 5.4.3 | Self-discharge behaviors of the LR-GO EC | 97 |
| 5.4.4 | Electrochemical impedance spectroscopy | 99 |
| 5.5 | Conclusions | 100 |
| REFERENCES | | 102 |
| 6 | ANOMALOUS CAPACITIVE BEHAVIORS OF ALL SOLID-STATE GRAPHENE BASED ELECTROCHEMICAL CAPACITORS | 105 |
| 6.1 | Introduction | 105 |
| 6.2 | ECs and DCs..... | 105 |
| 6.3 | Experimental Section..... | 107 |
| 6.3.1 | Sample preparation | 107 |

| | | |
|----------|---------------------------------------------------------------------------------------------------|-----|
| 6.3.2 | Lightscribing reduction | 108 |
| 6.3.3 | Characterizations of the GO films and the sandwiched GO films..... | 109 |
| 6.3.4 | Electrochemical characterizations of the sandwiched GO films..... | 110 |
| 6.3.5 | Measurement of dielectric constant for the GO films | 111 |
| 6.3.6 | Measurement on the humidity effects | 111 |
| 6.3.7 | Simulation on the water structures and charge distribution in the gap of two graphene sheets..... | 112 |
| 6.4 | Results and Discussion | 114 |
| 6.4.1 | Microstructure and chemical identification analysis..... | 114 |
| 6.4.1.1 | Microstructure: AFM, TEM and SEM..... | 114 |
| 6.4.1.2 | Dielectric constant of the GO film | 116 |
| 6.4.1.3 | XRD, TGA and Raman | 117 |
| 6.4.2 | Electrochemical performances | 119 |
| 6.4.2.1 | Galvanostatic charge/discharge | 119 |
| 6.4.2.2 | Electrochemical impedance spectroscopy..... | 121 |
| 6.4.3 | Solid state NMR spectroscopy | 123 |
| 6.4.4 | Modeling on the charge structure | 126 |
| 6.4.5 | Charge Close-Packed model..... | 130 |
| 6.5 | Conclusions | 131 |
| | REFERENCES..... | 133 |
| 7 | CONCLUSION AND FUTURE WORK..... | 136 |
| 7.1 | Summary of the Research Contributions..... | 136 |
| 7.2 | Future Work..... | 138 |
| Appendix | | |
| A | SCIENTIFIC AND TECHNICAL CONTRIBUTIONS DURING PH.D. | 141 |
| B | AWARDS DURING PH.D. | 142 |
| C | PERMISSION LETTERS | 143 |

LIST OF TABLES

| | | |
|------------|------------------------------------------------------------------------------------------------------------------------------------|-----|
| Table 1.1. | Properties and characteristics of various carbon materials as electrode materials for ECs. | 10 |
| Table 2.1 | Parameters of the self-discharge testing. | 28 |
| Table 2.2. | Specific capacitances of the ACF-LiPF ₆ EC. | 33 |
| Table 2.3 | Specific capacitances of the ACF-TEABF ₄ EC. | 37 |
| Table 3.1 | Specific capacitances of the SWNT-TEABF ₄ EC. | 51 |
| Table 3.2 | Self-discharge parameters under different charge current densities. | 52 |
| Table 4.1 | Atomic percentage concentrations of r-SWNT, SWNT and o-SWNT based on XPS survey. | 68 |
| Table 4.2 | Atomic percentage concentrations of various carbon functional groups of r-SWNT, SWNT, and o-SWNT based on XPS curve fittings. | 70 |
| Table 4.3 | Three types of ECs: r-SWNT, SWNT, and o-SWNT ECs and their self-discharge fitting parameters. | 75 |
| Table 5.1 | Characterization results of the GO films and LR-GO films. | 93 |
| Table 5.2 | Fitting parameters calculated based on the DPD to SPD model. | 98 |
| Table 6.1 | Specific capacitance for the sandwiched GO Film, calculated from CV curves. | 121 |
| Table 6.2. | Fitting Parameters of the Equivalent Circuit for EIS data. | 122 |

LIST OF FIGURES

| | | |
|------------|--------------------------------------------------------------------------------------------------------------------------------------------------------------------------------------------------------------------------------------------------------------------------------------------------------------------------|----|
| Figure 1.1 | Charge storage models for (a) the EDLC and (b) the pseudocapacitor..... | 4 |
| Figure 1.2 | Models of the double layer on the positively charged electrode surface. (a) Helmholtz model of compact layers of charges; (b) Gouy-Chapman model with thermal fluctuation; and (c) Stern-Grahame model. (ψ_0 and ψ_s are the potential at the electrode side and the solution side of the double layer) | 6 |
| Figure 1.3 | Schematic of the structure of charged EC with two double layer structures. | 8 |
| Figure 1.4 | Atomic structures of three main types of carbon materials as electrode materials of ECs and their common microstructures: activated carbon (a), (d), with permission from ref. 36 (Appendix C: 1); carbon nanotubes (b), (e), with permission from ref. 37 (Appendix C: 2); and graphene (c), (f)..... | 10 |
| Figure 1.5 | Illustration on the self-discharge process. (Note: ΔE —potential field; $\partial c/\partial x$ —concentration gradient of ions) | 13 |
| Figure 2.1 | Common forms of AC materials (a) powders of AC; (b) fibers of AC... | 26 |
| Figure 2.2 | (a) Schematic of the assembled ECs with ACF-LiPF ₆ and ACF-TEABF ₄ structure; (b) Galvanostatic self-discharge testing after two and a half cycle of charging/discharging of the assembled ECs. | 27 |
| Figure 2.3 | Self-discharge curves of the ACF-LiPF ₆ EC system under different charge current densities I_C at 25 °C, the inset is the initial voltage versus I_C | 29 |
| Figure 2.4 | Relations on initial voltage and diffusion parameter versus the charge current density I_C | 29 |
| Figure 2.5 | Self-discharge curves of the ACF-TEABF ₄ EC under different charge current densities I_C at 25 °C, the inset is the initial voltage versus I_C | 31 |
| Figure 2.6 | Decrease in voltage after 36 hours of self-discharge for the ACF-TEABF ₄ EC..... | 31 |

| | | |
|-------------|------------------------------------------------------------------------------------------------------------------------------------------------------------------------------------------------------------------------------------------------------------------------------------------------------------------------------------------------------------------------------------------------------------------------------------------------------------------|----|
| Figure 2.7 | (a) Self-discharge curves of the ACF-LiPF ₆ EC versus $t^{1/2}$; (b) Fitting the self-discharge curves with Diffusion control model for the ACF-LiPF ₆ EC..... | 33 |
| Figure 2.8 | Energy barrier E_b for ionic diffusion at different charge current densities I_C | 34 |
| Figure 2.9 | Self-discharge curves of the ACF-TEABF ₄ EC fitted by: (a) diffusion control model $V \propto e^{-t}$; and (b) potential driving model $V \propto t^{1/2}$ | 35 |
| Figure 2.10 | Self-discharge curves of the ACF-TEABF ₄ EC fitted by the proposed dual mechanism control model: (a) $I_C=25 \text{ mA}\cdot\text{g}^{-1}$ and (b) $I_C=500 \text{ mA}\cdot\text{g}^{-1}$. Note: Black curve: original; Red: $V \propto e^{-t}$; Blue: $V \propto t^{1/2}$. Fitting has been preformed for all charge current densities, $25 \text{ mA}\cdot\text{g}^{-1}$ and $500 \text{ mA}\cdot\text{g}^{-1}$ are shown here as examples. | 36 |
| Figure 2.11 | Self-discharge behaviors at different temperatures with charge current density of $I_C=100 \text{ mA}\cdot\text{g}^{-1}$: (a) the ACF-LiPF ₆ EC at -25°C, 25°C, 75°C; (b) the ACF-TEABF ₄ EC at -25°C, 25°C, 75°C; (c) Fitting with the diffusion control model for the ACF-LiPF ₆ EC at -25°C and 75°C; (d) Fitting by the DM model for the ACF-TEABF ₄ EC at -25°C and 75°C. | 38 |
| Figure 3.1 | Schematic of (a) SWNTs and (b) MWNTs; (c) TEM image of SWNTs, with permission from ref. 17 (Appendix C: 3); (d) TEM image of MWNTs, with permission from ref. 18 (Appendix C: 4)..... | 46 |
| Figure 3.2 | Schematic of (a) the CVD synthesis of SWNTS and (b) the EC assembly. | 47 |
| Figure 3.3 | Illustration of the self-discharge testing: (a) two and a half cycle charging/discharging, followed by (b) the self-discharge process. | 48 |
| Figure 3.4 | Self-discharge curves with charge current densities I_C from 10 to 1000 $\text{mA}\cdot\text{g}^{-1}$ at 25 °C; the inset shows the zoom-in at the beginning of the self-discharge..... | 49 |
| Figure 3.5 | Fitting results of the self-discharge curves with (a) the diffusion control model: $V \propto -t^{1/2}$ and (b) the potential driving model: $V \propto e^{-t/\tau}$ | 51 |
| Figure 3.6 | Self-discharge curves (black) fitted with the DPD model: (red) and single potential driving model (blue). Note: Selected self-discharge curves with 10, 100, and 1000 $\text{mA}\cdot\text{g}^{-1}$ are presented)..... | 52 |

| | | |
|------------|-----------------------------------------------------------------------------------------------------------------------------------------------------------------------------------------------------------------------------------------------------------------|----|
| Figure 3.7 | Illustration of the functional groups interference on interactions between the electrolytic ions and the charged electrode. | 54 |
| Figure 3.8 | Self-discharge curves (black) fitted with the DPD model (red) and the SPD model (blue), (a) at 75 °C and (b) at -25 °C. | 56 |
| Figure 4.1 | Structure of carbon surface with various functional groups..... | 62 |
| Figure 4.2 | (a) Schematic of the structures of the built ECs, each with r-SWNT, SWNT, and o-SWNT as electrodes, and 1M TEABF ₄ (PC) as electrolyte; (b) The self-discharge experiments after two and a half cycles of charging/discharging. | 66 |
| Figure 4.3 | SEM images taken on (a) SWNT; (b) r-SWNT after heat treatment; and (c) o-SWNT after oxidation treatment..... | 67 |
| Figure 4.4 | XPS survey of 400 °C heat-treated SWNT (r-SWNT, cyan), as-prepared SWNT (SWNT, orange), and KMnO ₄ -oxidized SWNT (o-SWNT, maroon). | 68 |
| Figure 4.5 | C 1s binding energy (BE) regions of (a) r-SWNT; (b) SWNT; and (c) o-SWNT. All spectra were calibrated by setting the main peak in the C 1s BE region to the sp ² -hybridized carbons at 284.5 eV. | 69 |
| Figure 4.6 | (a) Raman spectra over r-SWNT, SWNT, and o-SWNT; varied intensity ratio: <i>ID/IG</i> indicates structural changes. (b) TGA curves of the three SWNT samples: r-SWNT, SWNT, and o-SWNT. Results are shown within the temperature range from 100 to 1000 °C..... | 71 |
| Figure 4.7 | Self-discharge curves (black) of the r-SWNT EC, the SWNT EC, and the o-SWNT EC and fitting results: red by the DPD model and blue by the SPD model at room temperature (a, c, e) and -25 °C (b, d, f). | 73 |
| Figure 4.8 | (a) EIS spectra at room temperature and (b) Bode phase plot at room temperature (solid lines) and at -25 °C (lines starred with “◇”, “Δ”, “□”) of r-SWNT (cyan), SWNT (orange) and o-SWNT (maroon). (c) Corresponding equivalent circuits. | 77 |
| Figure 4.9 | CV curves of r-SWNT (cyan), SWNT (orange) and o-SWNT (maroon) at the scan rate of 10 mV·s ⁻¹ | 78 |
| Figure 5.1 | Schematic of the fabrication of graphene oxide films..... | 88 |

| | | |
|------------|------------------------------------------------------------------------------------------------------------------------------------------------------------------------------------------------------------------------------------------------------------------------------------------------------------------------------------------------------------------------------------------------------------------------------------------------------------------------------------------------------------|-----|
| Figure 5.2 | (a) Schematic representation of the laser workstation for GO film reduction. (b) Digital camera image of LR-GO film after laser reduction and punched into 13 mm in diameter. | 89 |
| Figure 5.3 | Digital camera images taken of (a) the parts of the test cell and (b) the assembled test cell. | 89 |
| Figure 5.4 | (a) SEM image of GO surface before (yellow box) and after (cyan box) laser reduction. (b) Zoom-in SEM view on the unreduced area; (c) Zoom-in SEM view on the reduced area. | 91 |
| Figure 5.5 | (a) SEM image of the cross sectional view of the GO film before (yellow box) and after (cyan box) laser reduction; (b) Zoom-in SEM view on the unreduced part; (c) Zoom-in SEM view on the reduced part, which shows a much expanded structure; (d) XEDS results collected on randomly picked areas on the surface and cross-section of the GO and the LR-GO films; (e) Raman spectra collected on the GO and LR-GO films. | 92 |
| Figure 5.6 | (a) XPS survey of the GO film and the LR-GO film; C 1s binding energy (BE) regions of (b) the GO film and (c) the LR-GO film. | 94 |
| Figure 5.7 | (a) Galvanostatic charge/discharge curves and (b) the corresponding charge/discharge energy densities of the LR-GO EC with an charge current density of $0.2 \text{ mA}\cdot\text{g}^{-1}$. (c) CV curves of the LR-GO EC with different scan rate from 10 to 100 mV s^{-1} | 96 |
| Figure 5.8 | Self-discharge curves of the LR-GO films, with charge current density of $0.2 \text{ mA}\cdot\text{g}^{-1}$, (a) self-discharge after two and a half cycle of charge/discharge; (b) self-discharge after holding the voltage at 0.5 V for 12 hours following the two and a half cycle of charge/discharge. | 98 |
| Figure 5.9 | (a) EIS spectra and (b) the Bode Phase plot of the LR-GO film. | 100 |
| Figure 6.1 | Schematics of charge storage mechanisms. (a) The EC, which stores energy through ionic diffusion under electrostatic attraction to form one or two atomic layers of compact electrolytic ions followed by a relatively uncondensed diffusion layer. (b) The DC, where dipoles in dielectric polarize under external potential field. (c) The GO-capacitor with the sandwiched structure of rGO/GO/rGO that behaves abnormally, where ions exist in the system yet without detectable ionic diffusion. | 106 |

| | | |
|-------------|------------------------------------------------------------------------------------------------------------------------------------------------------------------------------------------------------------------------------------------------------------------------------------------------------------------------------------------------------------------------------------------------------------------------|-----|
| Figure 6.2 | Schematic flow of sandwiched GO film fabrication: (a) the lightscribing DVD disk with aluminum foil attached on and the GO (aq). (b) Drop-casting GO (aq) onto the aluminum foil; (c) Air drying of the GO films..... | 108 |
| Figure 6.3 | Schematic of the lightscribing process..... | 109 |
| Figure 6.4 | Molecular structure of water, H, and O confined along z-direction perpendicular to the graphene or GO sheets, in two rGO sheets (a), in one rGO and one GO sheets (b) and in two GO sheets (c). | 113 |
| Figure 6.5 | (a) AFM image of the GO samples on silicon wafers; (b) TEM images of the reduced GO with slightly wrinkles. | 114 |
| Figure 6.6 | SEM images of the top-views of (a) GO film and (b) the sandwiched GO capacitor film. Cross-sectional view of (c) the GO film and (d) the sandwiched GO capacitor film. The thickness of the GO intralayer (indicated by the red arrow) is $\sim 9 \mu\text{m}$ | 115 |
| Figure 6.7 | C-V curve measured on the GO film and the gold-sputtering GO film. | 116 |
| Figure 6.8 | (a) XRD characterization of the GO film and GO-capacitor film. (b) XEDS analysis of the sandwiched GO film; (c) Raman spectra for the GO film and the sandwiched GO film, featuring five peaks. (d) TGA analysis from 100°C to 1000°C on the GO film and the sandwiched GO film. The TGA results prove a decrease in functional groups and water molecules in the sandwiched GO film..... | 118 |
| Figure 6.9 | (a) The galvanostatic charge/discharge cycles ($200 \text{ mA}\cdot\text{g}^{-1}$) of the GO-capacitor; (b) The corresponding specific capacitance for charging/discharging. (c) Self-discharge curve measured after two and a half charge/dishcharge cycles (from 0 V to 0.5 V) with an charge current density of $200 \text{ mA}\cdot\text{g}^{-1}$; (d) CV cycles from 0 to 0.5 V with different scan rates..... | 120 |
| Figure 6.10 | Nyquist plot of the GO capacitor film from 3 MHz to 10 mHz, giving two semicircles (fitted with the equivalent circuit above) without diffusion. The diffusion is typical for ECs and is represented by the Warburg line at a low frequency. | 122 |
| Figure 6.11 | Solid-state ^{13}C single pulse (SP) MAS NMR spectra of GO film sample and the capacitor film sample at 10 kHz, confirms the existence of various functional groups..... | 123 |

| | | |
|-------------|-----------------------------------------------------------------------------------------------------------------------------------------------------------------------------------------------------------------------------------------------------------------------------------------------------------------------------------------------------------------------------------------------------------------------------------------------------------------------------------------------------------------------------------------------------------------------------------------------------------------------------------------------------------------------------------------------------------------------------------------|-----|
| Figure 6.12 | Solid-state ^1H NMR spectra of GO film sample and the sandwiched film sample at 10 kHz, confirms the existence of waters and various functional groups. | 124 |
| Figure 6.13 | CV scanning of the sandwiched GO film before the humidity treatment, right after the 30 days' humidity treatment and ten days in the open air after the humidity treatment. | 126 |
| Figure 6.14 | Molecular structures and charge distributions. a-c, Molecular structures of water confined within (a) two rGO sheets, (b) one GO and one rGO sheets, and (c) two GO sheets. d-f, Charge distributions (excluding the charge on graphene) along z-direction perpendicular to graphene plane under an external electrical field (E , unit $\text{V}\cdot\text{mm}^{-1}$), showing in (d), (e) and (f) correspond to the rGO, rGO/GO, and GO systems, respectively. g, Three parts of the EIS equivalent circuit assigned to the rGO surface, the GO/rGO interface, and the GO intralayer according to the calculated parameters (Table. 6.4.2.2.1), the electrochemical performance is the collective result of all three parts. | 127 |

LIST OF ABBREVIATIONS

| | |
|------|----------------------------------------|
| AC | Activated carbon |
| ACF | Activated carbon fiber |
| AFM | Atomic force microscopy |
| BET | Brunauer-Emmett-Teller |
| CNT | Carbon nanotubes |
| CV | Cyclic voltammetry |
| CVD | Chemical vapor deposition |
| DC | Dielectric capacitor |
| DEC | Diethyl carbonate |
| DM | Dual mechanism |
| DMC | Dimethyl carbonate |
| DPD | Divided potential driving |
| DVD | Digital video disc |
| EC | Electrochemical capacitor |
| eC | Ethylene carbonate |
| EDLC | Electrochemical double layer capacitor |
| EIS | Electrochemical impedance spectroscopy |
| GO | Graphene oxide |
| LR | Laser reduced |
| MWNT | Multiwalled carbon nanotube |

NIR Near infrared
NMR Nuclear magnetic resonance
PC Propylene carbonate
rGO Reduced graphene oxide
SEM Scanning electron microscopy
SPD Single potential driving
SSA Specific surface area
SWNT Single-walled carbon nanotube
TEABF₄ Tetraethyl ammonium tetrafluoroborate
TEM Transmission electron microscopy
TGA Thermal gravimetric analysis
XEDS Energy-dispersive X-ray spectroscopy
XPS X-ray photoelectron spectroscopy
XRD X-ray diffraction

ABSTRACT

Suffering from poor energy retention, electrochemical capacitors (ECs), with exceptional power capability and long-term cyclability compared to batteries, have rarely been considered as an energy storage device that can store energy enduringly. To develop ECs as a competitive alternative to batteries, it is critical and necessary to realize control over ECs' self-discharge for desired energy retention. This dissertation focuses on the fundamental research of the energy retention of ECs and covers the pioneering progress made in establishing self-discharge mechanisms, realizing tunable self-discharge and making further insights into capacitive behaviors of ECs beyond self-discharge.

Fundamentals on self-discharge mechanisms have been explored and concluded on ECs built with three typical carbon materials: one-dimensional single-walled carbon nanotubes (SWNT), two-dimensional graphene oxide (GO), and three-dimensional activated carbon fibers (ACF), and electrolytes in liquid and solid forms. Our research indicates that ECs' structures determine the relative strength between the two self-discharge driving forces: the potential field ΔE and the concentration gradient $\partial c/\partial x$, and eventually affect the self-discharge mechanisms. For the ACF-LiPF₆ EC with a high specific capacitance (i.e., high $\partial c/\partial x$) and relatively poor charge transportation (i.e., low ΔE), its self-discharge is driven by $\partial c/\partial x$ and obeys the diffusion control model; for the SWNT-TEABF₄ EC with good charge transportation and a relatively low specific capacitance, its self-discharge is driven by ΔE and obeys the potential driving model; and for the ACF-TEABF₄ EC with the

two comparable driving forces, the dual mechanism (DM) model has been proposed. The proposed self-discharge mechanism is extendable to GO based solid-state ECs as well. On the other hand, environmental factors such as temperature have no effects on self-discharge mechanisms though these factors can affect the discharge rate of the self-discharge process.

Besides the self-discharge mechanisms, the ACF-TEABF₄ EC exhibits excellent energy retention where up to 70% of the initial voltage is retained after 36 hours of self-discharge. This energy retaining time would be desirable for the daily chargeable electronic devices. Moreover, a divided potential driving process has been discovered on the SWNT-TEABF₄ EC and confirmed to be related to the functional groups of the SWNT surface. Through tailoring the functional groups on the SWNT surface, tuning of the self-discharge has been realized for the first time. This breakthrough will offer a facile and feasible solution to the appeal for capacitor components with specialized energy retention in electric circuit designs.

Anomalous phenomenon has been observed on the GO based solid-state ECs, which contradicts the conventional understanding of both ECs and dielectric capacitors (DCs). From systematical characterizations and modeling calculations, the Charge Close-Packed model has been proposed, featuring periodical layers of charges as well as nanoscaled ionic diffusion and well explaining the contradiction between considerable energy density and undetectable ionic diffusion observed on this GO based EC.

Chapter 1

INTRODUCTION

1.1 General

Environmental issues and limited sources of fossil fuels lead to growing demands in exploring other energy sources, such as wind energy, solar energy and hydropower, as substitutes. However, these energy sources need to be harvested and converted into the form of electricity prior to use, raising enormous needs for energy storage devices represented by rechargeable batteries and electrochemical capacitors (ECs) for storage and consumption of electrical energy. Meanwhile, as a result of a burgeoning market for portable electronic devices and the development of hybrid electric vehicles and electric vehicles, there has been increasing demand for the development of energy storage devices with superior performance[1-3].

Currently, lithium-ion batteries are considered as one of the most qualified energy supply in electronic devices[4]. Suffering from the intrinsic non-reversible redox reaction of lithium insertion/extraction, the development of lithium-ion batteries, however, has been always challenged by unavoidable slow power delivery and fast degradation in energy density[1, 4, 5]. On the other hand, ECs, based on the double layer charge storage mechanisms (see Sections 1.2.3 and 1.3), provide a solution to the stability issue faced by lithium-ion batteries. The double layer structures grant ECs high power densities and ultra-long lifespan up to millions of charge/discharge cycles. Hence, in terms of reliability, ECs become much more favorable than batteries, especially in applications that require fast power delivery[2,

4]. However, the physisorption feature of double layer structures also results in the poor energy retention of ECs, which poses ECs' application in energy storage. Unlike batteries, ECs tend to lose energy fast once disconnected from the external circuit due to the fast kinetics of ionic diffusion out of the double-layer structures. Therefore, ECs have rarely been considered as energy storage/supply like batteries, but more like a "pulse supply" or an electric signal filter because of their poor retainability of energy.

Previous research on ECs has been focused on improving the energy and power densities[6-9] or manipulating the ECs' structures[10-12], with little attention paid on fundamentals of the self-discharge process. Our study on the self-discharge process of ECs not only fills the blank on the fundamentals of self-discharge process with the proposed self-discharge mechanisms for various carbon based EC systems (see Chapters 2, 3, and 5), but also provides guidance in controlling the self-discharge (Chapter 4) and therefore, explores the potential of ECs as a competing alternative or even substituent to batteries in specific fields of applications.

1.2 Electrochemical Capacitors

An EC, also called a supercapacitor or ultracapacitor, stores energy in the "double layer" structures (Section 1.2.3) at the electrode/electrolyte interface, primarily in porous carbon materials with a high surface area. ECs have two main types, depending on the occurrence of redox reactions, one is called electrochemical double-layer capacitors (EDLCs) and the other is pseudocapacitors.

1.2.1 Brief history of electrochemical capacitors

Ever since the first dielectric capacitor (DC) in 1745, the principle that electrical energy can be stored in a cell has been introduced and utilized for practical

purposes such as power supply filters, particularly applied in the applications such as pulse power generation[2, 13-15] or signal processing[16, 17]. The first DC on record is the Leyden jar, where charges were stored on the two metal surfaces separated by a layer of glass, and the glass served as a dielectric. The dielectric is the electrical insulating materials that can be polarized under electric field, and the energy in DCs is stored through the dielectric polarization. Dielectric materials with high dielectric constants are required to achieve the high energy density in DCs. Higher dielectric constant means that more energy is required to fully polarize the dipoles in the dielectrics; therefore, more energy will be stored in the process of dielectric polarization. Typical dielectric materials are ceramics, composites of ceramics in polymer matrix, etc. Detailed information on the charge storage differences between DCs and ECs is discussed in Section 6.2.

The concept of EDLCs was described in 1957 by Becker in his granted patent, where the capacitance is related to the charge accumulation on the electrode/electrolyte interfaces. Carbon based materials are the primarily used electrode materials for EC fabrication[1, 3, 14]. Introduction of double layer has radically enhanced capacitors' energy density, comparing to dielectric capacitors (DCs). Taking an average capacitance value of $25 \mu\text{F}/\text{cm}^2$ and a specific surface area (SSA) of $1000 \text{ m}^2/\text{g}$ for carbon based electrodes[14, 18, 19], the ideal attainable energy at 1 V operating potential would reach 250 kJ/kg, comparable to the energy density of lithium-ion batteries.

The other type of ECs is pseudocapacitors, which was firstly introduced and developed by Conway during the years from 1975 to 1981 with solid oxide redox systems, especially the system comprised of RuO_2 films, in which H_2SO_4 (aq) as

electrolyte gave the best electrochemical performance[20, 21]. Faradaic redox reactions are involved in pseudocapacitance. Large capacitance up to hundreds of farads can be obtained for the EDLCs and pseudocapacitors and they are called “the ECs” collectively.

1.2.2 Principle of electrochemical capacitors

The fundamental difference between charge storage mechanisms of EDLCs and pseudocapacitors is the involvement of charge transfer. As shown in Figure 1.1a, the process of charging and discharging in the EDLC is non-Faradaic, where energy is stored through electrostatic accumulation of positive and negative charges on electrode/electrolyte interface with opposite charge (details will be discussed in Section 1.2.3). While in pseudocapacitors (Figure 1.1b), chemisorption of ions/molecules on the electrode/electrolyte interface occurs where partial charge transfer happens between the electroactive species and results in variations in their chemical states, analogous to the faradaic redox reactions in a battery.

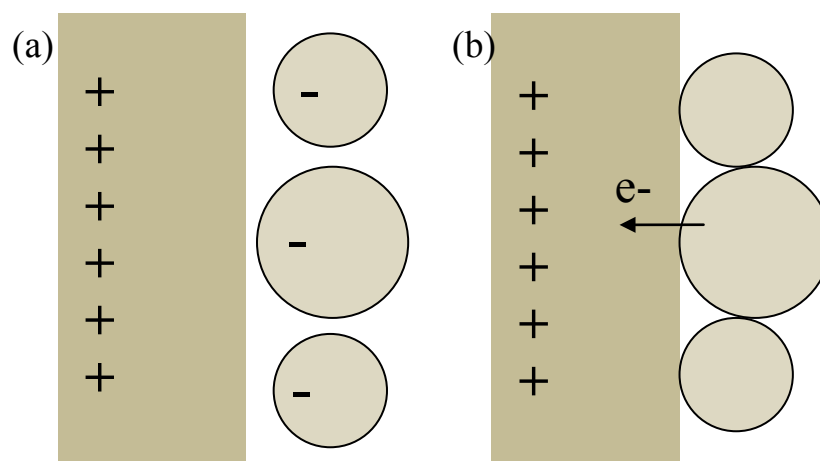


Figure 1.1 Charge storage models for (a) the EDLC and (b) the pseudocapacitor.

Though pseudocapacitance is unavoidable for carbon based ECs due to the existence of functional groups (see Chapter 4), administrative controls such as glove-box assembling, employing organic electrolytes with high voltage windows, and running the assembled capacitors within the voltage windows, can be applied to minimize pseudocapacitance in carbon based ECs. Effects of pseudocapacitance on self-discharge processes are therefore negligible on our carbon-based ECs, given that the pseudocapacitance only takes up less than 5% of the total energy stored in EDLCs[18]. This dissertation will focus on the self-discharge study in EDLCs and ECs will stand for ECs based on double layers in the rest of the dissertation except stated otherwise.

1.2.3 Double layer models in ECs

To describe the structure at the electrode/electrolyte interface in ECs, series of models have been proposed progressively, approaching to an accurate definition. The development of the double-layer model experienced three major phases, from the Helmholtz's model (of quasi-2-dimensional static compact distribution of opposite charges separated with atomic distance on the interface), to the introduction of thermal fluctuation by the Gouy-Chapman model, and to the Stern-Grahame model.

As shown in Figure 1.2a, the Helmholtz model depicts for the first time the concept of the double layer, where compact layers of charges forming on the electrode/electrolyte interface. There are two layers of charges, one on the electrode surface side and one on the electrolyte side, separated with a distance of atomic scale. The charges on the electrolyte side of double layer come from the electrolytic ions and balance the excess or deficit charges on the electrode side. In the Helmholtz model, charges in the double layers are assumed to be static. In the Gouy-Chapman model

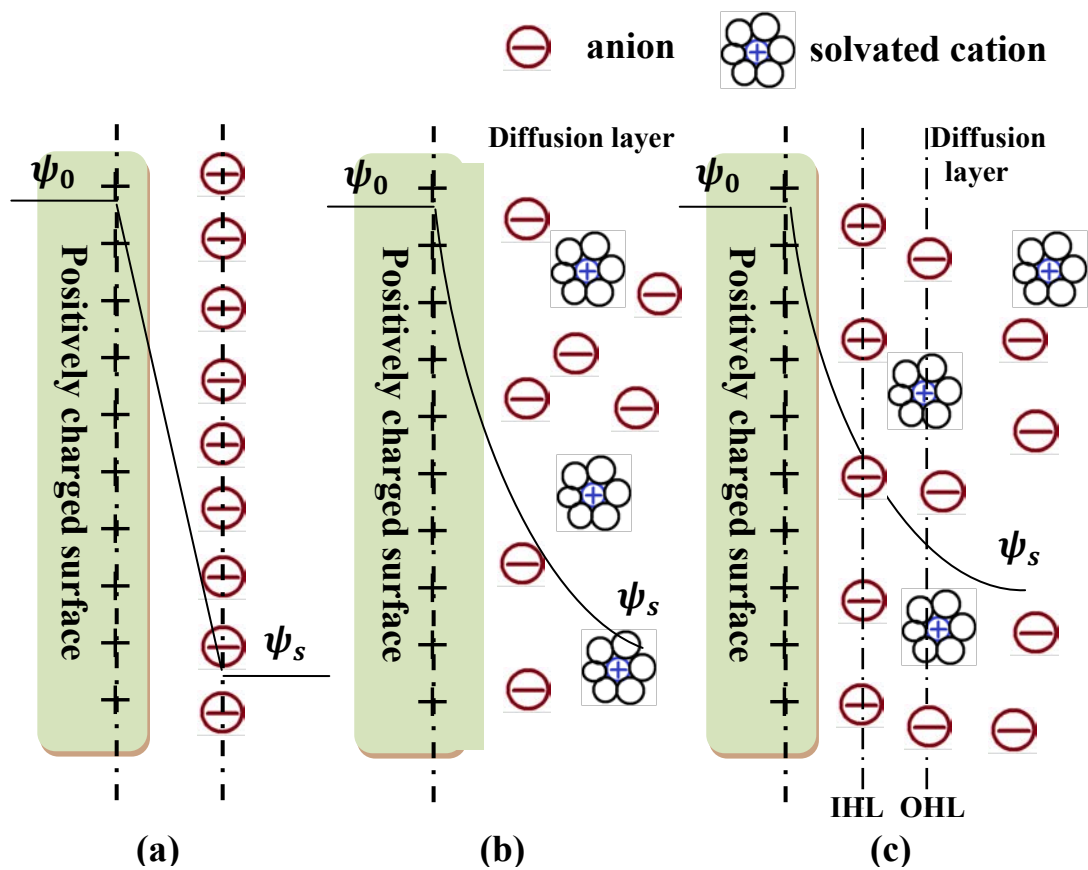


Figure 1.2 Models of the double layer on the positively charged electrode surface. (a) Helmholtz model of compact layers of charges; (b) Gouy-Chapman model with thermal fluctuation; and (c) Stern-Grahame model. (ψ_0 and ψ_s are the potential at the electrode side and the solution side of the double layer)

(Figure 1.2b), thermal fluctuation factor has been introduced into the double layer that ions will diffusively distribute in the double layer with a concentration gradient. However, the Gouy-Chapman model fails to define the distance between counterions to the oppositely charged electrode surface, and leads to an enormous overestimation of the capacitance achievable by the double layer. The Stern-Grahame model (Figure

1.2c) on the double-layer structure combines the compact structures of charges of the Helmholtz model and the diffuse region due to the thermodynamic movements of electrolytic ions as described in the Gouy-Chapman model. Moreover, the concept of the closest approach of ions to the electrode surface was introduced in the Stern-Grahame model, which led to the distinction of inner Helmholtz layer (IHL) and outer Helmholtz layer (OHL), given the smaller distances of closest approach of anions than the distance of closest approach of solvated cations. Hence, the double-layer structure consists of three distinguishable regions: the inner Helmholtz layer, the outer Helmholtz layer, and a diffusion layer. The Stern-Grahame model has remained a good basis for interpretations of the electrode interface phenomena so far.

Due to the large SSA and the atomic range of the charge separation distance, ECs based on double-layer structures can store energy of several orders higher in magnitude than that of conventional electric capacitor, even though they are both electrostatic in origin. However, when comparing the charge densities stored from electrostatic reactions to that from the Faradaic redox reactions, the double-layer capacitance is only up to 0.17-0.20 electrons per atom of the accessible surface, substantially lower than up to 2.5 electrons per atom of the accessible atoms of the electroactive material of pseudocapacitors or 1 to 3 electrons per atom of the bulk phase in batteries[18]. The energy densities of ECs based on double layers usually fall around $5 \text{ Wh}\cdot\text{kg}^{-1}$ while it is up to $100 \text{ Wh}\cdot\text{kg}^{-1}$ for batteries. On the other hand, without kinetic restrictions of chemical reactions, the power delivery of the ECs is much faster with a power density of $(5-10) \text{ kW}\cdot\text{kg}^{-1}$, which is up to 20 times higher than that of lithium ion batteries[22].

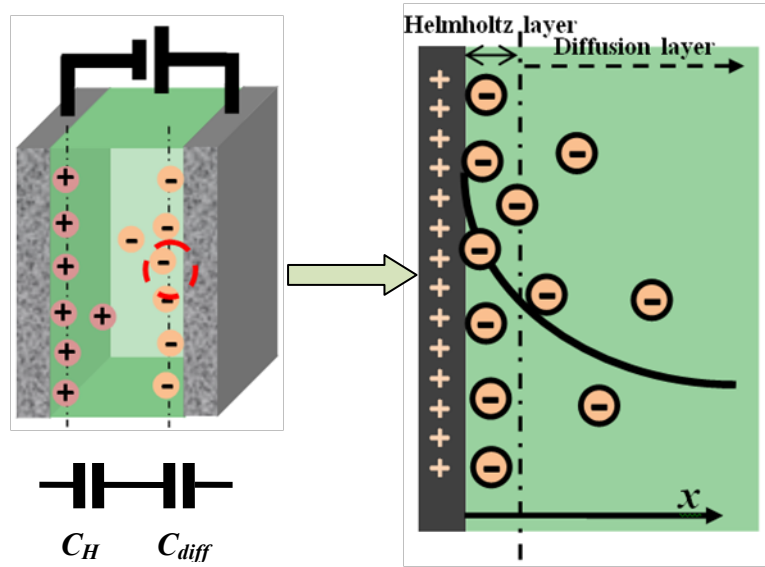


Figure 1.3 Schematic of the structure of charged EC with two double layer structures.

An EC must employ two such double-layer structures (Figure 1.3), one on each electrode/electrolyte interface, working against each other on charging, discharging or self-discharging. Moreover, the overall double-layer capacitance C_{dl} is the collective result of the conjugated components C_H of the Helmholtz layer and C_{diff} of the diffusion layer:

$$\frac{1}{C_{dl}} = \frac{1}{C_H} + \frac{1}{C_{diff}} \quad \text{-----} \quad 1.1$$

1.2.4 Electrodes and electrolytes for ECs

Energy density and power delivery capability are the two major criteria for evaluating the electrochemical performances of an EC. In order to achieve an excellent performance, electrode materials with a high SSA accessible to electrolytic ions and

superior charge transportation within the cell as well as a robust chemical stability for reliable operation are highly preferred for designing ECs[3, 14, 23]. Electrode materials with a high SSA (accessible to the electrolyte ions) provide high energy densities because increasing the electrode/electrolyte interface can provide more areas for forming double-layer structures. Capability of charge transportation is comprised of three major parts: the conduction of electrons (holes) in the electrode bulk, the ionic transportation within the electrolyte, and the charge transfer on the electrode/electrolyte interface; superior charge transportation is critical for high rate power delivery. Chemical stability is particularly important for ECs since most electrolytes are either acidic or basic. Conclusively, high SSA, good electrical conductivity, and chemical inertness are the three critical requisites to choose electrode materials for designing an EC.

Carbon-based materials are the most widely used electrode materials in ECs due to their suitable physical and chemical properties. These properties include low cost[24], facile processing, controllable porosity[25-27], electrochemical stability and variety of forms[14] (powders, fibers, fabrics, aerogels, composites, etc). Well established physical[28, 29] or chemical methods[30, 31] ensure feasible control on structural properties of carbon materials, such as micro-texture[25, 32] and surface area, for adapting to an chosen electrolyte for optimum performance in electrochemistry. Moreover, carbon materials admit stable behaviors in an extended temperature range, from subzero to 100 °C or even higher[19, 33-35], demonstrating their reliability. Excellent adaptability and versatility of carbon-based materials contribute to their outstanding electrochemical performance in terms of both power density and energy density.

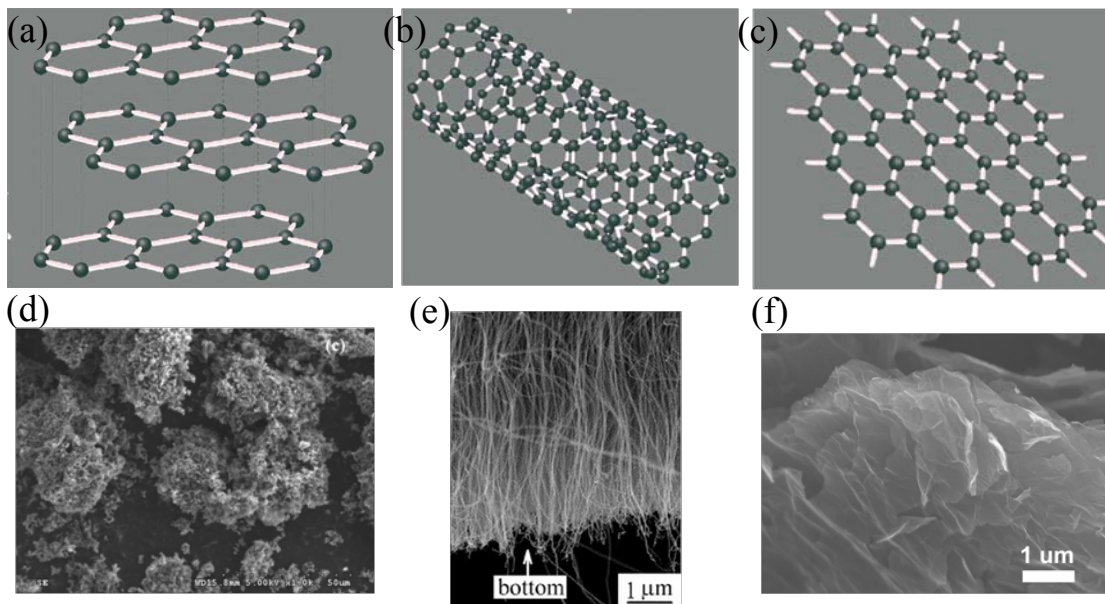


Figure 1.4 Atomic structures of three main types of carbon materials as electrode materials of ECs and their common microstructures: activated carbon (a), (d), with permission from ref. 36 (Appendix C: 1); carbon nanotubes (b), (e), with permission from ref. 37 (Appendix C: 2); and graphene (c), (f).

Table 1.1. Properties and characteristics of various carbon materials as electrode materials for ECs.

| Materials | Specific surface area | Electrical conductivity | Specific capacitance ($F \cdot g^{-1}$) | |
|------------------|-----------------------|-------------------------|-------------------------------------------|---------------------|
| | $m^2 \cdot g^{-1}$ | $S \cdot m^{-1}$ | Aqueous electrolyte | Organic electrolyte |
| Activated carbon | 1000-3000 | 10-100 | 74-250[36, 38] | 90-160 |
| Carbon nanotubes | 400-600 | 500-7200 | 50-100 | <60 |
| Graphene | 705-3100 | 200-1738 | 100-205 | 80-276 |

From the electrochemical point of view, carbon materials exhibit good polarizability. The potential voltage window of carbon for almost ideal polarizability is 1.0 V in an aqueous solution and possibly up to 3.5 V in a non-aqueous media[18], which is perfect for the self-discharge study of ECs with double-layer capacitance. There are various forms of carbon-based materials, ranging from fullerenes, nanotubes, and graphene to graphite; from zero to three-dimensional structures. The most commonly studied carbon materials for ECs are activated carbon (AC), carbon nanotubes (CNT), and reduced graphene oxide (rGO). Their atomic structures and typical morphologies are given in Figure 1.4, together with collected data on their capacitive performance and physical properties (Table 1.1) based on literature survey. AC has a three-dimensional porous structure. The SSA of AC is high as a result of activation; therefore, ECs built with AC commonly admit high specific capacitances. On the other hand, CNT, known as the representative one-dimensional carbon material, has a relatively low SSA but an excellent electrical conductivity. ECs built with CNTs as electrodes exhibit high power densities compared to ECs built with AC. Graphene has a high SSA and excellent electrical conductivity, combining the advantages of the AC and CNT and has drawn extensive research interest in electrochemistry and other fields recently. The three typical carbon materials are chosen for the self-discharge studies and the results will be discussed in details in the Chapter 2, 3 and 5, respectively.

In parallel to electrode materials, electrolytes, as an indispensable source of ions in ECs, hold an important role in ECs' performance as well. Electrolytes are prepared from dissolving inorganic or organic salts in liquid or solid-state solvents such as water, organic solvents or polymers; meanwhile, there is another type of

solvent-free electrolyte, ionic liquids. Ionic liquids are the room temperature molten salts and highly favorable for high temperature EC applications[1].

The working voltage of an EC is normally restricted by the decomposition voltage of the chosen electrolyte. Based on the states of matters, except for the solvent-free ionic liquids, electrolytes can be divided into liquid solution-based electrolytes and solid polymer-based electrolytes. Liquid solution-based electrolytes can be further divided into aqueous electrolytes and organic electrolytes. The most used aqueous electrolytes are acidic electrolyte such as H_2SO_4 (aq), basic electrolyte such as NaOH (aq), and neutral electrolyte such as KCl (aq) and KNO_3 (aq). The operational voltage window for all aqueous electrolytes should be lower than 1.2 V as the water will decompose above that voltage. As for organic electrolytes, tetraethyl ammonium tetrafluoroborate (TEABF_4) is one of the mostly common used salts, and can be dissolved in organic solutions such as polycarbonate (PC), ethylene carbonate (eC), diethyl carbonate (DEC), dimethyl carbonate (DMC), and their mixture. The organic electrolytes can greatly enhance the energy density as the operational voltage window of organic electrolytes can be up to 4.0 V and correspondingly, the energy stored increases with the square of the charged voltage. Polymer electrolytes are ion conducting composites, developed by incorporating ionic liquid or other salts into polymer matrices. Typical polymer electrolytes are aluminum chloride in 1-butylpyridinium halides[39], and non-chloroaluminate in PVDF-HEP and NAFION membranes[40]. Polymer electrolytes can withstand a high voltage window like organic liquid electrolytes, and therefore, increase the energy density.

Ionic mobility affects the self-discharge significantly because self-discharge is intrinsically a diffusion process of ions. In this dissertation, organic electrolytes are

chosen due to their high voltage window which can eliminate possible pseudocapacitance. On the other hand, in order to investigate the effects of different ionic mobilities, an all solid-state GO based EC has also chosen due to its restricted ionic mobility (see Chapters 2 and 5).

1.3 Self-discharge in ECs

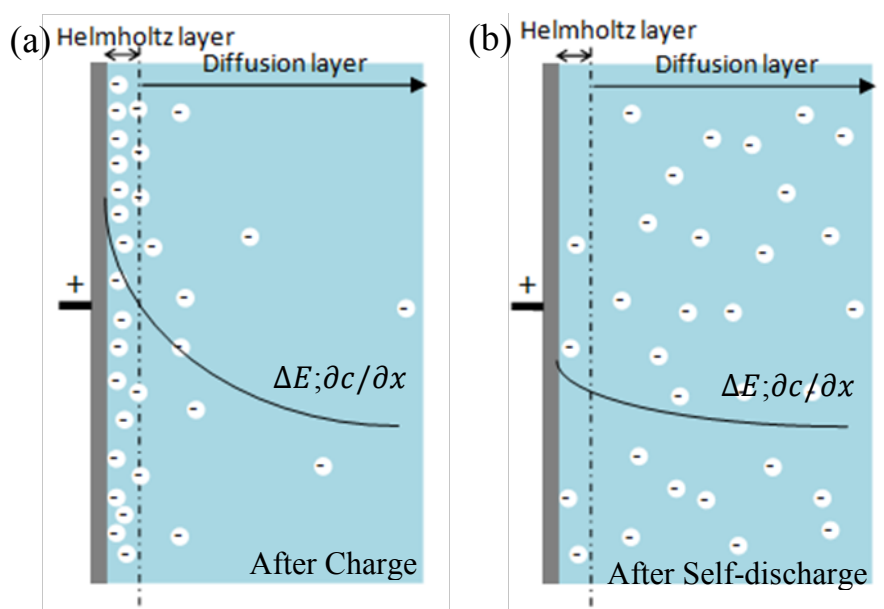


Figure 1.5 Illustration on the self-discharge process. (Note: ΔE —potential field; $\partial c / \partial x$ —concentration gradient of ions)

As shown in the Figure 1.5a, when charging ECs, electrolytic ions with opposite charges become separated and form double layer structures on the opposing electrode/electrolyte interface, respectively; the process reverses when discharging. Similar to discharge, self-discharge also involves ionic diffusion out of the double

layers, but under no external electrical field and proceeds spontaneously. After self-discharge, ions distribute evenly (Figure 1.5b) across the two opposing electrode/electrolyte interfaces.

From the view of thermodynamics, charged EC systems are at the state of non-equilibrium and prone to self-discharge to the state of equilibrium through releasing the charged electric energy. Hence, self-discharge is a spontaneous phenomenon of thermodynamics. From the view of kinetics, the self-discharge is a physical process as there is no Faradaic redox reaction, *i.e.*, ideally no electron transfer takes place across the electrode/electrolyte interface. Conclusively, self-discharge in ECs is a spontaneous electric energy diminishing process once withdrawing the external electrical field, where ions diffuse out of the double layers until the system reaches its thermodynamic equilibrium.

1.3.1 Driving forces of self-discharge

During the charging process, internal potential field ΔE and concentration gradient field $\partial c/\partial x$ will be built up as the ions accumulate onto the electrode/electrolyte interfaces and form the double-layer structures. It is worthy of reiterating that adsorption (charging) and desorption (discharging or self-discharge) of ions are electrostatic and physical in ECs; no Faradaic leakage or electron transfer through the electrode/electrolyte interface occurs. Therefore, there are two types of driving forces for the self-discharge process in ECs: one is the potential field ΔE and the other is the ionic concentration gradient $\partial c/\partial x$. These driving forces are built up during charging, and gradually fade as discharge or self-discharge proceeds.

1.3.2 Mechanisms of self-discharge

The energy diminishing of self-discharge is usually described by measuring the voltage decrease with time.

Self-discharge of conventionally DCs obeys the potential driving model with leakage over an ohmic resistance:

$$V = V_{initial} \times e^{-t/RC} \quad \text{-----} \quad 1.2 [41]$$

where V is the voltage of the capacitor, $V_{initial}$ is the initial voltage from which self-discharge starts, R is the ohmic equivalent load resistance, and C is the capacitance of the capacitor. Their self-discharge processes are solely driven by the potential field and without any involvement of ions. Usually, the self-discharge process of this type of capacitors will complete in the scale of microseconds, indicating a negligible energy retention in DCs. The time constant $\tau = RC$ is the intrinsic characteristic of a DC and determines its self-discharge rate. $t = \tau$ corresponds to the time required for the voltage to decrease to 37% of the initial voltage (as $e^{-1} = 0.37$).

In ECs, the involvement of ions makes the self-discharge process more complicated. Not only the potential field ΔE exists, the field of ionic concentration gradient $\partial c / \partial x$ also exists. Different mechanisms exist for self-discharge process driven by different driving forces.

Theoretically, for the self-discharge process driven by the potential field ΔE , the voltage decreases exponentially to time, similar to that of DCs:

$$V \propto e^{-t/\tau} \quad \text{-----} \quad 1.3$$

While, for the self-discharge process driven by the concentration gradient $\partial c/\partial x$, the voltage decreases to the square root of time:

$$V \propto -t^{1/2} \quad \text{-----} \quad 1.4$$

Previous work have only pointed out that the self-discharge process of ECs cannot be wholly ascribed to the leakage resistance model as in the DCs[41], however, few analytical results or mechanism models have been presented so far. Dominant driving force for a certain self-discharge process can be affected by many factors. For example, self-discharge of the activated carbon fabric (ACF)-TEABF₄ EC is governed with the dual mechanism (DM) model, where its self-discharge process is firstly dominated by ΔE and then switched to be driven by $\partial c/\partial x$ (see Chapter 2). The structure of an EC system, *i.e.*, the choice of electrode material and electrolyte, determines the self-discharge mechanism.

1.3.3 Influencing factors of self-discharge

The electrochemical performance of ECs, such as the energy density or power density, greatly depends on both internal and external factors. Internal factors include the electrode morphology, the surface chemistry of electrode and the wettability of electrode in electrolyte, etc. External factors include the charge current density and the operational temperature, etc. Similarly, the self-discharge process of ECs can also be influenced by those factors. Surface chemistry, charge current density and self-discharge temperature will be covered in the dissertation to discuss their effects on the self-discharge.

1.4 Dissertation Scope

This dissertation focuses on the self-discharge study of carbon based ECs, including research on fundamental self-discharge mechanisms concluded on the ECs with various electrode/electrolyte structures, tuning on self-discharge, and some new insights of the capacitive behaviors of the GO-based ECs.

AC is a commercial material for EC construction because of its high controllable SSA. Extensive work has been done on AC based ECs to improve its energy density, mostly, through increasing its SSA and surface functionalities; nevertheless, little knowledge has been gained on its self-discharge behavior. In Chapter 2, ECs built with ACF (one typical form of AC) and two different organic electrolytes: 1M LiPF₆(EC:DEC) and 1M TEABF₄(PC), have been assembled to study their self-discharge behaviors. The experimental results and systematical analysis conclude with two distinct self-discharge models, demonstrating the effects of electrolytes on determining the self-discharge mechanisms.

Another carbon material of great interests for ECs is SWNT, which has an excellent electric conductivity and a relatively high SSA. Chapter 3 presents the self-discharge study on ECs built with SWNT and 1M TEABF₄(PC). The SWNT-TEABF₄ EC is well described by a different self-discharge model compared to that of the ACF-TEABF₄ EC, indicating that the self-discharge mechanisms depend on the electrode materials as well. The study of the SWNT-TEABF₄ ECs also reveals an interesting phenomenon related to the surface functional groups on SWNT and it leads to tuning of the self-discharge process as discussed in detail in Chapter 4.

Functional groups can alter the chemical states of carbon materials, and can influence the surface chemistry of SWNT and eventually affect the electrochemical performance of ECs. However, no research has been done before to study the effects

of functional groups on self-discharge. Based on the observations in Chapter 3, SWNT samples with different amounts of functional groups have been prepared to study their self-discharge behaviors in Chapter 4. This work further demonstrates and well-explains our proposed self-discharge model for SWNT based ECs in Chapter 3 and is also the first demonstration on tuning self-discharge.

As a relatively new member of carbon material family, the potential of graphene for EC applications has already been demonstrated. In order to study the effects of limited ionic mobility of electrolytes on self-discharge, ECs fabricated on GO films in an all solid state are chosen as a perfect candidate. In Chapter 5, these all solid-state GO based ECs are fabricated using near infrared (NIR) laser. With the special layering structure and restricted ionic mobility, the as-prepared ECs admit considerable energy densities and a potential driving self-discharge mechanism. Combining the self-discharge studies in Chapter 2 and 3, Chapter 5 demonstrates the self-discharge mechanisms are determined by the competition of the driving forces.

Anomalous capacitive behaviors have been noticed during research in solid-state GO based ECs which challenges the conventional understandings in categorizing electric capacitors. Considerable capacitance can be obtained but no diffusion is observed in this type of ECs. Chapter 6 describes the systematically designed work to tackle the issue and a “Charge Close-Packed model” is proposed, which is different from the energy storage mechanisms of the conventional ECs and DCs. The model indicates that the total energy storage in the all solid state sandwiched GO based EC results from a nanoscaled ionic diffusion and packed layers of charges due to the nanoscaled diffusion. The observations will contribute to a more comprehensive understanding in the fundamentals of electric capacitors.

Chapter 7 concludes the thesis with a summary and a brief outlook towards future work and potential applications of self-discharge research.

REFERENCES

- [1] Simon, P. and Y. Gogotsi, *Materials for electrochemical capacitors*. Nature materials, 2008. **7**(11): p. 845-854.
- [2] Miller, J.R. and P. Simon, *Electrochemical capacitors for energy management*. Science Magazine, 2008. **321**(5889): p. 651-652.
- [3] Zhang, L.L. and X. Zhao, *Carbon-based materials as supercapacitor electrodes*. Chemical Society Reviews, 2009. **38**(9): p. 2520-2531.
- [4] Burke, A., *Ultracapacitors: why, how, and where is the technology*. Journal of power sources, 2000. **91**(1): p. 37-50.
- [5] Tarascon, J.-M. and M. Armand, *Issues and challenges facing rechargeable lithium batteries*. Nature, 2001. **414**(6861): p. 359-367.
- [6] Rudge, A., et al., *Conducting polymers as active materials in electrochemical capacitors*. Journal of Power Sources, 1994. **47**(1): p. 89-107.
- [7] Fischer, A.E., et al., *Incorporation of homogeneous, nanoscale MnO₂ within ultraporous carbon structures via self-limiting electroless deposition: implications for electrochemical capacitors*. Nano Letters, 2007. **7**(2): p. 281-286.
- [8] Kierzek, K., et al., *Electrochemical capacitors based on highly porous carbons prepared by KOH activation*. Electrochimica Acta, 2004. **49**(4): p. 515-523.
- [9] Wu, Z.S., et al., *High-energy MnO₂ nanowire/graphene and graphene asymmetric electrochemical capacitors*. Acs Nano, 2010. **4**(10): p. 5835-5842.
- [10] Park, J.H. and O.O. Park, *Hybrid electrochemical capacitors based on polyaniline and activated carbon electrodes*. Journal of Power Sources, 2002. **111**(1): p. 185-190.
- [11] El-Kady, M.F., et al., *Laser scribing of high-performance and flexible graphene-based electrochemical capacitors*. Science, 2012. **335**(6074): p. 1326-1330.
- [12] Yu, C., et al., *Stretchable supercapacitors based on buckled single-walled carbon-nanotube macrofilms*. Advanced Materials, 2009. **21**(47): p. 4793-4797.

- [13] Huggins, R.A., *Supercapacitors and electrochemical pulse sources*. *Solid State Ionics*, 2000. **134**(1): p. 179-195.
- [14] Frackowiak, E. and F. Beguin, *Carbon materials for the electrochemical storage of energy in capacitors*. *Carbon*, 2001. **39**(6): p. 937-950.
- [15] Chu, A. and P. Braatz, *Comparison of commercial supercapacitors and high-power lithium-ion batteries for power-assist applications in hybrid electric vehicles: I. Initial characterization*. *Journal of power sources*, 2002. **112**(1): p. 236-246.
- [16] Ottman, G.K., et al., *Adaptive piezoelectric energy harvesting circuit for wireless remote power supply*. *Power Electronics, IEEE Transactions on*, 2002. **17**(5): p. 669-676.
- [17] Zhu, X. and C.H. Ahn, *On-chip electrochemical analysis system using nanoelectrodes and bioelectronic CMOS chip*. *Sensors Journal, IEEE*, 2006. **6**(5): p. 1280-1286.
- [18] Conway, B., *Electrochemical supercapacitors: scientific fundamentals and technological applications (POD)*. 1999: Kluwer Academic/Plenum: New York.
- [19] Balducci, A., et al., *High temperature carbon-carbon supercapacitor using ionic liquid as electrolyte*. *Journal of Power Sources*, 2006. **165**(2): p. 922-927.
- [20] Lodi, G., et al., *Ruthenium dioxide-based film electrodes*. *Journal of Applied Electrochemistry*, 1978. **8**(2): p. 135-143.
- [21] Hadz, S., et al., *Reversibility and growth behavior of surface oxide films at ruthenium electrodes*. *Journal of The Electrochemical Society*, 1978. **125**(9): p. 1471-1480.
- [22] Miller, J.R. and A.F. Burke, *Electrochemical capacitors: challenges and opportunities for real-world applications*. *The Electrochemical Society Interface*, 2008. **17**(1): p. 53.
- [23] Pandolfo, A. and A. Hollenkamp, *Carbon properties and their role in supercapacitors*. *Journal of Power Sources*, 2006. **157**(1): p. 11-27.
- [24] Burke, A., *R&D considerations for the performance and application of electrochemical capacitors*. *Electrochimica Acta*, 2007. **53**(3): p. 1083-1091.
- [25] Ryoo, R., et al., *Ordered mesoporous carbons*. *Advanced Materials*, 2001. **13**(9): p. 677-681.

- [26] Knox, J.H., B. Kaur, and G.R. Millward, *Structure and performance of porous graphitic carbon in liquid chromatography*. Journal of Chromatography A, 1986. **352**(0): p. 3-25.
- [27] Lee, J., J. Kim, and T. Hyeon, *Recent progress in the synthesis of porous carbon materials*. Advanced Materials, 2006. **18**(16): p. 2073-2094.
- [28] Hirscher, M., et al., *Hydrogen storage in sonicated carbon materials*. Applied Physics A, 2001. **72**(2): p. 129-132.
- [29] Huang, W., et al., *Sonication-assisted functionalization and solubilization of carbon nanotubes*. Nano Letters, 2002. **2**(3): p. 231-234.
- [30] Figueiredo, J., et al., *Modification of the surface chemistry of activated carbons*. carbon, 1999. **37**(9): p. 1379-1389.
- [31] Zhang, J., et al., *Effect of chemical oxidation on the structure of single-walled carbon nanotubes*. The Journal of Physical Chemistry B, 2003. **107**(16): p. 3712-3718.
- [32] Wei, B., et al., *Organized assembly of carbon nanotubes*. Appl. Phys. Lett, 2000. **77**: p. 3764-3766.
- [33] Zhang, Q., J. Rong, and B. Wei, *A divided potential driving self-discharge process for single-walled carbon nanotube based supercapacitors*. RSC Advances, 2011. **1**(6): p. 989-994.
- [34] Zhang, Q., et al., *The governing self-discharge processes in activated carbon fabric-based supercapacitors with different organic electrolytes*. Energy & Environmental Science, 2011. **4**(6): p. 2152-2159.
- [35] Hung, K., et al., *Wide-temperature range operation supercapacitors from nanostructured activated carbon fabric*. Journal of Power Sources, 2009. **193**(2): p. 944-949.
- [36] Subramanian, V., et al., *Supercapacitors from activated carbon derived from banana fibers*. The Journal of Physical Chemistry C, 2007. **111**(20): p. 7527-7531.
- [37] Zhang, X., et al., *Rapid growth of well-aligned carbon nanotube arrays*. Chemical Physics Letters, 2002. **362**(3-4): p. 285-290.
- [38] Calvo, E., et al., *Optimizing the electrochemical performance of aqueous symmetric supercapacitors based on an activated carbon xerogel*. Journal of Power Sources, 2013. **241**: p. 776-782.

[39] Watanabe, M., S.-i. Yamada, and N. Ogata, *Ionic conductivity of polymer electrolytes containing room temperature molten salts based on pyridinium halide and aluminium chloride*. *Electrochimica Acta*, International symposium on polymer electrolytes, 1995. **40**(13-14): p. 2285-2288.

[40] Fuller, J., A. Breda, and R. Carlin, *Ionic liquid-polymer gel electrolytes*. *Journal of the Electrochemical Society*, 1997. **144**(4): p. L67-L70.

[41] Ricketts, B.W. and C. Ton-That, *Self-discharge of carbon-based supercapacitors with organic electrolytes*. *Journal of Power Sources*, 2000. **89**(1): p. 64-69.

Chapter 2

SELF-DISCHARGE IN ACTIVATED CARBON BASED ELECTROCHEMICAL CAPACITORS

2.1 Introduction

The double layer structures grant ECs high power densities and an ultra-long lifespan, but also contribute to the poor energy retention. Lack of knowledge concerning the energy retention, *i.e.*, the self-discharge process of ECs, has been the major barrier posing ECs' application as the energy storage devices [1-4]. Fundamental research in the area of ECs' self-discharge will not only provide useful guidance in improving ECs performance but will also prompt their applications in energy storage devices, especially in the area requiring charging/discharging on a daily or other periodically short-term basis[5-7].

AC is a maturely developed material for electrodes of ECs and has been widely used in commercial ECs due to its high SSA and controllable pore size. Self-discharge study on AC based ECs provides vital information on the fundamentals of self-discharge mechanisms and explores the potential of AC based ECs being energy storage devices.

2.2 Activated Carbon

AC is important in many areas of daily life and modern science, including water/air purification, gas storage, and energy storage. AC is usually obtained *via* carbonization of natural or synthetic carbon-containing precursors followed by

activation treatment[8]. The mostly used precursors are carbon enriching materials such as biomass wastes (coconut shells, sugarcane bagasse, etc)[9-11], coals[12] and polymers (polypyrrole, phenolic resins, etc)[13]. Carbonization is a pyrolysis process that generates structured carbon from the carbon-containing precursors. AC is usually with highly porous structures as a result of activation treatment followed by the carbonization. AC can be classified as microporous (< 2 nm), mesoporous (2-50 nm), and macroporous (> 50 nm) depending on the activated pore width[14]. Physical activation is an activated process that usually performed as pyrolysis together with steam gasification, and alternatively, chemical activation is an activation process using chemical agents such as zinc chloride[15], potassium hydroxide[16], phosphoric acid[17], ammonium chloride[18], hydrochloric acid, and sodium hydroxide, etc. Template synthesis (by Knox) of activated materials has also been maturely developed to control the pore size distribution[14, 19].

Characterization techniques for AC materials include Brunauer-Emmett-Teller (BET) surface area measurement, X-ray photoelectron spectroscopy (XPS), and electron microscopies to investigate details on surface areas, chemical structures, and surface morphologies, etc.

AC advances in application in ECs due to their high SSA and active surfaces. High SSA offers dense accommodation of physisorbed ions of electrolytes for double layer formation, *i.e.*, the high energy density; while the active surface resulted from the defective sites in the carbon lattices as well as the functional groups can be manipulated for controlling electrochemical properties.

Figure 2.1 shows two common forms of AC materials, the powder-like AC and the fiber-like AC. The forms of the AC depend on the synthesis process and they are

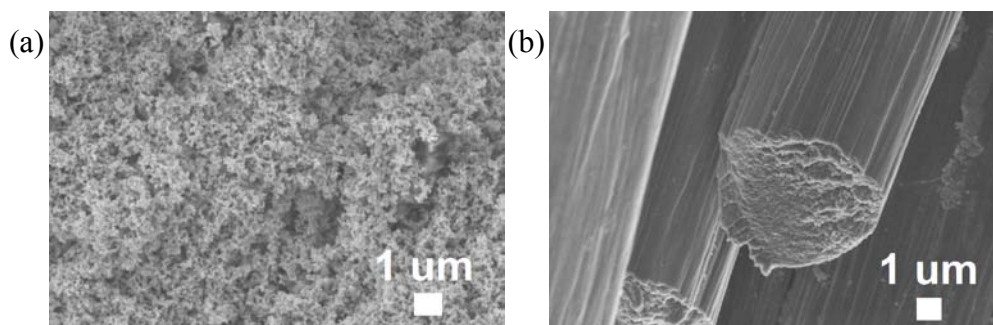


Figure 2.1 Common forms of AC materials (a) powders of AC; (b) fibers of AC.

all with high SSAs after activation. Fabrics woven with AC fibers, *i.e.*, the ACF, are applied in the self-discharge experiments as no binders or current collectors will be needed for the electrode preparation.

2.3 Experimental Section

2.3.1 Sample preparation and EC assembly

Two types of ECs were assembled in a standard 2032 coin cell configuration with ACF (Challenge Carbon Technology Co., Taiwan) as electrodes; 1 M LiPF₆/EC:DEC (Ferro Corporation) and 1 M TEABF₄ (Alfa-Aesar) dissolved in battery-graded PC (Alfa-Aesar) solvent as electrolyte, respectively. The schematic structures of the assembled ECs are shown in Figure 2.2a. The ACF electrode is the same as previously used in the study of wide-temperature operable ECs[20], with an excellent BET SSA of 1340 m²/g mainly comprised of micropores and mesopores. The excellent structural features make the ACF a suitable electrode material for ECs. All of the ECs were assembled in a glove box with an inert environment (O₂ content < 0.1 ppm, H₂O

content < 0.1 ppm), preventing air or moisture from contaminating the ECs in order to eliminate the possibility of pseudocapacitance.

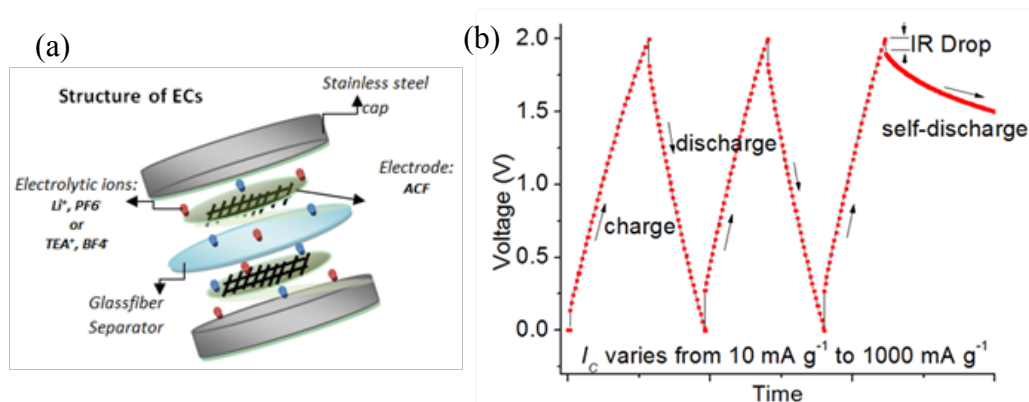


Figure 2.2 (a) Schematic of the assembled ECs with ACF- LiPF_6 and ACF- TEABF_4 structure; (b) Galvanostatic self-discharge testing after two and a half cycle of charging/discharging of the assembled ECs.

2.3.2 Electrochemical testing

The galvanostatic charge/discharge examinations were carried out using an Arbin battery testing system. As shown in Figure 2.2b, two and a half cycle of charge/discharge were applied prior to the self-discharge. The ECs were charged with various charge current densities I_c from 10 to 1000 mA/g. The operational voltage range was controlled from 0 to 2 V, below the decomposition voltage of the organic electrolytes used, to guarantee that the charge storage/release is the double-layer based. All of the two and a half cycle of charging/ discharging were carried out at 25°C while the following self-discharge were conducted at three different temperatures: -25, 25, and 75°C, in order to examine the temperature effects on self-discharge. An alcohol based circulation cooling system

(PolyScience) was used to provide the low temperature (-25°C) environment; and a hot box (Thermo, Electron Corporation) was used to provide the high temperature (75°C) for the self-discharge measurements. Detailed experimental parameters are summarized in Table 2.1.

Table 2.1 Parameters of the self-discharge testing.

| Capacitors (Electrode/Electrolyte) | Charge Current Density I_C (mA·g ⁻¹) (all charged to 2.0 V, at 25°C) | | |
|---------------------------------------|---------------------------------------------------------------------------------------|-------|------|
| | Room Temperature (25°C) | -25°C | 75°C |
| ACF-1 M LiPF ₆ /EC:DEC | 1000, 500, 250, 100, 50, 25, 10 | 100 | 100 |
| ACF-1 M TEABF ₄ /PC | 500, 250, 100, 50, 25* | 100 | 100 |

*Unstable self-discharge at 1000 mA·g⁻¹ and 10 mA·g⁻¹.

2.4 Results and Discussion

2.4.1 Self-discharge curves with organic electrolyte: 1M LiPF₆ in EC:DEC

From the self-discharge curves in Figure 2.3, it can be seen that for the ACF-LiPF₆ EC, increasing the charge current density I_C leads to a higher self-discharge rate, and a larger IR drop. IR drop is the voltage drop from the charged 2.0 V to the actual initial voltage ($V_{initial}$) where the self-discharge starts. It is an intrinsic and unavoidable reflection of the internal resistances of an EC. The ACF-TEABF₄ EC also exhibits a large IR drop especially when it is charged with a large I_C (Figure 2.5). Compared to ECs built with SWNT (see Figure 3.4), the large IR drop indicates a mediocre electric conductivity of ACF as electrode materials.

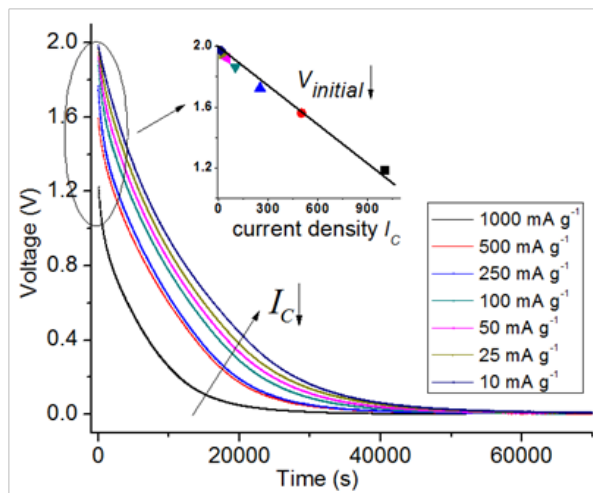


Figure 2.3 Self-discharge curves of the ACF-LiPF₆ EC system under different charge current densities I_C at 25 °C, the inset is the initial voltage versus I_C .

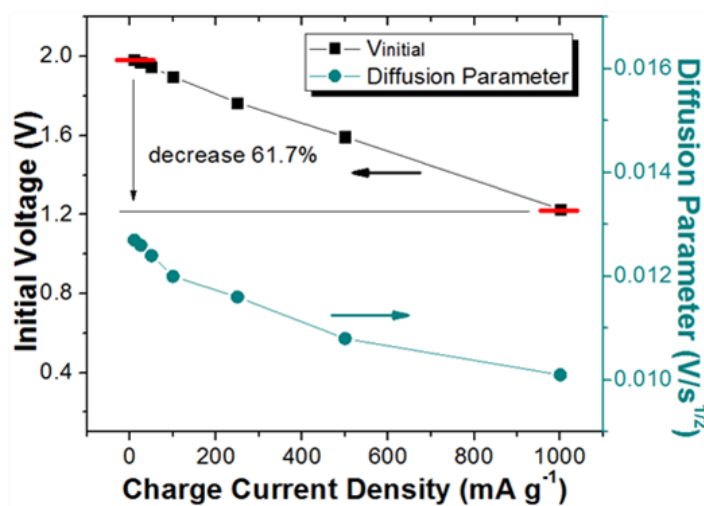


Figure 2.4 Relations on initial voltage and diffusion parameter versus the charge current density I_C .

More details are presented in Figure 2.4. In Figure 2.4, the initial voltage shows a nearly linear relation with the charge current density I_C . A smaller I_C , corresponds to a higher $V_{initial}$.

According to the fitting results in Section 2.4.3.1, self-discharge process in the ACF-LiPF₆ EC is driven by $\partial c/\partial x$ and obey the diffusion control model “ $V=V_{initial} - m \times t^{1/2}$ ” (t is the self-discharge time). Hence, the self-discharge rate is indicated by the slope m , named as the diffusion parameter [21, 22]. The decrease of m when I_C increases is the result of the decrease in the driving force $\partial c/\partial x$, which is scaled by the specific capacitance (see Table 2.2). Details on the self-discharge model fitting are given in Section 2.4.3.1.

2.4.2 Self-discharge curves with organic electrolyte: 1M TEABF₄ in PC

Similar to the self-discharge curves of the ACF-LiPF₆ EC, for the ACF-TEABF₄ EC, its self-discharge rate increases when the charge current density I_C decreases. However, when comparing the self-discharge curves in Figure 2.5 with the curves in Figure 2.3, the ACF-TEABF₄ EC not only displays a much slower discharge rate, but also exhibits a voltage plateau where the EC, especially the EC charged with a relatively smaller I_C , can stay at a voltage of 1.2 V for up to 48 hrs. The voltage plateau describes a slow rate of self-discharge despite of the large driving force from the high potential, which shows a significant difference in the self-discharge behaviors compared to that of the ACF-LiPF₆ EC at the high voltage. As discussed in the Section 2.4.3, the two different choices of electrolytes in the studied ACF based EC systems lead to varied mechanisms governing their self-discharge, and thus, varied behaviors in self-discharge.

Excellent energy retention has been achieved by the ACF-TEABF₄ EC. As

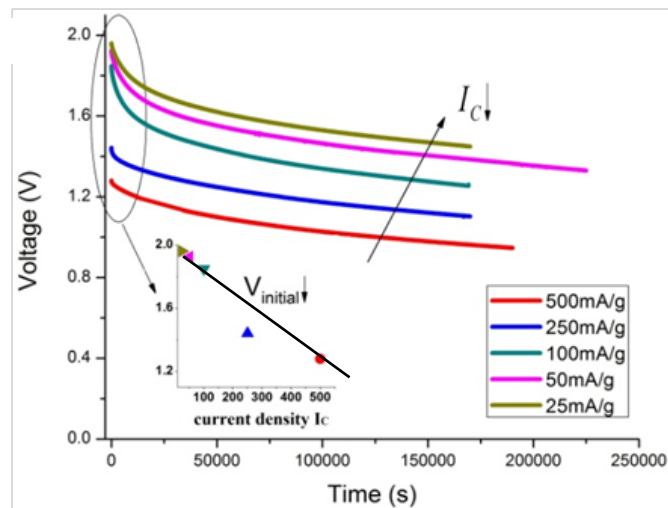


Figure 2.5 Self-discharge curves of the ACF-TEABF₄ EC under different charge current densities I_C at 25 °C, the inset is the initial voltage versus I_C .

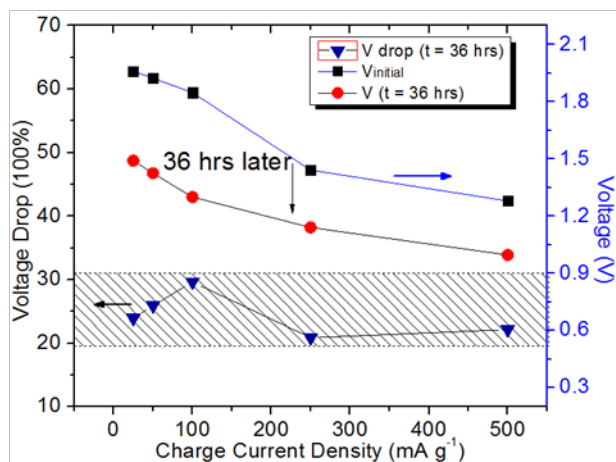


Figure 2.6 Decrease in voltage after 36 hours of self-discharge for the ACF-TEABF₄ EC.

shown in Figure 2.6, after self-discharging for 36 hours, the EC preserves more than 70% of their initial voltage and remains above 1 V. This remarkable high energy retention claims the potential of ECs in the daily chargeable energy storage devices.

2.4.3 Self-discharge models

ECs in the charged condition are in a state with highly positive free energy compared to the discharged or partially discharged states. Virtual forces corresponding to certain mechanisms exist and drive the self-discharge process.[21] In our experiments, the pseudocapacitance is negligible for all the studies of ACF based ECs as demonstrated with their straight galvanostatic charge/discharge curves (see Figure 2.2b). There are two possible driving forces: ionic concentration variation $\partial c/\partial x$ related to the diffusion control model : $V \propto -t^{1/2}$ and the potential field $\Delta E = V$ related to the potential driving model $V \propto e^{-t}$. Specific models obeyed by the ACF-LiPF₆ EC and the ACF-TEABF₄ EC are discussed in the following two sections.

2.4.3.1 Diffusion control model for ACF-LiPF₆ (EC:DEC)

From redrawing each self-discharge curve from Figure 2.3 by setting t to $t^{1/2}$, as shown in Figure 2.7a, within the voltage range from $V_{initial}$ to 37% $V_{initial}$, an almost linear relation between V and $t^{1/2}$ can be observed for all the curves. Curve fitting using the diffusion control model $V=V_{initial} - m \times t^{1/2}$ exhibits a high correlation coefficient R^2 (all higher than 0.99). As shown in Figure 2.7b, the fitted curves overlap the original curves. Hence, within the studied voltage range, self-discharge of the ACF-LiPF₆ EC obeys the diffusion control model.

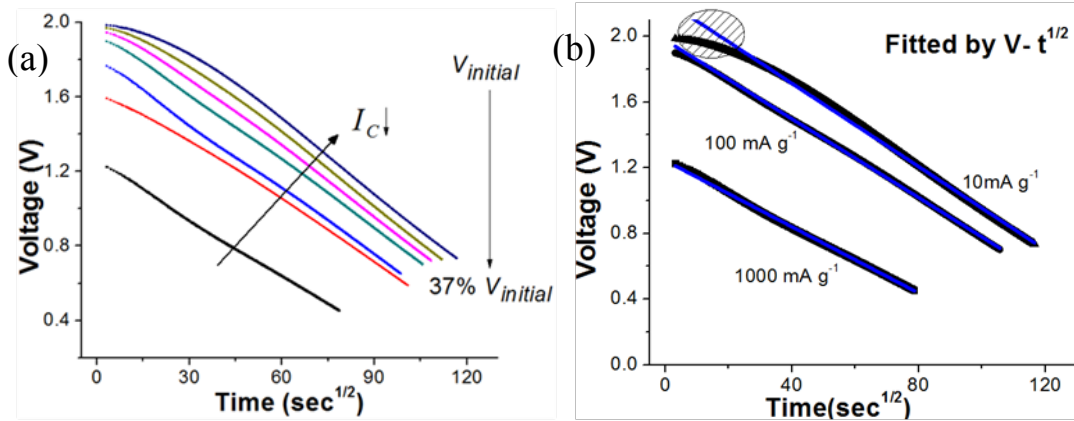


Figure 2.7 (a) Self-discharge curves of the ACF-LiPF₆ EC versus $t^{1/2}$; (b) Fitting the self-discharge curves with Diffusion control model for the ACF-LiPF₆ EC.

Table 2.2. Specific capacitances of the ACF-LiPF₆ EC.

| | Charge Current Density I_C (mA·g ⁻¹) | | | | | | |
|-------------------------------------------|----------------------------------------------------|------|------|------|------|------|------|
| | 10 | 25 | 50 | 100 | 250 | 500 | 1000 |
| Initial Voltage (V) | 1.99 | 1.97 | 1.95 | 1.90 | 1.77 | 1.59 | 1.22 |
| Specific Capacitance (F·g ⁻¹) | 126.7 | 66.2 | 52.2 | 43.2 | 33.7 | 22.5 | 8.1 |

As mentioned in Section 2.4.1, the diffusion parameter m is an indicator of the self-discharge rate for the diffusion controlled self-discharge processes, and for the ACF-LiPF₆ EC, m decreases when I_C increases from 10 to 1000 mA·g⁻¹. Since self-discharge processes of the ACF-LiPF₆ EC are governed by the diffusion control model, their self-discharge rate is then determined by the corresponding driving force, *i.e.*, the ionic concentration gradient $\partial c/\partial x$. As given in the Table 2.2, the specific capacitance C decreases as I_C increases. A larger C means a more

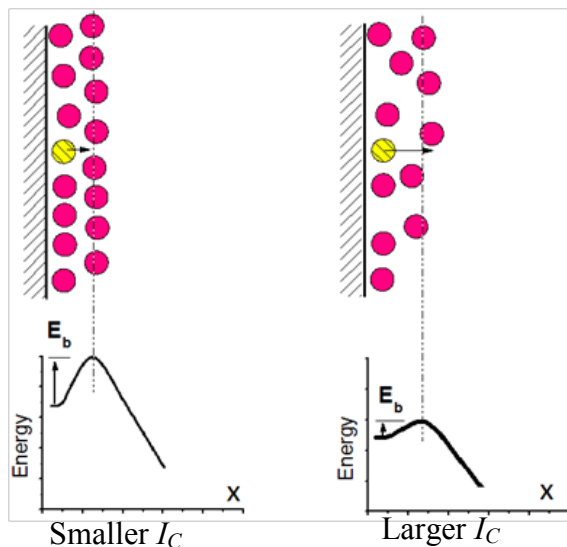


Figure 2.8 Energy barrier E_b for ionic diffusion at different charge current densities I_C .

densed accumulation of ions and thus a larger $\partial c/\partial x$. Hence, with increasing I_C , the decreased self-discharge rate as indicated by smaller m results from the decreased driving force $\partial c/\partial x$ due to the decreased C .

As seen in Figure 2.7b, a small deviation of the fitted curves from the experimental curves has been observed at the beginning of self-discharge, especially for that charged with a small I_C ($10 \text{ mA}\cdot\text{g}^{-1}$). The deviation is considered as a result of the blocking effects of the more denser layers of ions. Theoretically and experimentally, a longer time will be needed to charge an EC with a smaller I_C . The small charge current and the long charging time allow ions to form a more denser structure of charges at the electrode/electrolyte interface, as demonstrated by a relatively large specific capacitance (Table 2.2). As schematically visualized

in Figure 2.8, ions in the double layers need to overcome an energy barrier (E_b) in order to diffuse out. Well-arranged and dense double-layer structures of ions formed with a smaller I_C corresponds to a larger E_b , and thus a more obvious deviation is observed. As shown in the Figure 2.7b, E_b decreases and the deviation gradually fades out as I_C increases.

2.4.3.2 Dual mechanism model of ACF-TEABF₄ (PC)

Different from the ACF-LiPF₆ EC, self-discharge curves of the ACF-TEABF₄ EC cannot be fitted solely by the diffusion control model or the potential driving model. As shown in Figure 2.9, the fitted curves fail to overlap with the original self-discharge curves. Whereas, comparing the fitted curves with the experimental curves in Figure 2.9a, it shows that the self-discharge process become diffusion controlled after a period of time that there is overlapping between the fitted curves and the experimental curves. A transition to the diffusion controlling

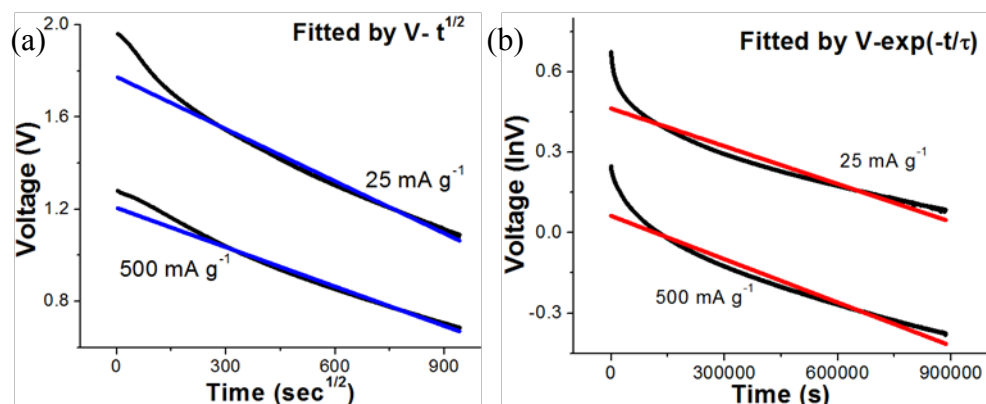


Figure 2.9 Self-discharge curves of the ACF-TEABF₄ EC fitted by: (a) diffusion control model $V \propto t^{-1/2}$; and (b) potential driving model $V \propto \exp(-t/\tau)$.

self-discharge is therefore implied and a dual mechanism (DM) control is proposed which presents good fitting results.

Figure 2.10 shows the fitting results on the self-discharge curves of the ACF-TEABF₄ EC using the proposed DM model. By dividing the self-discharge curve into two parts, the DM model fits the upper half with the potential driving model ($V \propto e^{-t/\tau}$) and the lower half with the diffusion control model ($V \propto t^{-1/2}$), respectively. The red portion represents the curve fitting by the potential driving model ($V \propto e^{-t/\tau}$) and the blue one by the diffusion control model ($V \propto t^{-1/2}$). The nearly perfect curve fittings demonstrate that the ACF-TEABF₄ EC experiences a transition of the dominant self-discharge mechanism from the potential driving model to the diffusion control model for all charge current densities from 25 to 500 mA·g⁻¹.

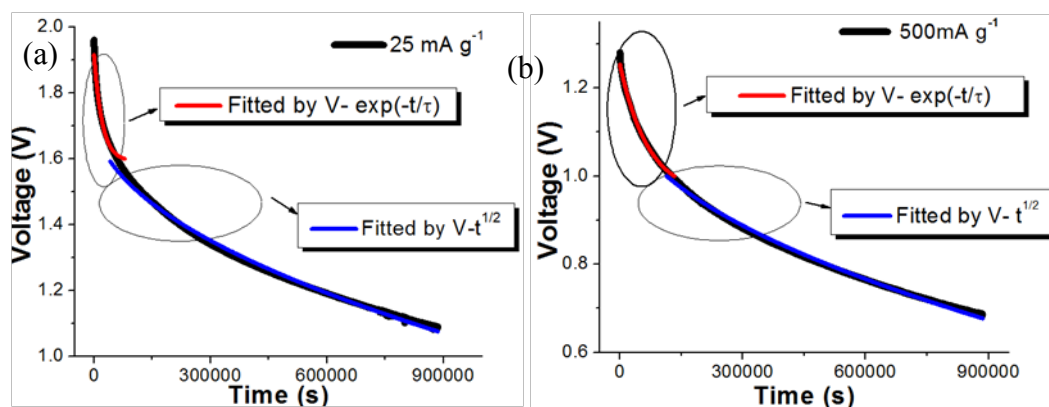


Figure 2.10 Self-discharge curves of the ACF-TEABF₄ EC fitted by the proposed dual mechanism control model: (a) $I_C = 25 \text{ mA}\cdot\text{g}^{-1}$ and (b) $I_C = 500 \text{ mA}\cdot\text{g}^{-1}$. Note: Black curve: original; Red: $V \propto e^{-t}$; Blue: $V \propto t^{-1/2}$. Fitting has been performed for all charge current densities, 25 mA·g⁻¹ and 500 mA·g⁻¹ are shown here as examples.

Transition in the self-discharge mechanisms is essentially an manifestation of the competition between the two driving forces on determining which can drive the ions to diffuse out of the double layers against the drags (from the viscosity of solvent and the electric repellent of other charges, etc). The dominant driving force determines the governing self-discharge model. Therefore, in the ACF-LiPF₆ EC, the dominant driving force is $\partial c/\partial x$, and the self-discharge obeys the diffusion control model. Compared to the ACF-LiPF₆ EC (Table 2.2), the ACF-TEABF₄ EC admits slightly smaller values of the initial voltage as well as much smaller values of the specific capacitance for all charge current densities (Table 2.3); hence the difference of the strength between the two driving forces ΔE and $\partial c/\partial x$ should be smaller in the ACF-TEABF₄ EC. This observation is consistent with the demonstrated co-existence of the diffusion control model and the potential driving model in the ACF-TEABF₄ EC. At the beginning, the self-discharge process is dominated by ΔE and proceeds with a relatively fast rate; as ΔE decreases and cannot drive the ions to diffuse against the drags, the dominant self-discharge mechanism will switch to the diffusion control model, where ions slowly discharge until they are evenly distributed in the electrolyte bulk.

Table 2.3 Specific capacitances of the ACF-TEABF₄ EC.

| | Charge Current Density I_C (mA·g ⁻¹) | | | | |
|-------------------------------------------|----------------------------------------------------|------|------|------|------|
| | 25 | 50 | 100 | 250 | 500 |
| Initial Voltage (V) | 1.96 | 1.92 | 1.85 | 1.44 | 1.28 |
| Specific Capacitance (F·g ⁻¹) | 37.7 | 35.7 | 31.5 | 14.3 | 8.3 |

2.4.3.3 Self-discharge at extended temperature range

Temperature is one of the mostly common environmental factors that should be considered. In this section, two EC systems: the ACF-LiPF₆ EC and the ACF-TEABF₄ EC, have been tested for their self-discharge performances at 75°C and -25°C.

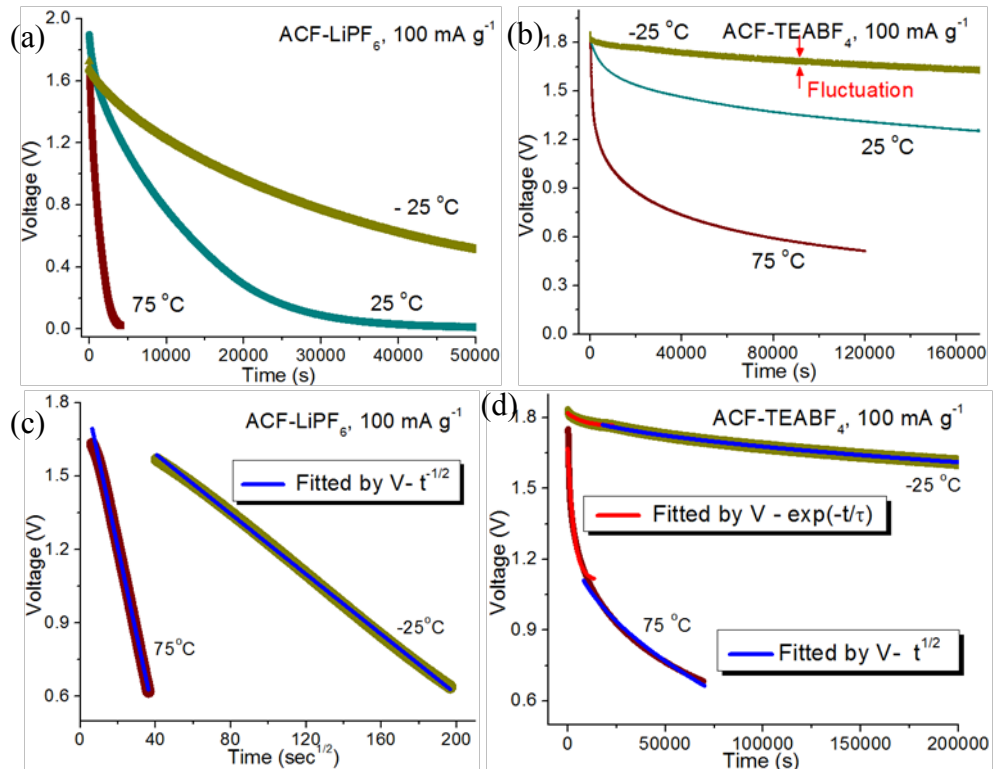


Figure 2.11 Self-discharge behaviors at different temperatures with charge current density of $I_C = 100 \text{ mA} \cdot \text{g}^{-1}$: (a) the ACF-LiPF₆ EC at -25°C, 25°C, 75°C; (b) the ACF-TEABF₄ EC at -25°C, 25°C, 75°C; (c) Fitting with the diffusion control model for the ACF-LiPF₆ EC at -25°C and 75°C; (d) Fitting by the DM model for the ACF-TEABF₄ EC at -25°C and 75°C.

From Figure 2.11a and b, the self-discharge process proceeds at a faster rate at 75°C and at a slower rate at -25°C. Moreover, as shown in Figure 2.11c and d, with the excellent curve fitting results, the diffusion control model applied well to the ACF-LiPF₆ EC and the DM control model applied well to the ACF-TEABF₄ EC at both 75°C and -25°C. Hence, it is concluded that self-discharge temperature does not affect the self-discharge mechanisms for the studied ECs.

A wide voltage fluctuation in the self-discharge curve was observed in the ACF-TEABF₄ EC at -25°C (Figure 2.11 b, dark yellow line), which was not noticed for the ACF-LiPF₆ EC at the same low temperature. As known, reducing the temperature will impair the ionic mobility due to the increase in electrolyte viscosity and the de-activation of ionic thermal activity[23]. The phenomenon of voltage fluctuation is absent in the ACF-LiPF₆ EC at -25°C, implying the difference in ionic mobility for the two organic electrolytes and the relatively poor mobility of TEA⁺ and/or BF₄⁻ ions in PC solvent at the subzero temperature of -25°C. As an important and indispensable component in an EC assembly, electrolyte plays a critical role in determining the governing self-discharge mechanisms and the self-discharge performances, though the specific principles are unavailable yet but surely worthy of further study.

2.5 Conclusions

Self-discharge is a spontaneous and self-driving process. In the two studied ACF-LiPF₆ EC and ACF-TEABF₄ EC where no electron transfer is involved, there are two driving forces existed: the potential field ΔE and the ionic concentration variation $\partial c/\partial x$; one leads to a self-discharge process dominated by the potential driving model and the other by the diffusion control model. The dominant self-

discharge model for a real EC system depends on the relative strength of the two driving forces.

For the ACF-LiPF₆ EC, the driving force from $\partial c/\partial x$ outweighs the potential driving force ΔE to a great extent and the diffusion control model governs the self-discharge until 37% of the initial voltage. While in the ACF-TEABF₄ EC, due to the different ionic mobility of the electrolyte, the driving forces ΔE and $\partial c/\partial x$ have comparable strength. Self-discharge of the ACF-TEABF₄ EC is first dominated by the potential driving model and then switched to the diffusion control model.

Based on the discussion above, we may expect that a potential driving self-discharge is likely to happen on ECs with a high voltage and a low capacitance; while a diffusion control self-discharge is prone to occur on ECs with a low voltage and a high specific capacitance.

In summary, we have demonstrated that ECs with the same electrode material (ACF) but different electrolytes obey different self-discharge mechanisms. The diffusion control model governs the self-discharge processes in the ACF-LiPF₆ ECs while the DM control model controls the self-discharge processes in the ACF-TEABF₄ ECs. It is also evident that both models are valid under different charge current densities and can be extended to a wide temperature range. Most importantly, an excellent energy retainability has been achieved in the ACF-TEABF₄ ECs, with more than 70% retention after 36 hours of self-discharging, indicating the great potential of ECs for periodic energy storage/supplies which require high reliability and a long service life.

ACKNOWLEDGMENTS

The author wishes to thank Jiepeng Rong for the help on the self-discharge measurements in this chapter. This chapter was previously published in ref. [6]. Reprinted with permission, Copyright 2011 Royal Society of Chemistry.

REFERENCES

- [1] Kotz, R. and M. Carlen, *Principles and applications of electrochemical capacitors*. Electrochimica Acta, 2000. **45**(15-16): p. 2483-2498.
- [2] Burke, A., *Ultracapacitors: why, how, and where is the technology*. Journal of power sources, 2000. **91**(1): p. 37-50.
- [3] Masarapu, C., et al., *Effect of temperature on the capacitance of carbon nanotube supercapacitors*. Acs Nano, 2009. **3**(8): p. 2199-2206.
- [4] Balducci, A., et al., *Cycling stability of a hybrid activated carbon//poly(3-methylthiophene) supercapacitor with N-butyl-N-methylpyrrolidinium bis(trifluoromethanesulfonyl)imide ionic liquid as electrolyte*. Electrochimica Acta, 2005. **50**(11): p. 2233-2237.
- [5] Zhang, Q., et al., *Tunable self-discharge process of carbon nanotube based supercapacitors*. Nano Energy, 2014. **4**: p.14-22.
- [6] Zhang, Q., et al., *The governing self-discharge processes in activated carbon fabric-based supercapacitors with different organic electrolytes*. Energy & Environmental Science, 2011. **4**(6): p. 2152-2159.
- [7] Zhang, Q., J. Rong, and B. Wei, *A divided potential driving self-discharge process for single-walled carbon nanotube based supercapacitors*. RSC Advances, 2011. **1**(6): p. 989-994.
- [8] Rodriguez-Reinoso, F. and M. Molina-Sabio, *Activated carbons from lignocellulosic materials by chemical and/or physical activation: an overview*. Carbon, 1992. **30**(7): p. 1111-1118.
- [9] Williams, P.T. and A.R. Reed, *Development of activated carbon pore structure via physical and chemical activation of biomass fibre waste*. Biomass and Bioenergy, 2006. **30**(2): p. 144-152.
- [10] Tan, I., A.L. Ahmad, and B. Hameed, *Adsorption of basic dye on high-surface-area activated carbon prepared from coconut husk: Equilibrium, kinetic and thermodynamic studies*. Journal of Hazardous Materials, 2008. **154**(1): p. 337-346.

- [11] Rufford, T.E., et al., *Microstructure and electrochemical double-layer capacitance of carbon electrodes prepared by zinc chloride activation of sugar cane bagasse*. Journal of Power Sources, 2010. **195**(3): p. 912-918.
- [12] Gryglewicz, G.y., et al., *Effect of pore size distribution of coal-based activated carbons on double layer capacitance*. Electrochimica Acta, 2005. **50**(5): p. 1197-1206.
- [13] Tanahashi, I., A. Yoshida, and A. Nishino, *Electrochemical characterization of activated carbon-fiber cloth polarizable electrodes for electric double-layer capacitors*. Journal of The Electrochemical Society, 1990. **137**(10): p. 3052-3057.
- [14] Ryoo, R., et al., *Ordered mesoporous carbons*. Advanced Materials, 2001. **13**(9): p. 677-681.
- [15] Hu, Z. and M. Srinivasan, *Mesoporous high-surface-area activated carbon*. Microporous and Mesoporous Materials, 2001. **43**(3): p. 267-275.
- [16] Mitani, S., et al., *Activation of raw pitch coke with alkali hydroxide to prepare high performance carbon for electric double layer capacitor*. Journal of Power Sources, 2004. **133**(2): p. 298-301.
- [17] Kennedy, L.J., J.J. Vijaya, and G. Sekaran, *Effect of two-stage process on the preparation and characterization of porous carbon composite from rice husk by phosphoric acid activation*. Industrial & Engineering Chemistry Research, 2004. **43**(8): p. 1832-1838.
- [18] Balci, S., T. Dogu, and H. Yucel, *Characterization of activated carbon produced from almond shell and hazelnut shell*. Journal of Chemical Technology and Biotechnology, 1994. **60**(4): p. 419-426.
- [19] Knox, J.H., B. Kaur, and G.R. Millward, *Structure and performance of porous graphitic carbon in liquid chromatography*. Journal of Chromatography A, 1986. **352**(0): p. 3-25.
- [20] Hung, K., et al., *Wide-temperature range operation supercapacitors from nanostructured activated carbon fabric*. Journal of Power Sources, 2009. **193**(2): p. 944-949.
- [21] Conway, B., *Electrochemical supercapacitors: scientific fundamentals and technological applications (POD)*. 1999: Kluwer Academic/Plenum: New York.
- [22] Ricketts, B.W. and C. Ton-That, *Self-discharge of carbon-based supercapacitors with organic electrolytes*. Journal of Power Sources, 2000. **89**(1): p. 64-69.
- [23] Xu, K., *Nonaqueous liquid electrolytes for lithium-based rechargeable batteries*. Chemical Reviews, 2004. **104**(10): p. 4303-4418.

Chapter 3

SELF-DISCHARGE OF SINGLE-WALLED CARBON NANOTUBE BASED ELECTROCHEMICAL CAPACITORS

3.1 Introduction

Self-discharge mechanisms depend on the structures of ECs, *i.e.*, the choices of electrode materials and electrolytes. As discussed in Chapter 2, for ECs built with ACF, the carbon-based material with a high SSA and a mediocre electric conductivity, the ACF-LiPF₆ EC is dominated by the diffusion control model while the ACF-TEABF₄ EC is governed by the DM model. The competition of the two driving forces, the potential field ΔE and the ionic concentration gradient $\partial c/\partial x$, determines the dominant self-discharge model; and it is expected that ECs with a high initial voltage ($\Delta E = V$) and a low specific capacitance C (small $\partial c/\partial x$ by $Q = C \times V$) tend to be dominated by the potential driving model [1].

CNTs are of particular interests for the development of EC electrodes because of their unique tubular porous structures and superior electrical properties[2-4], which are favored for fast charge transportation[5-7]. So far, extensive research has been conducted on CNT-based ECs, covering from improving the energy density through increasing the electrochemical active species or the surface areas (methods include acid treatments[8], particles' decoration[9-11], mixing with additives[12, 13], etc), to the effects of temperature[14], pressure[15], and other factors on the electrochemical performance. However, there is little attention on evaluating their energy retainability and self-discharge behaviors. To further verify the hypothesis that the competition of

driving forces determines the self-discharge mechanisms in different carbon materials, CNTs, of superior electric conductivity and relatively low surface area compared to ACF, are the perfect choice of electrode material to study.

3.2 Single-walled Carbon Nanotube

Due to their superior electrical, mechanical, chemical, and thermal properties stemming from the one dimensional structure, CNTs have captured the attention in various research fields such as energy storage devices, nanocomposites, transistors, and sensors.

A CNT is structured of carbon atoms as 12 pentagons forming the closed tip and millions of hexagons extending along the CNT wall[16]. The CNT wall can be imagined as the one-atom thick sheets of carbon (called graphene) rolling at specific angles, and the helicity of the tube determines whether the CNT tube is a metallic or a semiconductor[3]. Depending on the assembly patterns, CNT can be divided into two types: the single-walled carbon nanotube (SWNT) and the multiwalled carbon nanotube (MWNT). As shown in Figure 3.1a and c, SWNTs consist of a single graphene sheet seamlessly wrapped into a cylindrical tube; and MWNTs (see Figure 3.1b and d) consist of concentric tubes of CNTs with a layer-to-layer separation of 0.34 nm. Individual tubes, no matter of MWNTs or of SWNTs, naturally bundle themselves together into bundles by van der Waals forces.

MWNTs are commonly in the form of powders, while SWNTs can form free-standing sheets by filtering SWNT dispersions or directly synthesizing from a chemical vapor deposition (CVD) method[14, 17]. The free-standing films of SWNTs can be directly used as electrodes without binders or current collectors, which is one of the advantages of SWNT films as electrode materials for EC assembly.

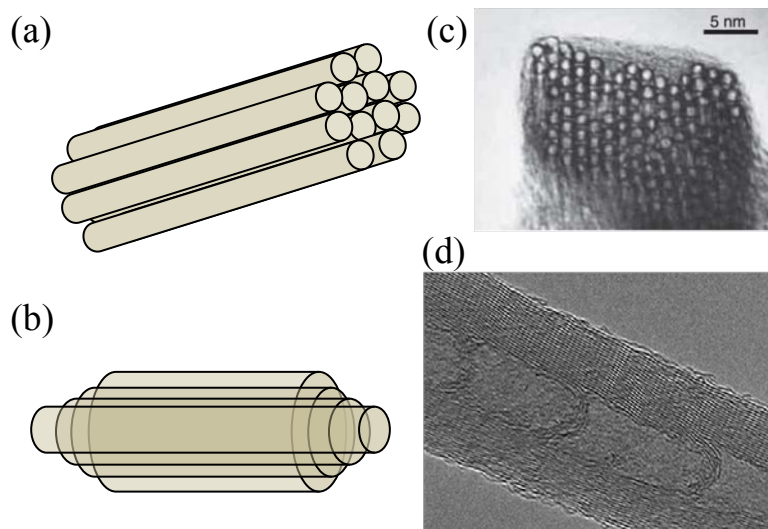


Figure 3.1 Schematic of (a) SWNTs and (b) MWNTs; (c) TEM image of SWNTs, with permission from ref. 17 (Appendix C: 3); (d) TEM image of MWNTs, with permission from ref. 18 (Appendix C: 4).

Compared to porous carbon materials such as AC[19], SWNTs exhibit their own superiority as electrode materials for ECs in terms of their outstanding electrical conductivity for fast charge transfer and the availability of free standing macro-films. ECs built with free-standing SWNT films are investigated for the effects of electrode properties on the self-discharge mechanism.

3.3 Experimental Section

3.3.1 Sample preparation and EC assembly

As shown in Figure 3.2a, the free-standing SWNT macrofilms were fabricated using the CVD method. Ferrocene and sulfur were mixed at an atomic ratio of Fe:S = 10:1, serving as precursor. The reaction took (30 – 50) min at 1140 °C under a mixture

gas flow of argon and hydrogen. In order to get rid of the impurities such as amorphous carbon and the catalytic iron particles, the synthesized SWNT films were treated in air at 420 °C for 30 min and then rinsed with hydrochloric acid and copious deionized water. After air-drying, the free standing SWNT macrofilms were ready to use for EC assembly.

Organic electrolyte, 1M TEABF₄/PC, was applied, which is the same organic electrolyte as used in the self-discharge study for ACF based ECs (Chapter 2). The SWNT-TEABF₄ ECs were assembled in a standard 2032 coin cell in a glove box, where the atmospheric conditions were maintained at an adequate level (O₂ content < 0.1 ppm, H₂O content < 0.1 ppm) to prevent air or moisture from contaminating into the ECs. The structure of the as-assembled EC is given in Figure 3.2b.

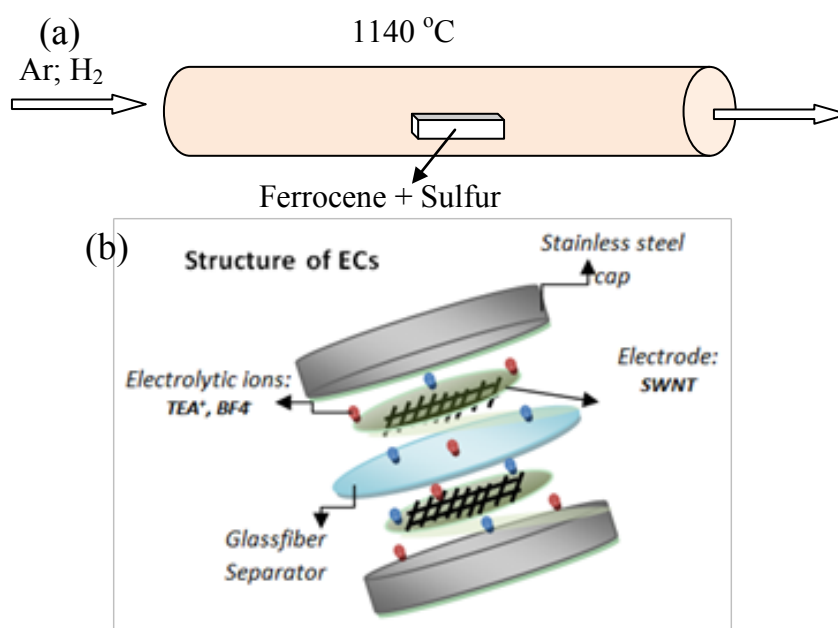


Figure 3.2 Schematic of (a) the CVD synthesis of SWNTs and (b) the EC assembly.

3.3.2 Self-discharge testing

As shown in Figure 3.3, the galvanostatic charge/discharge/self-discharge tests were carried out using an Arbin battery testing system. The assembled ECs were charged/discharged with different charge current densities ($I_C = 1000, 500, 250, 100, 50, 25, \text{ and } 10 \text{ mA}\cdot\text{g}^{-1}$) for two and a half cycles (0 to 2.0 V) at room temperature (25°C), then followed with the self-discharge. The self-discharge was also tested at 75°C and -25°C for ECs charged with $100 \text{ mA}\cdot\text{g}^{-1}$ at 25°C, to study the effects of temperature on the self-discharge.

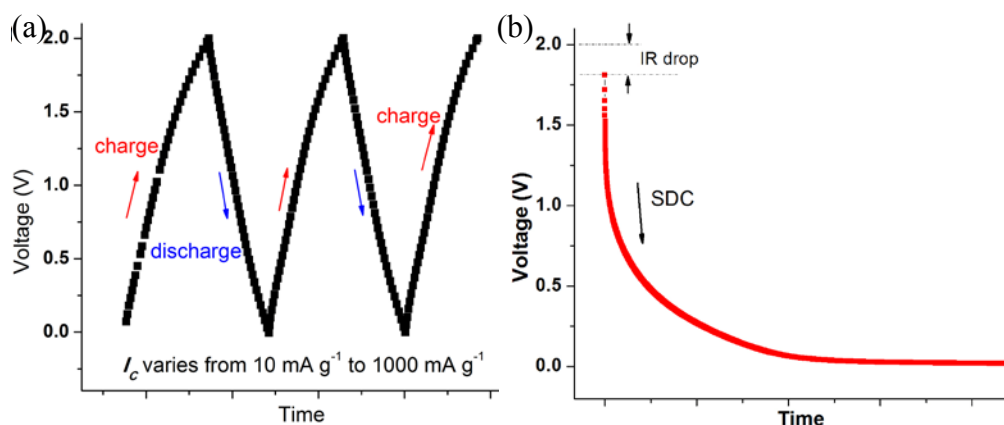


Figure 3.3 Illustration of the self-discharge testing: (a) two and a half cycle charging/discharging, followed by (b) the self-discharge process.

Controls such as the operation voltage of 2.0 V (lower than the decomposition voltage of the 1M TEABF₄/PC organic electrolyte) as well as the glove box operations were taken to eliminate the possibility of pseudocapacitance, as evidenced with the straight galvanostatic charge/discharge curves in Figure 3.3a.

3.4 Results and Discussion

3.4.1 Self-discharge curves

Self-discharge curves charged with different charge current densities from 10 to 1000 mA·g⁻¹ at 25°C are shown in Figure 3.4. With decreasing I_C , the self-discharge rate decreases. Compared with the ACF-TEABF₄ EC using ACF as electrodes (see Figure 2.5), the SWNT-TEABF₄ EC exhibits much smaller IR drop, about 9% voltage drop than the 35%-40% voltage drop of the ACF-TEABF₄ EC, due to its excellent electric conductivity and fast charge transfer on electrode/electrolyte interface.

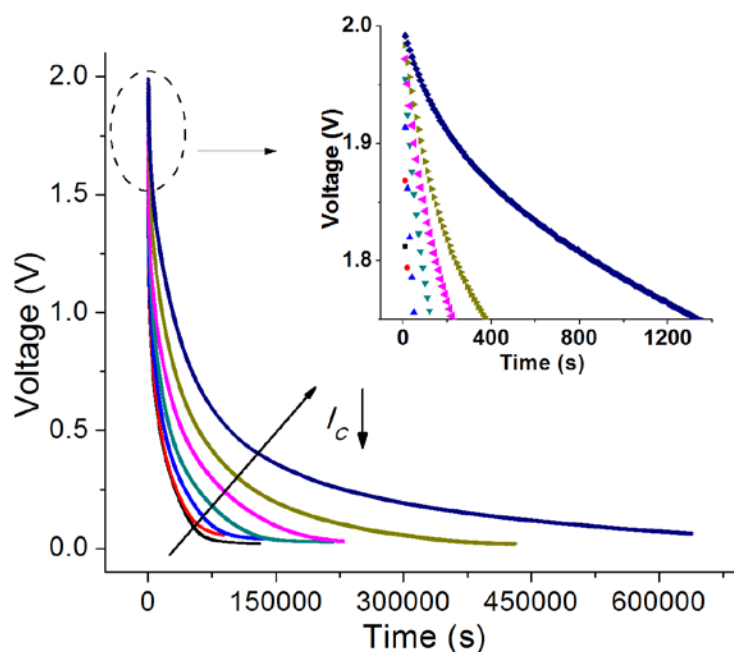


Figure 3.4 Self-discharge curves with charge current densities I_C from 10 to 1000 mA·g⁻¹ at 25 °C; the inset shows the zoom-in at the beginning of the self-discharge.

Moreover, a much higher self-discharge rate is presented for the SWNT-TEABF₄ EC, especially at the beginning of the self-discharge, where the voltage decreases so fast that the collected data points are disconnected from each other (inset of Figure 3.4, time interval between two voltage points is 10 sec). Specifically, the decrement in the first 10 sec from the initial voltage reaches up to 0.1 V when $I_C=1000 \text{ mA}\cdot\text{g}^{-1}$, which is ten times of that for the ACF-TEABF₄ EC at the same conditions.

The faster self-discharge rate and the smaller IR drop compared to those of the ACF-TEABF₄ EC demonstrate the superior capability of charge transportation of SWNTs as electrode materials, which then contributes a stronger driving force of ΔE for self-discharge.

3.4.2 Self-discharge model

Same as the ACF based EC, no pseudocapacitance has been observed for the SWNT-TEABF₄ EC. Therefore, there are two possible driving forces: the potential field ΔE and the ionic concentration variation $\partial c/\partial x$.

From the curve fitting results (Figure 3.5), neither the diffusion control model ($V \propto -t^{1/2}$) nor the potential driving model ($V \propto e^{-t/\tau}$) can fit well with the experimental self-discharge curves. Meanwhile, the curves cannot be fitted with the DM model proposed for the ACF-TEABF₄ EC.

Based on the previous study on self-discharge of ACF based EC, ECs with a high initial voltage and a low specific capacitance are expected to self-discharge under the potential field driving. As given in Table 3.1, the SWNT-TEABF₄ EC exhibits a higher initial voltage compared to that of the ACF-TEABF₄ EC (Table 2.3), while the specific capacitance is comparable to that of the ACF-TEABF₄ EC (Table 2.3). Therefore, the SWNT-TEABF₄ EC is prone to be driven by the potential

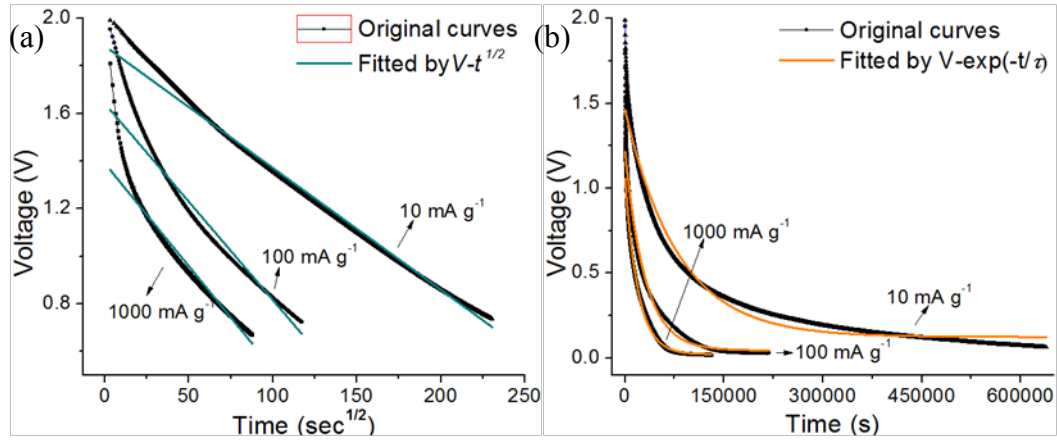


Figure 3.5 Fitting results of the self-discharge curves with (a) the diffusion control model: $V \propto -t^{1/2}$ and (b) the potential driving model: $V \propto e^{-t/\tau}$.

Table 3.1 Specific capacitances of the SWNT-TEABF₄ EC.

| | Charge Current Density I_C (mA·g ⁻¹) | | | | | | |
|-------------------------------------------|----------------------------------------------------|-------|------|------|------|------|------|
| | 10 | 25 | 50 | 100 | 250 | 500 | 1000 |
| Initial Voltage (V) | 1.99 | 1.98 | 1.97 | 1.96 | 1.91 | 1.89 | 1.81 |
| Specific Capacitance (F·g ⁻¹) | 63.8 | 29.64 | 22.3 | 20.0 | 19.0 | 18.4 | 16.7 |

field. Further investigation reveals that self-discharge of the SWNT-TEABF₄ EC is under the potential field driving though cannot be fitted with one exponential decay component. It requires two exponential decay components for perfect fitting. A split potential driving model is then proposed based on the self-discharge of the SWNT-TEABF₄ EC, termed as the “Divided Potential Driving” (DPD) model.

3.4.2.1 Divided potential driving model and single potential driving model

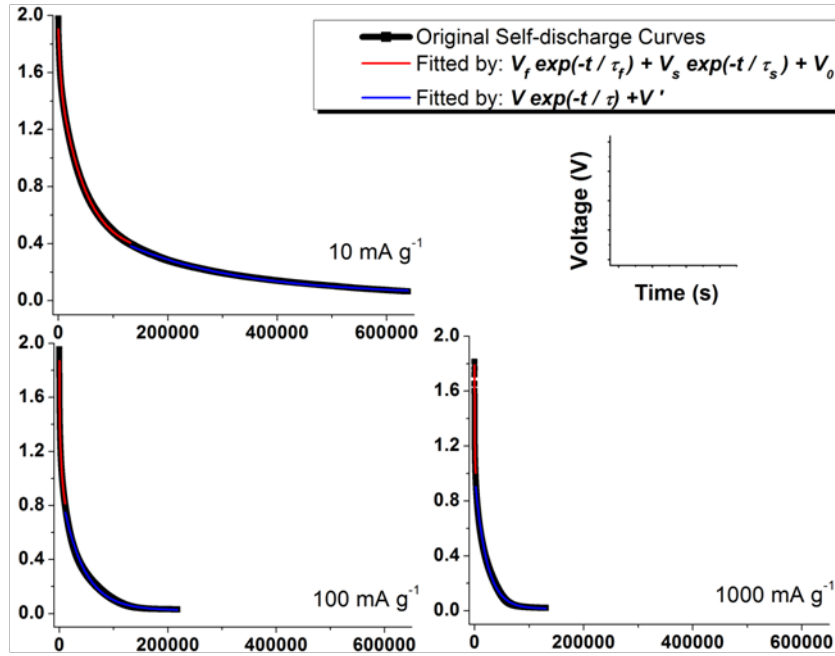


Figure 3.6 Self-discharge curves (black) fitted with the DPD model: (red) and single potential driving model (blue). Note: Selected self-discharge curves with 10, 100, and 1000 mA·g⁻¹ are presented).

Table 3.2 Self-discharge parameters under different charge current densities.

| | Self-discharge Temperature (°C) | | | | | | | | |
|-----------------------------|---------------------------------|------|------|------|------|------|------|------|------|
| | 25 | | | | | | | 75 | -25 |
| I_C (mA·g ⁻¹) | 10 | 25 | 50 | 100 | 250 | 500 | 1000 | 100 | 100 |
| $V_f/V_{initial}$ | 0.18 | 0.20 | 0.24 | 0.22 | 0.21 | 0.23 | 0.26 | 0.22 | 0.43 |
| V_f/V_s | 0.28 | 0.37 | 0.56 | 0.55 | 0.59 | 0.73 | 0.99 | 1 | 0.48 |
| τ_f (sec) | 3507 | 1705 | 886 | 470 | 179 | 88 | 55 | 454 | 3321 |
| τ_s/τ_f | 14 | 18 | 14 | 13 | 16 | 18 | 16 | 1 | 11 |
| τ/τ_f | 60 | 58 | 68 | 85 | 162 | 240 | 392 | 7 | 66 |

Figure 3.6 illustrates the self-discharge curve fitting results with the proposed DPD model. As depicted in the figure, at the beginning, the self-discharge process is driven by ΔE and fitted with two exponential decay components:

$$V = V_f \times e^{-t/\tau_f} + V_s \times e^{-t/\tau_s} + V_0, \tau_s > \tau_f \text{ ----- } 3.1$$

After a period of time, it switches to the single potential-driving process:

$$V = V \times e^{-t/\tau} + V' \text{ ----- } 3.2$$

This interesting phenomenon has never been noticed and reported before. The self-discharge process dominated with Eqn. 3.1 is termed as the DPD process, in order to distinguish from the usual “Single Potential Driving” (SPD) process described with Eqn. 3.2. The proposed DPD \rightarrow SPD model fits very well on the self-discharge processes of the SWNT-TEABF₄ EC.

In the potential driving model, the time constant τ is the characteristic parameter to describe the self-discharge rate, and is determined by the mobility of ions and the magnitude of the potential field. Smaller τ describes a faster self-discharge process while larger τ indicates a slower self-discharge process. Hence, in Eqn. 3.1, $V_s \times e^{-t/\tau_s}$ (with a larger time constant τ_s) expresses the self-discharge process with a slower rate, while $V_f \times e^{-t/\tau_f}$ (with a smaller time constant τ_f) represents the self-discharge process with a faster self-discharge rate. In another word, the DPD model comprises of one slower SPD process and one faster SPD process and the two processes proceed simultaneously.

According to the DPD model, ions in the double-layer structures could be divided into two groups. The values of V_1 and V_2 reflect the quantities of the charge in

each groups based on $Q = C \times V$. Therefore, $V_f/V_{initial}$ gives the ratio of the charges of the fast self-discharge ions to the total charges contained in the double layers. Details are given in Table 3.2 and will be discussed in Section 3.4.2.2.

3.4.2.2 Origins of the divided potential driving model

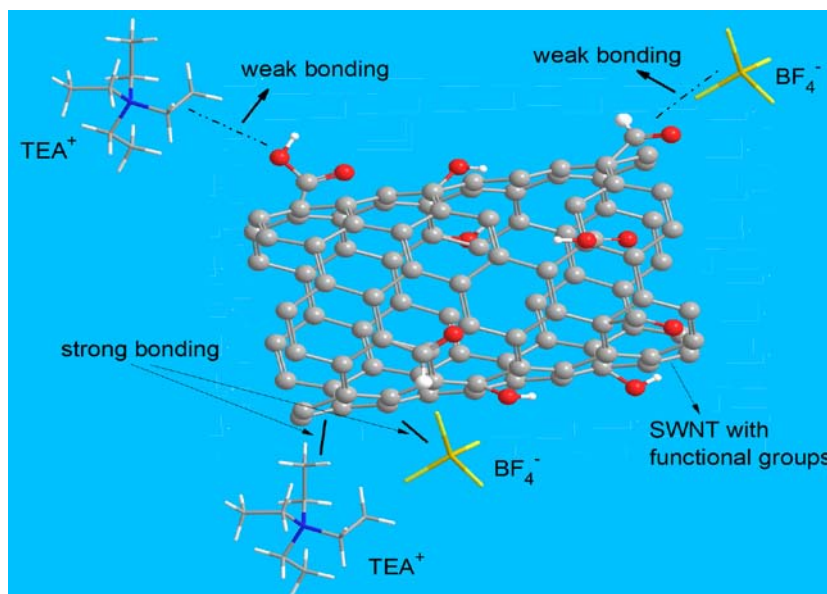


Figure 3.7 Illustration of the functional groups interference on interactions between the electrolytic ions and the charged electrode.

In the potential driving self-discharge process, self-discharge proceeds as the driving force ΔE overcomes the drags (viscosity and the electric repellent of other charges, etc). In the SWNT-TEABF₄ EC, since the environment, including the potential field and the electrolyte bulk, between the two electrode/electrolyte

interfaces are shared, the possible reason that divides electrolytic ions into two groups is then predicted to be the heterogeneity of the electrode surface.

Oxygenated functional groups (such as carboxyl, carbonyl, and hydroxyl groups, etc.) are attached onto the SWNT surface during the purification process[19]. Considering the comparable size of the functional groups such as -COOH (~0.2 nm in diameter) to the diameter of electrolytic ions (such as BF_4^- 0.33 nm in diameter)[20] and the atomic thickness of double layers, the electrostatic interactions between ions and the charged SWNT surfaces can be affected by those polarized functional groups under the potential field.

As illustrated in Figure 3.7, as a result of the interference of the functional groups, the distance between the ions and the charged SWNT surface is expanded and it leads to a relatively weak bonding compared to the direct interaction between the ions and the intact SWNT surface. Consequently, it generates two groups of ions: the tight-bonded ions where the intact surface is present[21] and the weak-bonded ions where the functional groups are present. This is consistent with the self-discharge process described by the DPD model. Two groups of ions co-exist and contribute to the capacitance in the EC with varied self-discharge rates. The strong-bonded ions would correspond to the term of $V_s \times e^{-t/\tau_s}$ with the larger time constant τ_s and the weak-bonded ions would be represented by the term of $V_f \times e^{-t/\tau_f}$ with the smaller time constant τ_f . As a self-discharge process begins, both strong-bonded ions and the weak-bonded ions start to move out of the Helmholtz layers. Once the weak-bonded ions (with a faster diffusion rate) are all out of the Helmholtz layers, the “ $V_f \times e^{-t/\tau_f}$ ” term will be vanishing and the DPD model will then switch to the SPD model accordingly.

The inference that the DPD model is triggered by the heterogeneity of functional group distribution on SWNTs surfaces is also evidenced by the V_f/V_s ratio (Table 3.2), which is close to the functional group coverage of SWNT surfaces (around 1:4 to 1:3). A designed research on the effects of functional groups on the SWNT-TEABF₄ EC self-discharge further confirms the conclusions and will be discussed in Chapter 4, where through tailoring the functional groups, the tuning of the self-discharge process is realized for the first time.

3.4.2.3 Self-discharge at extended temperature range

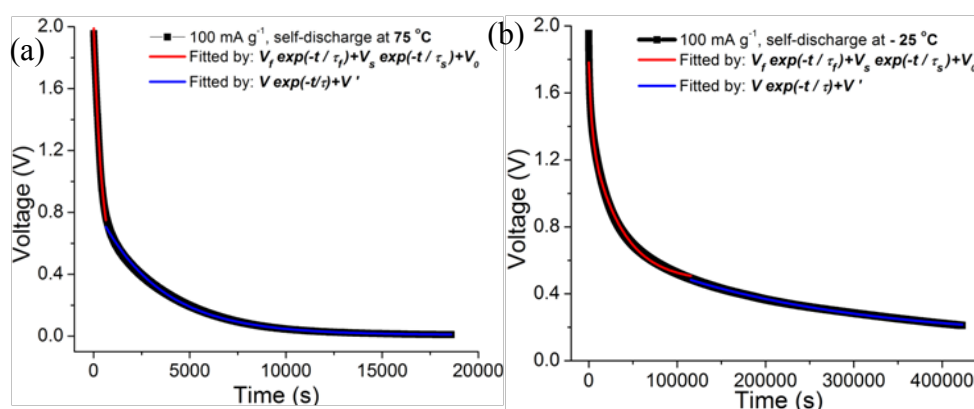


Figure 3.8 Self-discharge curves (black) fitted with the DPD model (red) and the SPD model (blue), (a) at 75 °C and (b) at -25 °C.

Fitting results for the self-discharge curves at different temperatures are given in Figure 3.8. The perfect curve fittings indicate that the proposed DPD model to the SPD model can be extended to a large temperature range: down to -25 °C and up to 75 °C. The self-discharge rate decreases at -25 °C because of the impaired ionic

mobility at low temperature and increases at 75 °C due to the enhanced ionic mobility at high temperature. Due to the effects of temperature on the thermal energy of ions and the viscosity of organic solvent, relative quantities between weak-bonded ions and strong-bonded ions also change in the DPD self-discharge process (Table 3.2).

Moreover, at -25 °C, the voltage ratio V_f/V_s is calculated to be 0.48 (Table 3.2), indicating that the weak-bonded ions take up $\sim 1/3$ of the total ions while the strong-bonded ions take up $\sim 2/3$ of the total. This is consistent with previous characterization results obtained on the SWNT films that around 1/3 surfaces of the SWNT are functionalized[17]. Since the ionic mobility activated by the thermal energy is greatly impaired at the subzero temperature of -25 °C and the V_f/V_s ratio admitted at this condition approaches to the actual coverage of functional groups. Hence, the calculated ratio based on the proposed DPD model shows consistency with the characterization results.

3.5 Conclusions

SWNT has superior electric conductivity compared to ACF. Self-discharge of the SWNT-TEABF₄ EC has been demonstrated to be driven by the potential field, confirming the hypothesis that ECs with a high initial voltage ($\Delta E = V$) and a low specific capacitance C (small $\partial c/\partial x$ by $Q = C \times V$) tends to be dominated by the potential driving model.

The DPD model is proposed based on the SWNT-TEABF₄ EC and explains very well the self-discharge behaviors. The self-discharge process experiences a change from the DPD model to the SPD model. Functional groups on the SWNT surfaces are responsible for the division in the DPD self-discharge model as the

polarized functional groups affect the interactions between electrolytic ions and the charged SWNT surfaces.

In summary, we have demonstrated that SWNT-TEABF₄ EC obey the potential driving mechanism and experience a transition from the DPD model to the SPD model. It is also evidenced that the models are valid under different charge current densities and can be extended to a wide temperature range. Most importantly, the DPD model reveals the underlying relation between the self-discharge performance and the microstructures of SWNT electrode materials. As discussed in Chapter 4, the finding provides guidance in designing EC configuration for realizing self-discharge tuning, indicating the great potential to design ECs for applications requiring varied energy retentions.

ACKNOWLEDGMENTS

The author wishes to thank Jiepeng Rong for the help on the self-discharge measurements in this chapter. This chapter was previously published in ref. [22]. Reprinted with permission, Copyright 2011 Royal Society of Chemistry.

REFERENCES

- [1] Zhang, Q., et al., *The governing self-discharge processes in activated carbon fabric-based supercapacitors with different organic electrolytes*. Energy & Environmental Science, 2011. **4**(6): p. 2152-2159.
- [2] Wei, B., R. Vajtai, and P. Ajayan, *Reliability and current carrying capacity of carbon nanotubes*. Applied Physics Letters, 2001. **79**(8): p. 1172-1174.
- [3] Ebbesen, T., et al., *Electrical conductivity of individual carbon nanotubes*. Nature, 1996. **382**: p. 54-56.
- [4] Dai, H., E.W. Wong, and C.M. Lieber, *Probing electrical transport in nanomaterials: conductivity of individual carbon nanotubes*. Science, 1996. **272**(5261): p. 523-526.
- [5] Frackowiak, E. and F. Beguin, *Carbon materials for the electrochemical storage of energy in capacitors*. Carbon, 2001. **39**(6): p. 937-950.
- [6] Pandolfo, A. and A. Hollenkamp, *Carbon properties and their role in supercapacitors*. Journal of Power Sources, 2006. **157**(1): p. 11-27.
- [7] Simon, P. and Y. Gogotsi, *Materials for electrochemical capacitors*. Nature Materials, 2008. **7**(11): p. 845-854.
- [8] Chen, X., et al., *Improvement in electrochemical capacitance of carbon materials by nitric acid treatment*. Journal of Power Sources, 2008. **184**(2): p. 668-674.
- [9] Hung, T.-C., et al., *One-Step Fabrication of Carbon Nanotubes Decorated with Graphitic Nanoflakes for Energy Storage Systems*. Journal of Nanoscience and Nanotechnology, 2010. **10**(7): p. 4738-4742.
- [10] Ellis, A.V., et al., *Hydrophobic anchoring of monolayer-protected gold nanoclusters to carbon nanotubes*. Nano Letters, 2003. **3**(3): p. 279-282.
- [11] Carrillo, A., et al., *Noncovalent functionalization of graphite and carbon nanotubes with polymer multilayers and gold nanoparticles*. Nano Letters, 2003. **3**(10): p. 1437-1440.

- [12] An, K.H., et al., *High-capacitance supercapacitor using a nanocomposite electrode of single-walled carbon nanotube and polypyrrole*. Journal of the Electrochemical Society, 2002. **149**(8): p. A1058-A1062.
- [13] Ma, S.B., et al., *Electrochemical properties of manganese oxide coated onto carbon nanotubes for energy-storage applications*. Journal of Power Sources, 2008. **178**(1): p. 483-489.
- [14] Masarapu, C., et al., *Effect of temperature on the capacitance of carbon nanotube supercapacitors*. ACS Nano, 2009. **3**(8): p. 2199-2206.
- [15] Li, X., J. Rong, and B. Wei, *Electrochemical behavior of single-walled carbon nanotube supercapacitors under compressive stress*. ACS Nano, 2010. **4**(10): p. 6039-6049.
- [16] Iijima, S. and T. Ichihashi, *Single-shell carbon nanotubes of 1-nm diameter*. Nature, 1993. **363**: p. 603-605.
- [17] Zhu, H. and B. Wei, *Direct fabrication of single-walled carbon nanotube macrofilms on flexible substrates*. Chemical Communications, 2007. **29**: p. 3042-3044.
- [18] Meier, M.S., et al., *Tearing open nitrogen-doped multiwalled carbon nanotubes*. Journal of Materials Chemistry, 2008. **18**: p. 4143-4145.
- [19] Lee, J., J. Kim, and T. Hyeon, *Recent progress in the synthesis of porous carbon materials*. Advanced Materials, 2006. **18**(16): p. 2073-2094.
- [20] Chmiola, J., et al., *Anomalous increase in carbon capacitance at pore sizes less than 1 nanometer*. Science, 2006. **313**(5794): p. 1760-1763.
- [21] Frolov, A.I., A.G. Rozhin, and M.V. Fedorov, *Ion interactions with the carbon nanotube surface in aqueous solutions: understanding the molecular mechanisms*. ChemPhysChem, 2010. **11**(12): p. 2612-2616.
- [22] Zhang, Q., J. Rong, and B. Wei, *A divided potential driving self-discharge process for single-walled carbon nanotube based supercapacitors*. RSC Advances, 2011. **1**(6): p. 989-994.

Chapter 4

TUNING SELF-DISCHARGE: EFFECTS OF FUNCTIONAL GROUPS ON SELF-DISCHARGE OF SINGLE-WALLED CARBON NANOTUBE BASED ELECTROCHEMICAL CAPACITORS

4.1 Introduction

Study on the self-discharge processes of various ECs of different electrode/electrolyte architectures allows us to gain insights into the underlying mechanisms. For the SWNT-TEABF₄ EC's self-discharge, the DPD model has been proposed and has demonstrated its reliability in fitting and characterizing the self-discharge processes[1]. Based on the discussion in Chapter 3, the determining factor leading to the DPD model instead of the SPD model is predicted to be related to the functional groups attached on the SWNT surfaces, as the heterogeneity on the surface chemistry creates two types of interactions between ions and electrode at the electrode/electrolyte interface.

Oxygenated functional groups are commonly presented on the SWNT surface and can enhance the wettability of the SWNTs in the electrolytes of the polarized solvent molecules and ions. Qualitative analysis of the functional group effects on the self-discharge of the SWNT-TEABF₄ ECs has been introduced in Chapter 3. However, quantitative evaluation on how and to what extent the functional groups affect self-discharge is still lacking. Self-discharge study on the SWNT-TEABF₄ ECs with elaborated amounts of functional groups not only provides knowledge of the effects of functional groups on the self-discharge mechanisms, but also, of the greater

significance, explores the possibility to tune the self-discharge processes with controlled functional groups.

4.2 Functional Groups

In electrochemistry, carbon materials are one of the most common materials under exploration, not only for ECs, but also for rechargeable batteries[2, 3]. Many properties of carbon materials are decisively influenced by various oxygenated functional groups[4]. By altering the quantities and species of the attached functional groups, properties of carbon materials such as hydrophilicity[5-7] or electroconductivity[8, 9] can be maneuvered, subsequently manipulating the performance of the carbon materials in various areas such as electrocatalysts[10], gas adsorption[11], gas sensing[12, 13], thermal sensing[6], composite strengthening[14-16], and electrochemical performance[3, 17, 18].

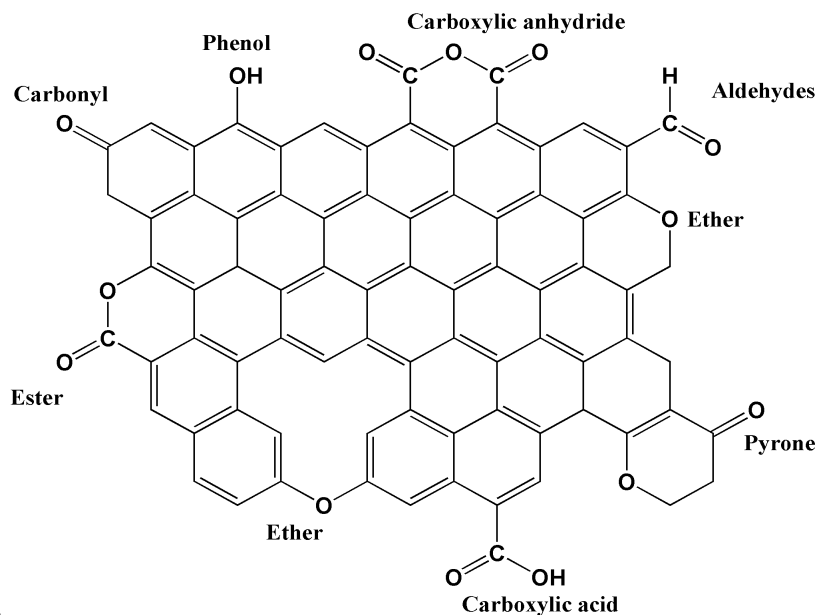


Figure 4.1 Structure of carbon surface with various functional groups.

As well-known, surface reactivity and the edge effects of the hexagonal plane in carbon materials can lead to the presence of functional groups on the carbon lattices, usually the oxygen-containing functional groups. Figure 4.1 presents the common types of oxygen-containing functional groups attached on the carbon surfaces. During the preparation of the SWNTs, the purification process consisting of the heat treatment and the acid-based bath can introduce a certain amount of functional groups onto the SWNT samples after CVD synthesis. Before purification, the SWNTs are hydrophobic and inert. After decoration with those oxygen containing functional groups, the SWNT surfaces become hydrophilic.

The quantity and type of functional groups are determined by the conditions and procedures of the carbon material preparation.

Treatments for carbon functionalization have already been well studied and can be categorized into four general methods:

1. Liquid-phase oxidation[19-21], where oxidizing agents are applied in acidic conditions;
2. Gas-phase oxidation[22, 23], where O_2 , H_2O in gas phase are used at very high temperatures up to 2300 °C;
3. Plasma treatment with atomic oxygen or ozone[23];
4. Heat treatment with inert gas protection or in vacuum[23].

The first three methods are used for increasing the functional groups and the last one is usually employed for decreasing the functional groups. Other properties of carbon such as surface area, porosity, and chemical affinity, etc, can also be modified during those procedures.

Common identification techniques of the oxygen functional groups on carbon materials[20] include the acid-base titration, Raman spectroscopy, XPS, temperature-programmed desorption, thermal gravimetric analysis (TGA), and Near-edge X-ray absorption fine structure.

In addition to the common oxygen-containing functional groups, other types of functional groups can be obtained through a specific treatment, like carbon fluorides formed when F_2 come into contact with graphitic carbon at elevated temperatures[23]. These functional groups (C_xLi , C_xNa , and $(CF)_n$, etc) are different from the surface or edge-bound functional groups mentioned earlier. They exist in the form of intercalated compounds and the formation of those compounds comes along with volume changes, the processes of which are the same as the battery-type and different from the pseudocapacitance arisen from the reversible electrosorption occurred on the oxygen-containing functional groups.

In summary, oxygen-containing functional groups are generally unavoidable for carbon-based materials and can influence their electrochemical performance. Since self-discharge is a spontaneous process, in which ions diffuse out of the double layers to reach the equilibrium[24-26], factors such as functional groups that can affect the interactions between the ions and the charged surface will subsequently have an influence on the self-discharge behaviors. In the rest of this chapter, the effects of the functional groups on the self-discharge will be systematically investigated through elaborately analyzing the self-discharge processes of ECs built with different SWNT samples with controlled amounts of functional groups.

4.3 Experimental Section

4.3.1 Sample preparation

Fabrication of SWNT macrofilms was done by the CVD method (Figure 3.2), followed with the heat treatment in air at 420 °C for 30 min and then rinsed with hydrochloric acid and copious DI water. After air-drying, the obtained samples were referred as SWNT. The purification process would introduce a certain amount of functional groups onto the SWNT films. In order to obtain SWNT samples with varied amounts of functional groups, post-treatments are applied. Heat treatment (400 °C in argon) was applied to reduce functional groups because functional groups tend to decompose at elevated temperatures [3, 4, 27], and the obtained SWNT film samples are referred as *r*-SWNT. On the other hand, in order to increase the number of functional groups, the SWNT films were soaked in the KMnO₄ solution [28, 29] (0.1 g KMnO₄ in 20 mL concentrated sulfuric acid) for 10 min, and followed with hydrochloric acid rinsing and copious DI water washing. The as-treated sample after air-drying was referred as *o*-SWNT. Both reduction and oxidation procedures were carried out in a gentle manner in order to preserve the tangled structures of the SWNT films.

4.3.2 Sample characterizations

The SEM (scanning electron microscopy) images were taken using a JEOL JSM-7400F scanning electron microscope. For XPS, monochromatic aluminum K α X-ray (1486.6 eV) was applied to excite photoelectrons from the carbon nanotube surface. All spectra were calibrated by setting the C 1s photoemission peak for sp²-hybridized carbons to 284.5 eV, and were fitted after a Shirley type background subtraction. Raman spectra were collected using a laser with an excitation wavelength

of 532 nm. TGA was conducted from room temperature to 1000 °C at a heating rate of 2 °C min⁻¹ under nitrogen protection (60 mL min⁻¹).

4.3.3 Self-discharge testing

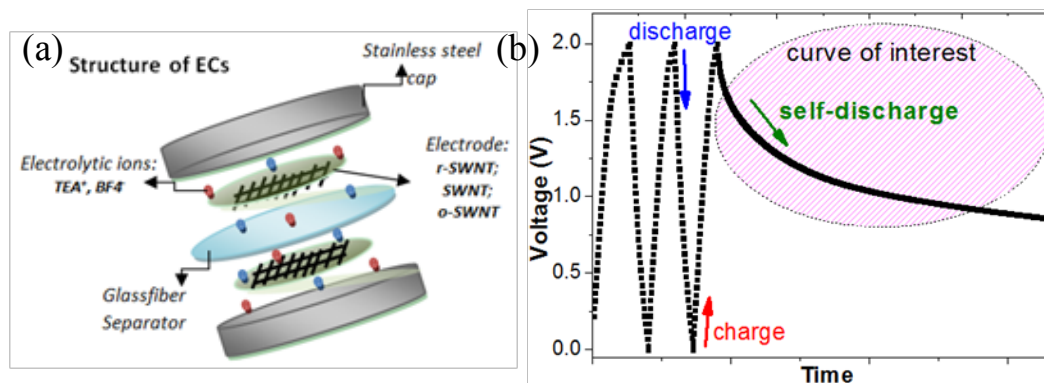


Figure 4.2 (a) Schematic of the structures of the built ECs, each with *r*-SWNT, SWNT, and *o*-SWNT as electrodes, and 1M TEABF₄ (PC) as electrolyte; (b) The self-discharge experiments after two and a half cycles of charging/discharging.

In order to study the effects of varied functional groups on self-discharge, ECs were built each with the SWNT, *r*-SWNT, and *o*-SWNT films as electrodes, which are punched into 1 inch in diameter, and 1M TEABF₄/PC as electrolyte (see schematic in Figure 4.2a). The ECs were assembled in the glove box filled with argon and the glove box was maintained at an adequate level (O₂ content < 0.1 ppm, H₂O content < 0.1 ppm).

With the assembled SWNT-based ECs, the electrochemical impedance spectroscopy (EIS) was recorded over a frequency range from 100 kHz to 10 mHz; cyclic voltammetry (CV) was scanned at voltage ramp of 10 mV s⁻¹ from -2 to 2 V;

the self-discharge tests were performed using the Arbin battery testing system with a charging current density of $100 \text{ mA}\cdot\text{g}^{-1}$ followed by self-discharge at two different temperatures: room temperature ($20 \text{ }^\circ\text{C}$) and $-25 \text{ }^\circ\text{C}$, to investigate the effects of functional groups on the self-discharge process.

4.4 Results and Discussion

4.4.1 SWNT microstructure and chemical identification analysis

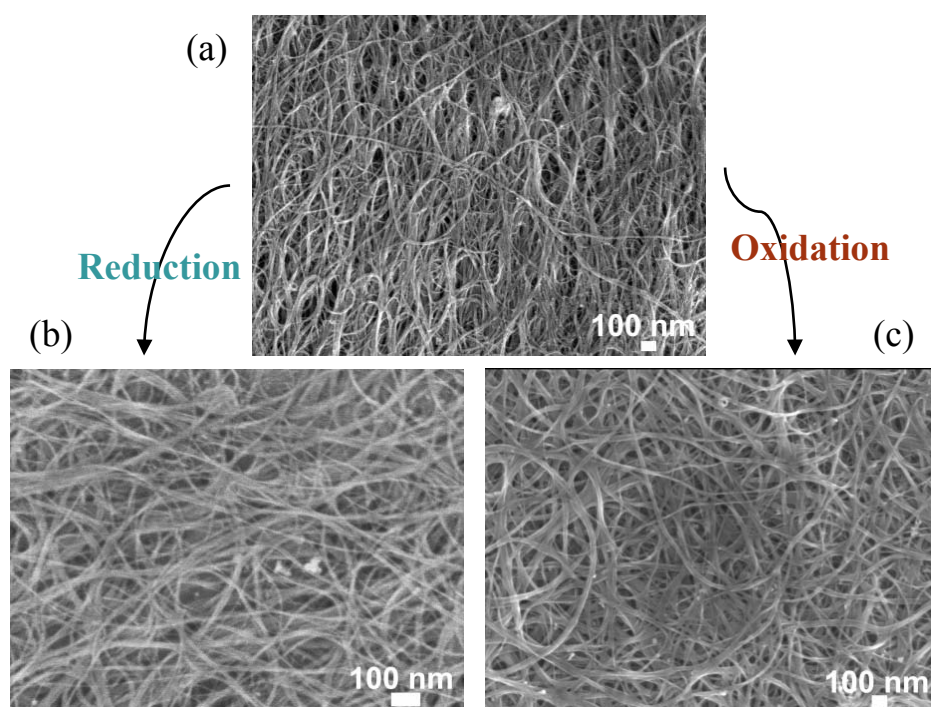


Figure 4.3 SEM images taken on (a) SWNT; (b) r-SWNT after heat treatment; and (c) o-SWNT after oxidation treatment.

SEM were performed over all three prepared samples, which indicated no obvious changes on the tangled structures of the SWNT films after both reduction and oxidation treatments (Figure 4.3). BET surface area characterization has been performed as well. From the results (Table 4.1), the specific area changes after the

Table 4.1 Atomic percentage concentrations of r-SWNT, SWNT and o-SWNT based on XPS survey.

| Sample Name | Atomic % | | Ratio | BET surface area (m ² -g ⁻¹) |
|----------------|----------|-------|-------|-----------------------------------------------------|
| | C 1s | O 1s | C/O | |
| <i>r</i> -SWNT | 96.3% | 3.7% | 26.3 | 445.7 |
| SWNT | 93.5% | 6.5% | 14.3 | 490.2 |
| <i>o</i> -SWNT | 80.7% | 19.3% | 4.2 | 563.4 |

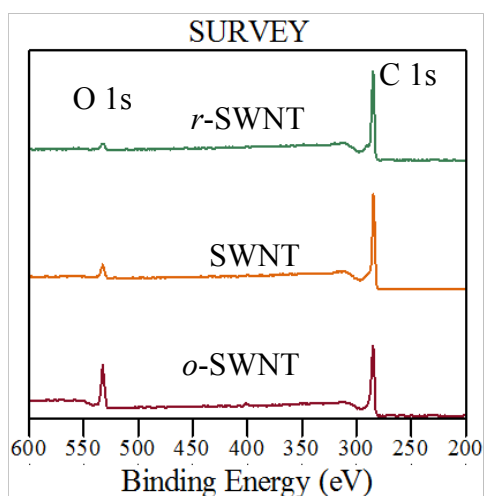


Figure 4.4 XPS survey of 400 °C heat-treated SWNT (*r*-SWNT, cyan), as-prepared SWNT (SWNT, orange), and KMnO₄-oxidized SWNT (*o*-SWNT, maroon).

post-treatments, *i.e.*, decreases after the reduction of the heat treatment, and increases after the KMnO_4 oxidation, but does not change significantly. It again confirms that the applied post-treatments are controlled to be mild to tailor the functional groups without sacrificing much on the carbon structures of SWNT.

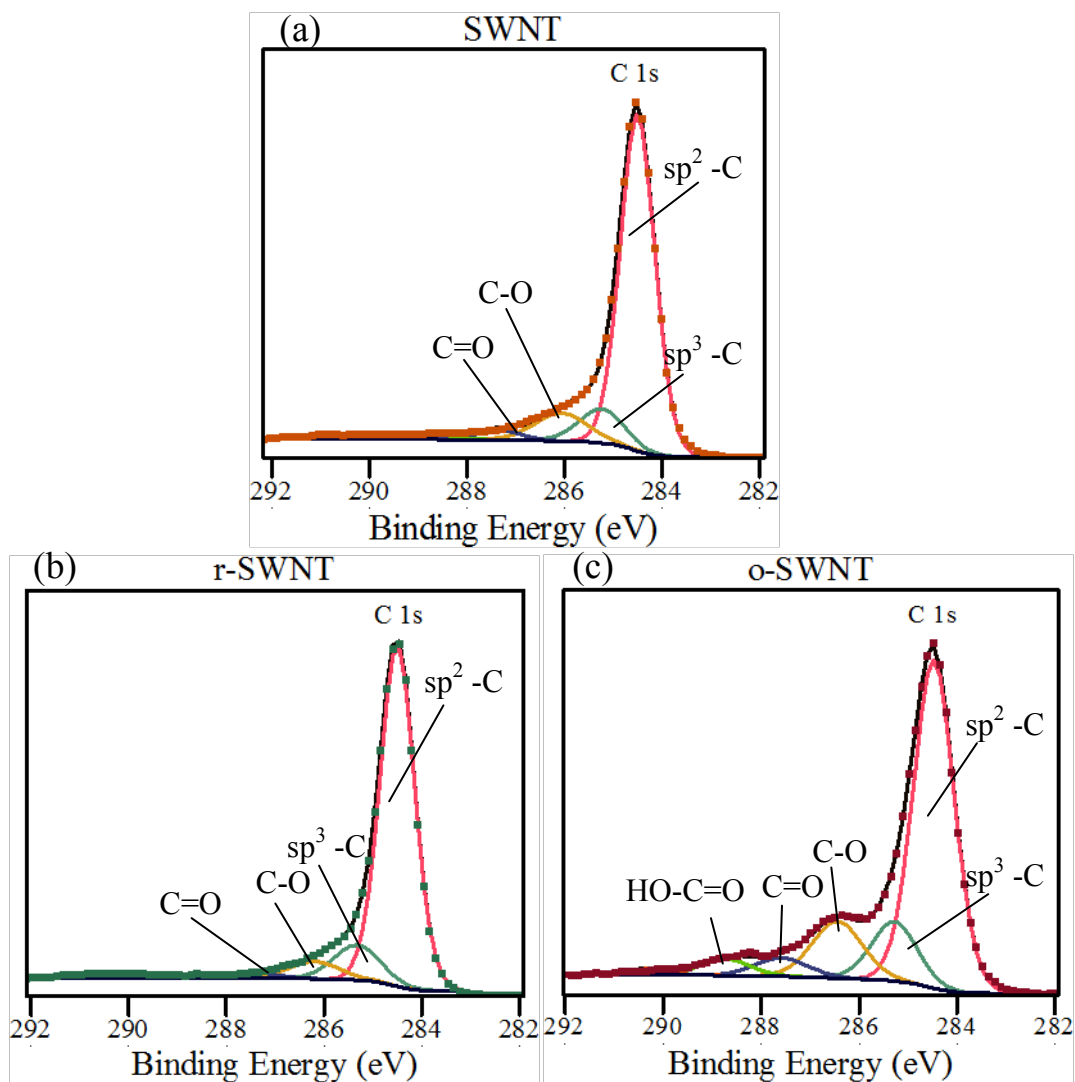


Figure 4.5 C 1s binding energy (BE) regions of (a) r-SWNT; (b) SWNT; and (c) o-SWNT. All spectra were calibrated by setting the main peak in the C 1s BE region to the sp^2 -hybridized carbons at 284.5 eV.

Table 4.2 Atomic percentage concentrations of various carbon functional groups of *r*-SWNT, SWNT, and *o*-SWNT based on XPS curve fittings.

| Sample Name | Relative atomic concentrations (%) | | | | | | Total functional groups |
|----------------|------------------------------------|--------------------|------|-----|------|------|-------------------------|
| | sp ² -C | sp ³ -C | C-O | C=O | COOH | p-p* | |
| <i>r</i> -SWNT | 77.6 | 11.7 | 5.9 | 1.8 | 1.2 | 1.8 | 8.9 |
| SWNT | 67.9 | 15.1 | 9.4 | 3.7 | 2.3 | 1.6 | 15.4 |
| <i>o</i> -SWNT | 64.5 | 12.2 | 12.2 | 5.2 | 4.7 | 1.2 | 22.1 |

In addition to structural characterizations of the three types of SWNT samples using SEM, chemical identification of the film samples was addressed by XPS.

Figure 4.4 shows the survey scans on the three SWNT samples. As given in Table 4.1, the *r*-SWNT sample possesses the highest C/O ratio and the *o*-SWNT sample possesses the lowest C/O ratio, confirming the reducing effect of the heat treatment for the *r*-SWNT sample and the oxidizing effect of KMnO₄ for the *o*-SWNT sample. Furthermore, high-resolution C1s scans (Figure 4.5) reveal the existence of several functional groups including C-O (~286.2eV), C=O (~287.5 eV), and COOH (~288.7 eV)[18,34,35]. Quantitative results on the functional groups are calculated by deconvoluting the C1s region and summarized in Table 4.2. For all three SWNT samples, sp² carbon takes up the major portion, from 77.6% of the *r*-SWNT sample to 64.5% of the *o*-SWNT sample. Sp² carbon is the carbon atom with sp² hybridization and associated with an aromatic structure. A higher percentage of sp² carbon indicates a better graphitization and fewer defects in the lattice structures of carbon nanotubes[30, 31]. The *r*-SWNT sample possesses fewer functional groups (~8.9%) due to the heat treatment while KMnO₄ acidic solution produces more oxygen-

containing functional groups (~22.1%) on the *o*-SWNT sample, and the SWNT sample without any post-treatment contains 15.4% of functional groups.

The reduction of *r*-SWNT and the oxidation of *o*-SWNT have also been confirmed with Raman and TGA measurements. As shown in Figure 4.6a, Raman spectra present the varied I_D/I_G . The D band (~1343 cm^{-1}) is induced by the structural disorder, and the G band (~1583 cm^{-1}) is related to the aromaticity of the carbon lattice[32]. The increasing ratio of I_D/I_G from *r*-SWNT, SWNT to *o*-SWNT indicates that *o*-SWNT possesses the highest percentage of defects. Defects in CNT structures usually serve as the chemically active sites for functional groups[31]. More defects would allow more functional groups to be accommodated onto the SWNT surfaces.

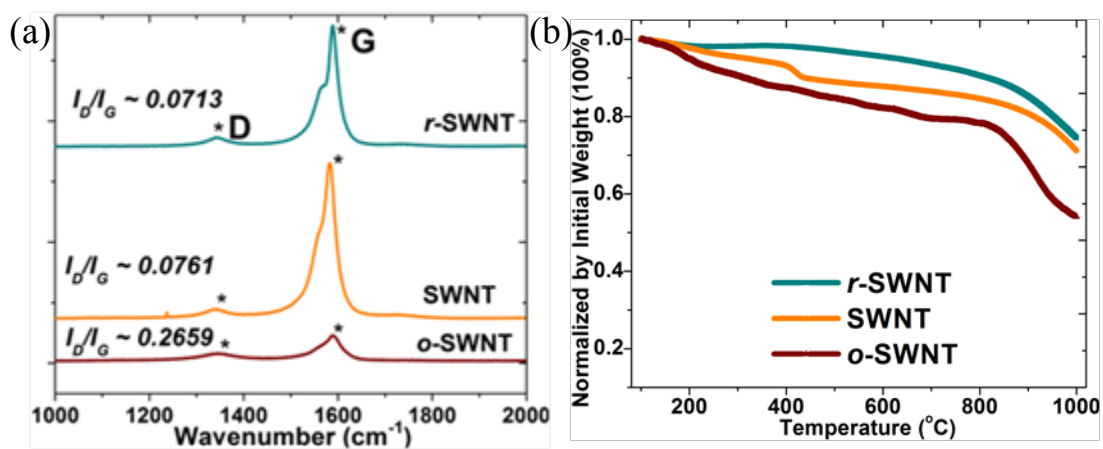


Figure 4.6 (a) Raman spectra over *r*-SWNT, SWNT, and *o*-SWNT; varied intensity ratio: I_D/I_G indicates structural changes. (b) TGA curves of the three SWNT samples: *r*-SWNT, SWNT, and *o*-SWNT. Results are shown within the temperature range from 100 to 1000 $^{\circ}\text{C}$.

TGA results are given in Figure 4.6b, and also confirm the varied chemical composition among the three SWNT samples. At 400 °C, *r*-SWNT lost 1.9 wt%, SWNT lost 6.9 wt%, and *o*-SWNT lost 12.7 wt%, which is the most.

Based on the characterization results of XPS, Raman and TGA, the *o*-SWNT sample contains the highest content of functional groups while the *r*-SWNT sample contains the least. Therefore, three SWNT samples with different contents of functional groups have been successfully prepared.

In order to investigate the effects of functional groups on the electrochemical behaviors, self-discharge tests, EIS, and CV were performed upon ECs built with SWNT, *r*-SWNT, and *o*-SWNT films as electrodes, and 1M TEABF₄(PC) as electrolyte.

4.4.2 Tuning self-discharge

The self-discharge results at room temperature (25 °C) and -25 °C are given in Figure 4.7.

As indicated by the fitting results, the voltage V decreases exponentially with time t ($V \propto e^{-t/\tau}$). Thus, the potential field ΔE is the dominant self-discharge driving force in all three capacitor systems built with the same organic electrolyte 1M TEABF₄(PC) and different SWNT electrodes (*r*-SWNT, SWNT and *o*-SWNT). Moreover, same as the previous study on the SWNT-TEABF₄ ECs in Chapter 3, the self-discharge processes are first dominated by the DPD model, and then switch to the SPD model. Tailoring on the functional groups does not alter the self-discharge mechanism for the SWNT based ECs with 1M TEABF₄/PC as electrolyte.

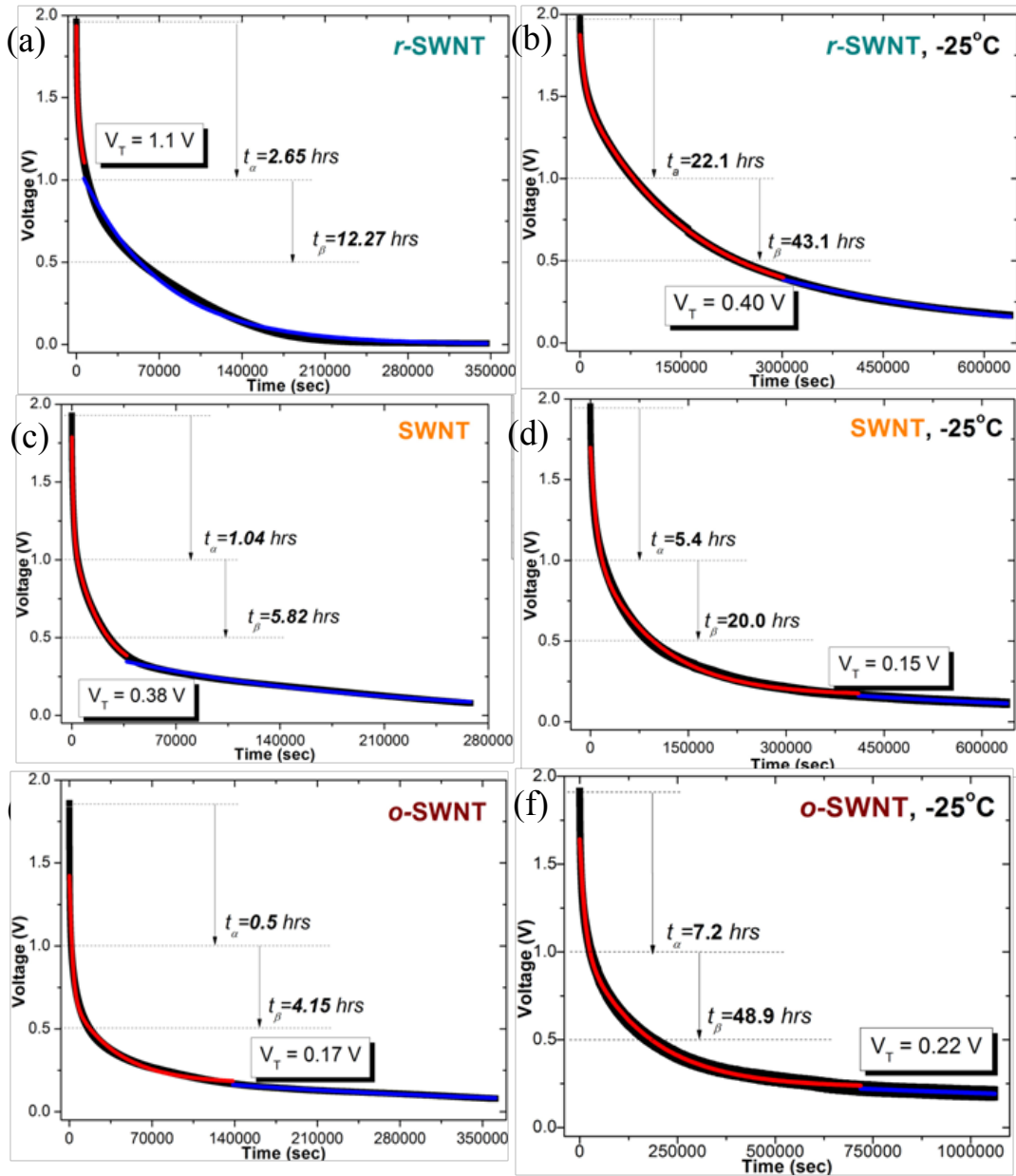


Figure 4.7 Self-discharge curves (black) of the r-SWNT EC, the SWNT EC, and the o-SWNT EC and fitting results: red by the DPD model and blue by the SPD model at room temperature (a, c, e) and -25 °C (b, d, f).

Fitting results are given in Figure 4.7, where the red line represents the DPD model and the relation between voltage V and self-discharge time t is described by Eqn. 3.1:

$$V = V_f \times e^{-t/\tau_f} + V_s \times e^{-t/\tau_s} + V_0 \quad \text{-----} \quad 3.1$$

The subscript “ f ” indicates the self-discharge portion with a smaller time constant τ_f while the subscript “ s ” corresponds to the portion with a larger time constant τ_s (*i.e.*, for the time constant, a larger value means a slower self-discharge rate). The blue line of the SPD model is simply described by Eqn. 3.2:

$$V = V \times e^{-t/\tau} + V' \quad \text{-----} \quad 3.2$$

All three ECs obey the transition of the “DPD to SPD” model. Hence, it can be deduced that mildly tailoring on the surface chemical states only changes the quantities of the functional groups, without altering the nature of the self-discharge mechanisms of the SWNT based ECs. However, certain characteristics describing the self-discharge processes such as the self-discharge rate and the energy retention ability have been affected.

The ability of energy retention, *i.e.* the self-discharge rate, changes as the amounts of functional groups changes. Comparing the self-discharge curves of the three ECs at room temperature (Figure 4.7a, c, e), it takes 1.04 hrs for the SWNT EC to drop from its initial voltage to 1 V, and another 5.82 hrs to drop to 0.5 V. For the EC built with *r*-SWNT, which has fewer functional groups, the self-discharge process is slower that it takes 2.65 hrs to reach 1 V and 12.27 hrs to 0.5 V. For the *o*-SWNT EC with more functional groups anchoring onto the nanotubes, the self-discharge

process proceeds in the fastest manner compared to the above two: it takes only 0.5 hrs to decrease to 1 V and another 4.15 hrs to self-discharge to 0.5 V.

Table 4.3 Three types of ECs: r-SWNT, SWNT, and o-SWNT ECs and their self-discharge fitting parameters.

| CNT electrodes | SDC Temperature | Specific Capacitance C (F/g) | $\frac{V_f}{V_{initial}} \times 100\%$ | Ratio of Non-sp ² carbon |
|----------------|-----------------|--------------------------------|----------------------------------------|-------------------------------------|
| <i>r</i> -SWNT | 20°C | 58.7 | 17.9% | 22.4% |
| | -25°C | 54.6 | 17.5% | |
| SWNT | 20°C | 52.2 | 34.0% | 32.1% |
| | -25°C | 52.9 | 32.2% | |
| <i>o</i> -SWNT | 20°C | 23.4 | 38.9% | 35.5% |
| | -25°C | 23.3 | 31.7% | |

Meanwhile, from the “DPD to SPD” fitting calculations (Table 4.3), it is shown that the percentage taken by the faster self-discharge ($V_f/V_{initial}$) increases from 17.9% for the *r*-SWNT EC to 38.9% for the *o*-SWNT EC at room temperature. A higher percentage of $V_f/V_{initial}$ corresponds to a faster self-discharge rate. Furthermore, by comparing the values of $V_f/V_{initial}$ with the percentages of functional groups (Table 4.3), it can be found that more functional groups correspond to a higher value of $V_f/V_{initial}$. Therefore, a higher content of functional groups leads to a higher ratio of the faster self-discharge “ $V_f/V_{initial}$ ” and a faster self-discharge rate

The discussion above on the functional groups and the DPD model fitting is consistent with our proposed scenario of co-existence of two types of ions within the ECs. As demonstrated in Chapter 3, at the SWNT surface areas where functional groups present, a relatively weak bonding will be created due to the enlarged distance

which weakens the static electrical force between the ions and the electrode surface. Two types of bondings are generated: the bonding between the ions and the intact electrode surface, which is stronger; and the bonding between the ions and the defective area of the electrode surface, which is relatively weaker because of the interference of the existing functional groups. Tight-bonded ions will diffuse more difficultly than the relatively loose-bonded ions and will slow down the corresponding self-discharge process. Therefore, with increasing the quantities of functional groups, the SWNT based ECs will self-discharge with a faster rate, as can be seen from the experimental results. Tuning self-discharge is simply realized through the surface chemistry modification.

Self-discharge tests have been conducted at -25 °C as well (Figure 4.7b, d, f), which demonstrate that the “DPD to SPD” model can be extended to a lower temperature range.

4.4.3 Electrochemical impedance spectroscopy

The effects of the functional groups on ionic movements are also reflected on the Nyquist plot (Figure 4.8a) and Bode phase plot (Figure 4.8b) based on the EIS tests. Radii of the semi-circle in the Nyquist plot is related to the charge transfer resistance on the electrode/electrolyte interface. A smaller semi-circle indicates a better ionic conductivity at the electrode-electrolyte interface.[33] In Figure 4.8a, *o*-SWNT with the most functional groups gives the largest radii of the semi-circle, indicating a relatively poor ionic conductivity because functional groups can weaken the electrostatic interaction between ions and charged carbon surface.

From the Bode phase plot (Figure 4.8b), there are two peaks: one main peak at ~1 kHz and a shoulder on its lower frequency side at room temperature. The existence

of two peaks instead of one suggests that there are two distinguishable groups of ions, one with a higher frequency and the other with a lower frequency [33, 34]. It can be seen that, the peak on the lower frequency side gradually fades from *o*-SWNT, to SWNT, to *r*-SWNT, corresponding to the decreasing amount of the loose-bonded ions from *o*-SWNT, to SWNT, to *r*-SWNT. Moreover, from the Bode phase plots at -25 °C, especially for the *o*-SWNT EC with the most functional groups, the two distinct peaks gradually merge into one peak. This can be explained as a result of the cryogenic depression of ionic mobility at the subzero temperature. The mobility of the loose-bonded ions and the tight-bonded ions have both been impaired and the loose-bonded ions has been impaired more and exhibit analogous behavior to the tight-bonded ions at -25 °C. Moreover, the equivalent circuit (Figure 4.8c) used for EIS spectra fitting

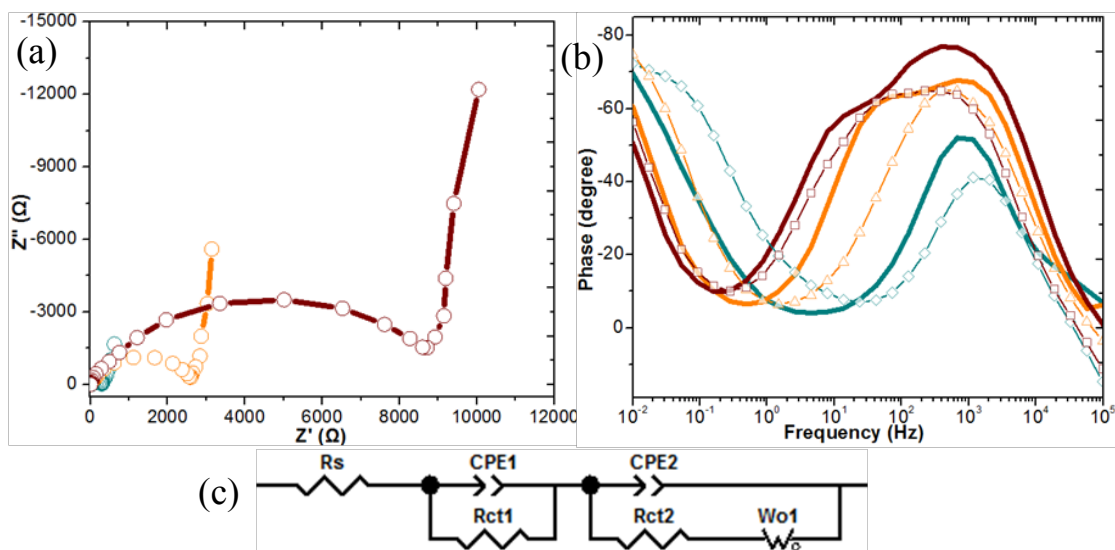


Figure 4.8 (a) EIS spectra at room temperature and (b) Bode phase plot at room temperature (solid lines) and at -25 °C (lines starred with “◇”, “Δ”, “□”) of *r*-SWNT (cyan), SWNT (orange) and *o*-SWNT (maroon). (c) Corresponding equivalent circuits.

comprises of two parallel components in series, also suggesting the existence of two types of ionic movements and consistent with the previous scenario of co-existence of two types of ions within the ECs.

4.4.4 Cyclic voltammetry

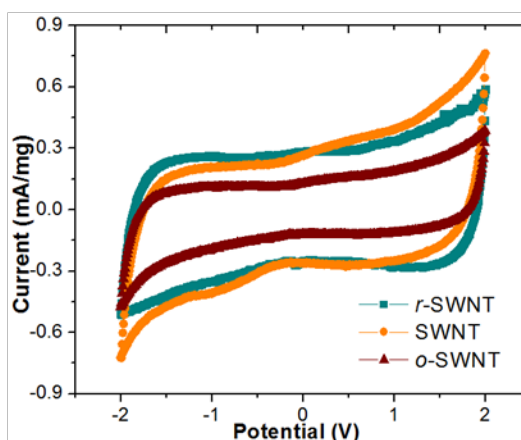


Figure 4.9 CV curves of *r*-SWNT (cyan), SWNT (orange) and *o*-SWNT (maroon) at the scan rate of $10 \text{ mV}\cdot\text{s}^{-1}$.

As calculated from the CV curves (Figure 4.9), the *r*-SWNT EC gives the highest value in specific capacitance of $58.7 \text{ F}\cdot\text{g}^{-1}$ while the *o*-SWNT EC gives the lowest value of $23.4 \text{ F}\cdot\text{g}^{-1}$. This phenomenon is different from the reported work, which claimed that through rigorous oxidation treatments (usually with highly oxidizing nitric acid treatment), the specific capacitance increased[18, 35]. It is reasonable that in those highly oxidized SWNT samples, much more electrode/electrolyte interfaces were formed for the double-layer capacitive structures, and also more pseudocapacitance was involved, therefore, a higher specific

capacitance was obtained. What is worth noting and may be the key factor which differentiates our samples to theirs is that our samples are mildly reduced or oxidized purposely to preserve the integrity of nanotube structures. The tangled feature of the SWNT films is preserved and the chemical composition only changes within a small range (13.2% for the functional groups). Moreover, the SSA among the three samples changes after reduction or oxidation, but does not change significantly (Table 4.1) and the CV curves (Figure 4.9) give no obvious pseudocapacitive peaks from -2 to 2 V.

On the other hand, as evidenced in the DPD model, functional groups can baffle the ionic interactions at the electrode/electrolyte interface. The double-layer structures formed on the areas where functional groups present will lead to a weak interaction between the electrode and electrolytic ions, and reduce the stored energy. Therefore, the increased amount of the functional groups would be the key for the decrease in specific capacitance due to the weakened electrode/electrolytic ion interaction within the double-layer structures.

4.5 Conclusions

Through a systematic experimental design and analysis, we have further validated the proposed “DPD to SPD” model for the self-discharge of SWNT based ECs using SWNT film electrodes with controlled functional groups ranging from 8.9% to 22.1%, even when the self-discharge was carried out at a low temperature of -25 °C. The DPD process is the result of the functional groups that create a relatively weak bonding between ions and the charged electrode surface. More functional groups lead to a faster self-discharge. Tuning on self-discharge has been demonstrated for the first time. With functional groups decreasing by 13 %, the self-discharge time from 2.0 to 1.0 V is extended by 5 times.

In summary, we have demonstrated that SWNT ECs built with different SWNT samples all obey the potential driving model and experience a transition from the DPD model to the SPD model. Varied functional groups do not alter the self-discharge mechanism, however, affect the self-discharge rate based on the DPD model. Most importantly, the underlying relation between the DPD model and the functional groups of SWNT electrode materials is quantitatively investigated and provides guidance on designing SWNT based ECs with various energy retentions. The tuning capability of the self-discharge process will benefit potential applications of ECs in energy storage.

ACKNOWLEDGMENTS

The author wishes to thank the following individuals for their contributions to this chapter. Chuan Cai prepared the SWNT samples, performed the TGA analysis and helped with the self-discharge measurements. Jinwen Qin prepared the SWNT samples. Trong Pham helped with the BET measurements. Robert Forest and Zachary Voras helped with the XPS measurements. This chapter was previously published in ref. [36], reprinted with permission from Elsevier, copyright 2014.

REFERENCES

- [1] Zhang, Q., J. Rong, and B. Wei, *A divided potential driving self-discharge process for single-walled carbon nanotube based supercapacitors*. RSC Advances, 2011. **1**(6): p. 989-994.
- [2] Kaempgen, M., et al., *Printable thin film supercapacitors using single-walled carbon nanotubes*. Nano Letters, 2009. **9**(5): p. 1872-1876.
- [3] Byon, H.R., et al., *Role of oxygen functional groups in carbon nanotube/graphene freestanding electrodes for high performance lithium batteries*. Advanced Functional Materials, 2013. **23**(8): p. 1037-1045.
- [4] Kundu, S., et al., *Thermal stability and reducibility of oxygen-containing functional groups on multiwalled carbon nanotube surfaces: a quantitative high-resolution XPS and TPD/TPR study*. The Journal of Physical Chemistry C, 2008. **112**(43): p. 16869-16878.
- [5] Zhu, H. and B. Wei, *Direct fabrication of single-walled carbon nanotube macrofilms on flexible substrates*. Chemical Communications, 2007. **29**: p. 3042-3044.
- [6] Xie, H., et al., *Nanofluids containing multiwalled carbon nanotubes and their enhanced thermal conductivities*. Journal of Applied Physics, 2003. **94**(8): p. 4967-4971.
- [7] Jiang, K., et al., *Selective attachment of gold nanoparticles to nitrogen-doped carbon nanotubes*. Nano Letters, 2003. **3**(3): p. 275-277.
- [8] Kim, Y.J., et al., *Electrical conductivity of chemically modified multiwalled carbon nanotube/epoxy composites*. Carbon, 2005. **43**(1): p. 23-30.
- [9] Stankovich, S., et al., *Synthesis of graphene-based nanosheets via chemical reduction of exfoliated graphite oxide*. Carbon, 2007. **45**(7): p. 1558-1565.
- [10] Li, Y., et al., *An oxygen reduction electrocatalyst based on carbon nanotube-graphene complexes*. Nature Nanotechnology, 2012. **7**(6): p. 394-400.
- [11] Cao, A., et al., *Hydrogen storage of dense-aligned carbon nanotubes*. Chemical Physics Letters, 2001. **342**(5): p. 510-514.

- [12] Robinson, J.A., et al., *Role of defects in single-walled carbon nanotube chemical sensors*. Nano Letters, 2006. **6**(8): p. 1747-1751.
- [13] Modi, A., et al., *Miniaturized gas ionization sensors using carbon nanotubes*. Nature, 2003. **424**(6945): p. 171-174.
- [14] Stankovich, S., et al., *Graphene-based composite materials*. Nature, 2006. **442**(7100): p. 282-286.
- [15] Viswanathan, G., et al., *Single-step in situ synthesis of polymer-grafted single-wall nanotube composites*. Journal of the American Chemical Society, 2003. **125**(31): p. 9258-9259.
- [16] Zhu, J., et al., *Improving the dispersion and integration of single-walled carbon nanotubes in epoxy composites through functionalization*. Nano Letters, 2003. **3**(8): p. 1107-1113.
- [17] Qu, D., *Studies of the activated carbons used in double-layer supercapacitors*. Journal of Power Sources, 2002. **109**(2): p. 403-411.
- [18] Ye, J.-S., et al., *Electrochemical oxidation of multi-walled carbon nanotubes and its application to electrochemical double layer capacitors*. Electrochemistry Communications, 2005. **7**(3): p. 249-255.
- [19] Boehm, H., *Some aspects of the surface chemistry of carbon blacks and other carbons*. Carbon, 1994. **32**(5): p. 759-769.
- [20] Boehm, H., *Surface oxides on carbon and their analysis: a critical assessment*. Carbon, 2002. **40**(2): p. 145-149.
- [21] Barton, S., et al., *Acidic and basic sites on the surface of porous carbon*. Carbon, 1997. **35**(9): p. 1361-1366.
- [22] Ajayan, P., et al., *Opening carbon nanotubes with oxygen and implications for filling*. Nature, 1993. **362**, 522-525.
- [23] Banerjee, S., T. Hemraj-Benny, and S.S. Wong, *Covalent surface chemistry of single-walled carbon nanotubes*. Advanced Materials, 2005. **17**(1): p. 17-29.
- [24] Zhang, Q., et al., *The governing self-discharge processes in activated carbon fabric-based supercapacitors with different organic electrolytes*. Energy & Environmental Science, 2011. **4**(6): p. 2152-2159.
- [25] Ricketts, B.W. and C. Ton-That, *Self-discharge of carbon-based supercapacitors with organic electrolytes*. Journal of Power Sources, 2000. **89**(1): p. 64-69.

- [26] Conway, B.E., W. Pell, and T. Liu, *Diagnostic analyses for mechanisms of self-discharge of electrochemical capacitors and batteries*. Journal of Power Sources, 1997. **65**(1): p. 53-59.
- [27] Yang, D., et al., *Chemical analysis of graphene oxide films after heat and chemical treatments by X-ray photoelectron and micro-Raman spectroscopy*. Carbon, 2009. **47**(1): p. 145-152.
- [28] Zhang, J., et al., *Effect of chemical oxidation on the structure of single-walled carbon nanotubes*. The Journal of Physical Chemistry B, 2003. **107**(16): p. 3712-3718.
- [29] Toebes, M.L., et al., *The influence of oxidation on the texture and the number of oxygen-containing surface groups of carbon nanofibers*. Carbon, 2004. **42**(2): p. 307-315.
- [30] Pulido, A., et al., *Reconstruction of the carbon sp² network in graphene oxide by low-temperature reaction with CO*. Journal of Materials Chemistry, 2012. **22**(1): p. 51-56.
- [31] Rosca, I.D., et al., *Oxidation of multiwalled carbon nanotubes by nitric acid*. Carbon, 2005. **43**(15): p. 3124-3131.
- [32] Kim, U.J., et al., *Raman and IR spectroscopy of chemically processed single-walled carbon nanotubes*. Journal of the American Chemical Society, 2005. **127**(44): p. 15437-15445.
- [33] Li, X., J. Rong, and B. Wei, *Electrochemical behavior of single-walled carbon nanotube supercapacitors under compressive stress*. ACS Nano, 2010. **4**(10): p. 6039-6049.
- [34] Brevnov, D.A. and T.S. Olson, *Double-layer capacitors composed of interconnected silver particles and with a high-frequency response*. Electrochimica Acta, 2006. **51**(7): p. 1172-1177.
- [35] Chen, X., et al., *Improvement in electrochemical capacitance of carbon materials by nitric acid treatment*. Journal of Power Sources, 2008. **184**(2): p. 668-674.
- [36] Zhang, Q., et al., *Tunable self-discharge process of carbon nanotube based supercapacitors*. Nano Energy, 2014. **4**: p.14-22.

Chapter 5

SELF-DISCHARGE OF GRAPHENE BASED ELECTROCHEMICAL CAPACITORS

5.1 Introduction

Electrode materials with high SSA accessible to electrolytic ions and superior capability for charge transport are favored for designing ECs with high energy densities and power densities. As repeatedly confirmed in the previous chapters, dominant self-discharge model is determined by the competition of the two driving forces: the ECs with a high specific capacitance yet poor charge transportation are prone to be dominated by the diffusion control model; while the ECs with a low specific capacitance yet good charge transportation are prone to be dominated by the potential driving model. Therefore, the SSA and the electrical conductivity are also closely associated with the self-discharge behaviors of the ECs in addition to energy density and power density.

Research in previous chapters indicates that ACF prevails over SWNT with a higher SSA and a higher specific capacitance, while SWNT prevails over ACF with a higher electrical conductivity and in turn, a higher power density[1, 2]. In addition to ACF and SWNT, graphene and graphene-based materials have already shown their exceptional advantages as electrode materials for ECs due to an extensive surface area and a superior electronic conductivity stemming from their two-dimensional structures. It has also been demonstrated that the hydrated GO can serve as a solid electrolyte for ECs[3, 4], based on the trapped water and ions within GO layers.

However, no report is available up to date on the self-discharge behaviors of graphene based ECs. Investigation of the self-discharge of the GO based solid-state ECs is of most significance, not only because it contributes to knowledge of the self-discharge behaviors of the ECs of the restricted ionic mobility, but also because it benefits the comprehension of the ionic diffusion in the solid-state ECs.

5.2 Graphene

Pristine graphene is structured of two-dimensional honeycomb carbon lattices, in which the sp^2 hybridized carbon atoms are arranged in hexagonal rings. Graphene layers can be bonded to each other by van der Waals interaction to form multilayer structures.

Graphene can be obtained through physical methods as well as chemical methods. Physical methods include mechanically exfoliating graphene from bulk graphite by utilizing external forces such as tape-peeling or ultrasonication in proper solvents [5, 6]. The graphene obtained by the mechanical exfoliation is usually with high quality but a low yield. Graphene can also be synthesized from the CVD method[7, 8]. In the CVD process, alkanes or alkenes serve as the carbon source. The decomposition of those hydrocarbon gases usually occurs at a very high temperature (higher than 1000 °C)[9]. CVD-synthesized graphene is formed through the re-decomposition of carbon atoms generated from the decomposition of the hydrocarbons on pretreated metal foils (nickel or copper thin foils with a high purity[10]). The CVD method is used to obtain graphene with a high quality and with a single layer or multi-layers.

Another chemical method to produce graphene is the modified Hummer's method. The graphene produced by this method is with a large yield and highly-

defective. For the modified Hummer's method, natural graphite flakes are first oxidized and intercalated with acids or other chemical species to enlarge the interlayer spacing (from 0.34 nm in graphite to > 0.6 nm in the expandable graphite oxide[11]) for facile exfoliation, followed by exfoliation in liquid phase to make GO. Sometimes, thermal treatments are performed prior to the exfoliation to expand the graphite more. Yang *et al.*[12] reported a low temperature exfoliation of GO assisted with vacuum, which skips the step of exfoliation in liquid phase and generates few-layer graphene oxide directly.

GO synthesized with the modified Hummer's method needs to be reduced to rGO before being used as electrode materials in ECs. There are several methods to reduce GO, such as the photocatalytical reduction using mercury lamp irradiation[13] and the controllable laser reduction[3, 14]. Compared to the physical reduction methods, chemically reducing rGO with reducing agents (sodium borohydride, hydrazine, etc) is of low cost and high yield.

The graphene based films can be feasibly synthesized through filtering the colloidal dispersions. Graphene-based films have drawn extensive attentions for applications in ECs. Shi *et al.*[15] prepared composite films of rGO and polyaniline nanofibers, which showed large electrochemical capacitance of $210 \text{ F}\cdot\text{g}^{-1}$ with 1M H_2SO_4 (aq) as electrolyte. Dai *et al.*[16] reported a hybrid film of polymer (PEI)-modified graphene sheets and CNTs, which exhibits a specific capacitance of $120 \text{ F}\cdot\text{g}^{-1}$ based on pure double layers with 1M H_2SO_4 (aq) as electrolyte. Similar specific capacitance was reported by Ruoff *et al.*[17], the chemically activated rGO films exhibited $120 \text{ F}\cdot\text{g}^{-1}$ with the organic electrolyte 1M TEABF₄ (AN). Moreover, the flexibility of the graphene based films grants the flexibility to the microcapacitors

fabricated on them, which are favored for applications in flexible electronic devices. There have already been reports on using the lightscribing reduced GO as electrodes with a gelled electrolyte by El-Kady *et al.* [14], and on the one-body GO based microcapacitor by Ajayan *et al.*[3], which directly utilized the hydrated GO as the solid electrolyte.

In this chapter, laser reduced GO films with no foreign electrolytes are investigated for the self-discharge behaviors with a restricted ionic mobility.

5.3 Experimental Section

5.3.1 Sample preparation

GO was prepared by the modified Hummer's method: natural graphite flakes (10 mesh, Alfa Aesar) served as the carbon sources, and were treated by 5 days of oxidization and exfoliation with KMnO_4 in a concentrated sulfuric acid, until brownish-colored colloidal dispersion of GO was obtained. Extensive washing with centrifuge and dialysis tubing were followed to remove the excess acids and salts.

As shown in Figure 5.1, the GO films were fabricated by vacuum filtration of a measured amount of the obtained GO solutions through a PVDF membrane filter (25 mm in diameter, 0.2 μm pore size, Sterlitech), followed by air drying and peeling from the filter. The thickness of the GO films is around 5 μm for all measurements reported here unless otherwise stated.

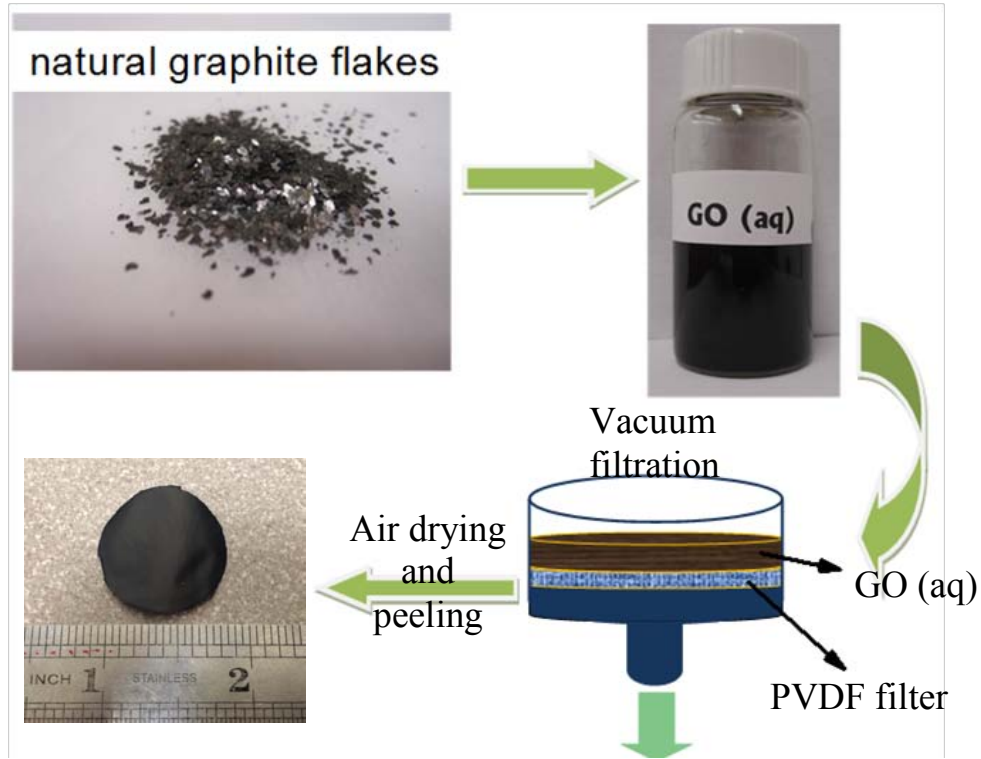


Figure 5.1 Schematic of the fabrication of graphene oxide films.

5.3.2 Near infrared laser workstation set-up

The reduction of the GO films was complemented with a laser source of 780 nm wavelength (near infrared, NIR). Its power output is tunable and up to 100 mW. Motorized translation stages were combined to realize programmed-control reduction. A schematic of the laser workstation is given in Figure 5.2a. During the reduction, nitrogen gas was used as the protection gas.

As shown in Figure 5.2b, after reduction, the original black surface of the GO film became grey.

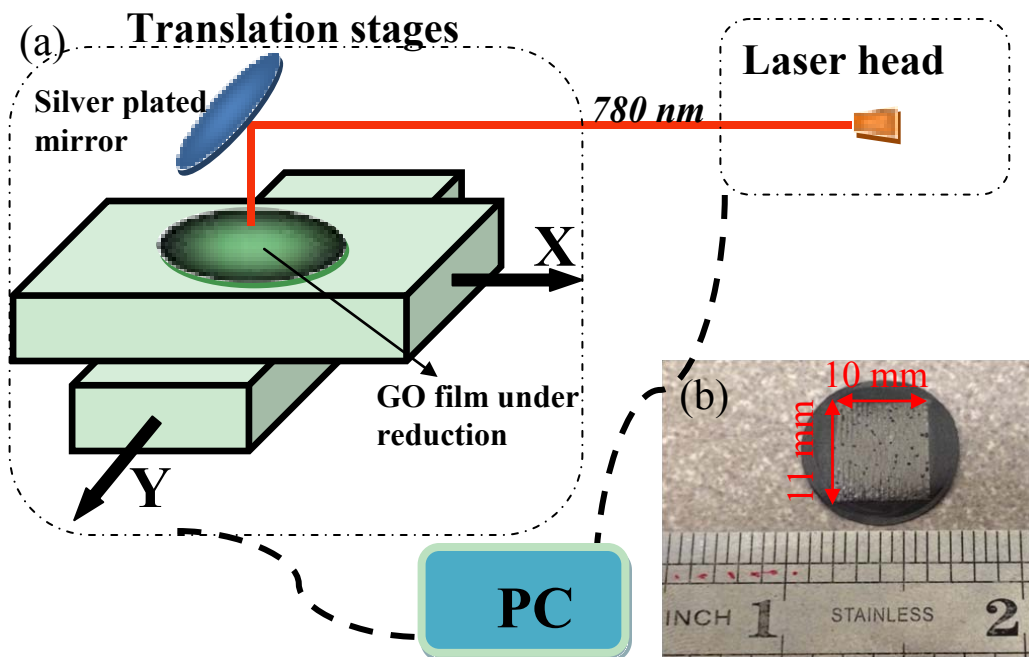


Figure 5.2 (a) Schematic representation of the laser workstation for GO film reduction. (b) Digital camera image of LR-GO film after laser reduction and punched into 13 mm in diameter.

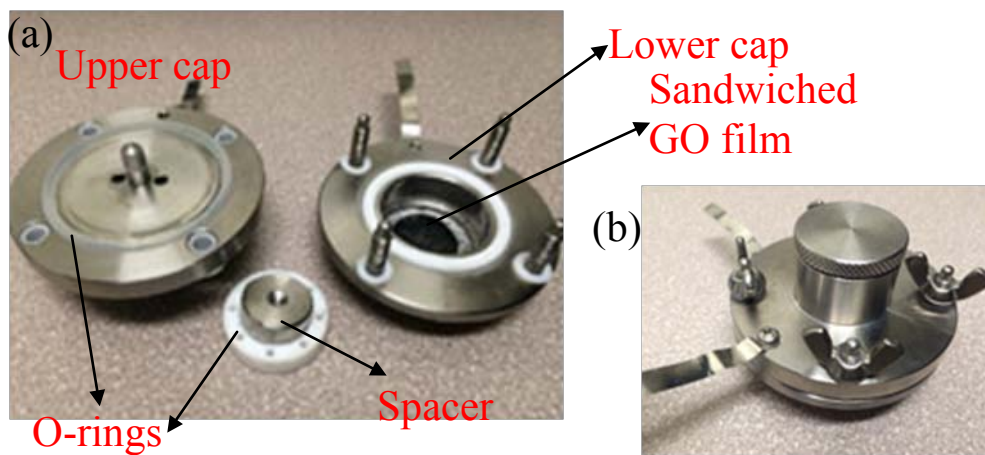


Figure 5.3 Digital camera images taken of (a) the parts of the test cell and (b) the assembled test cell.

5.3.3 Characterizations and electrochemical testing

The surface morphology and microstructures of the GO films and the laser reduced (LR)-GO films were characterized by SEM (AURIGA 60 Crossbeam FIB-SEM). XRD (Philips X'Pert X-ray diffractometer) was applied to characterize the layering structure of the films. Raman (Bruker Senterra AFM/Raman Microscope) was conducted using an excitation wavelength of 532 nm on the GO and LR-GO samples. XPS was applied to analyze the reduction effects and study the functional groups of the GO and LR-GO films.

As shown in Figure 5.3, the LR-GO films were assembled in the test cell for electrochemical measurements, including CV, EIS and galvanostatic charge/discharge/selfdischarge. Increasing the water content in the GO films can greatly enhance the ionic conductivity[3]. Therefore, the LR-GO films were kept in a desiccator with 80% relative humidity, where saturated aqueous solution of KNO_3 was applied, for the water adsorption before the electrochemical tests.

5.4 Results and Discussion

5.4.1 Microstructure and composition analysis

The color of the GO film changes from black to grey after laser reduction (see Figure 5.2b). As shown in Figure 5.4a, the surface morphology of the GO film has changed from the wrinkled surface to a relatively flat surface after laser reduction. As shown in Figure 5.4b, on the rGO surface, a few rGO layers become partially detaching from the originally intact surface of the GO film.

From the cross section views (Figure 5.5), the GO films comprised of densely packed layers of GO sheets. After the reduction, the packed layers expand greatly by ~ 4.6 times from $5.4 \mu\text{m}$ to $24.85 \mu\text{m}$ and present a more porous structure. During the

laser reduction, the volume of the GO film expands due to the heat and gas generated from the decomposition of oxygenated functional groups, leading to a flat surface and an expanded thickness. Energy-dispersive X-ray spectroscopy (XEDS) collected on the cross-sectional areas on the GO film and the LR-GO film exhibits a decrease in the atomic percentage of oxygen from ~ 37 at.% to ~ 28 at.% (Figure 5.5d). The reduction is through-the-thickness.

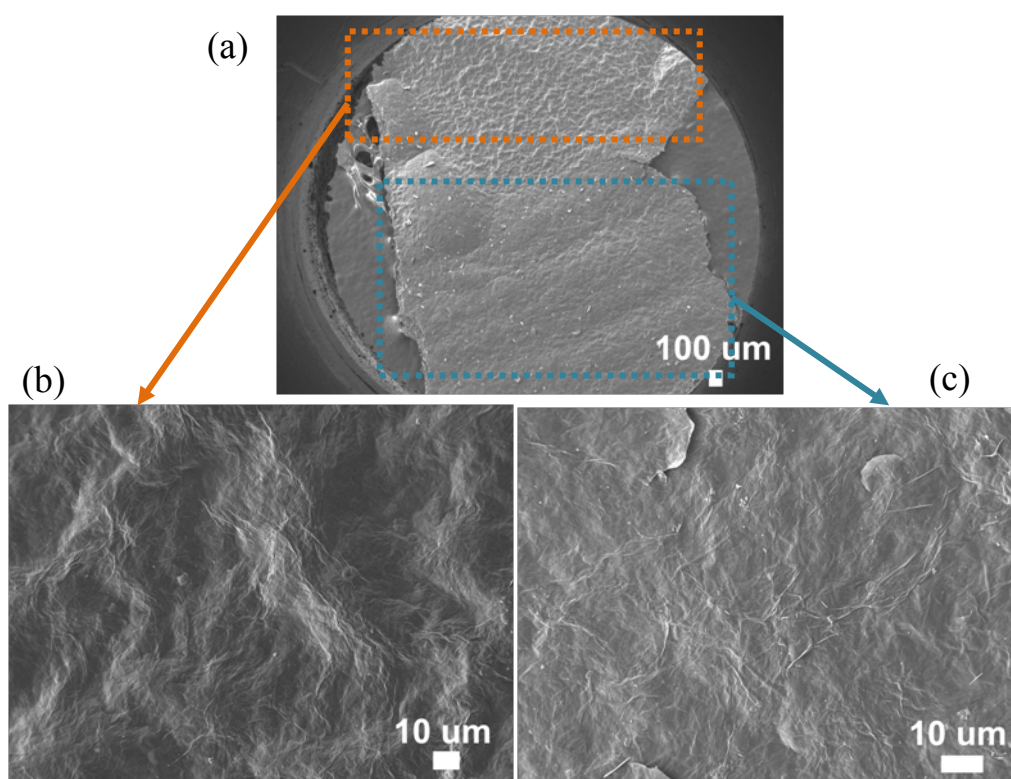


Figure 5.4 (a) SEM image of GO surface before (yellow box) and after (cyan box) laser reduction. (b) Zoom-in SEM view on the un-reduced area; (c) Zoom-in SEM view on the reduced area.

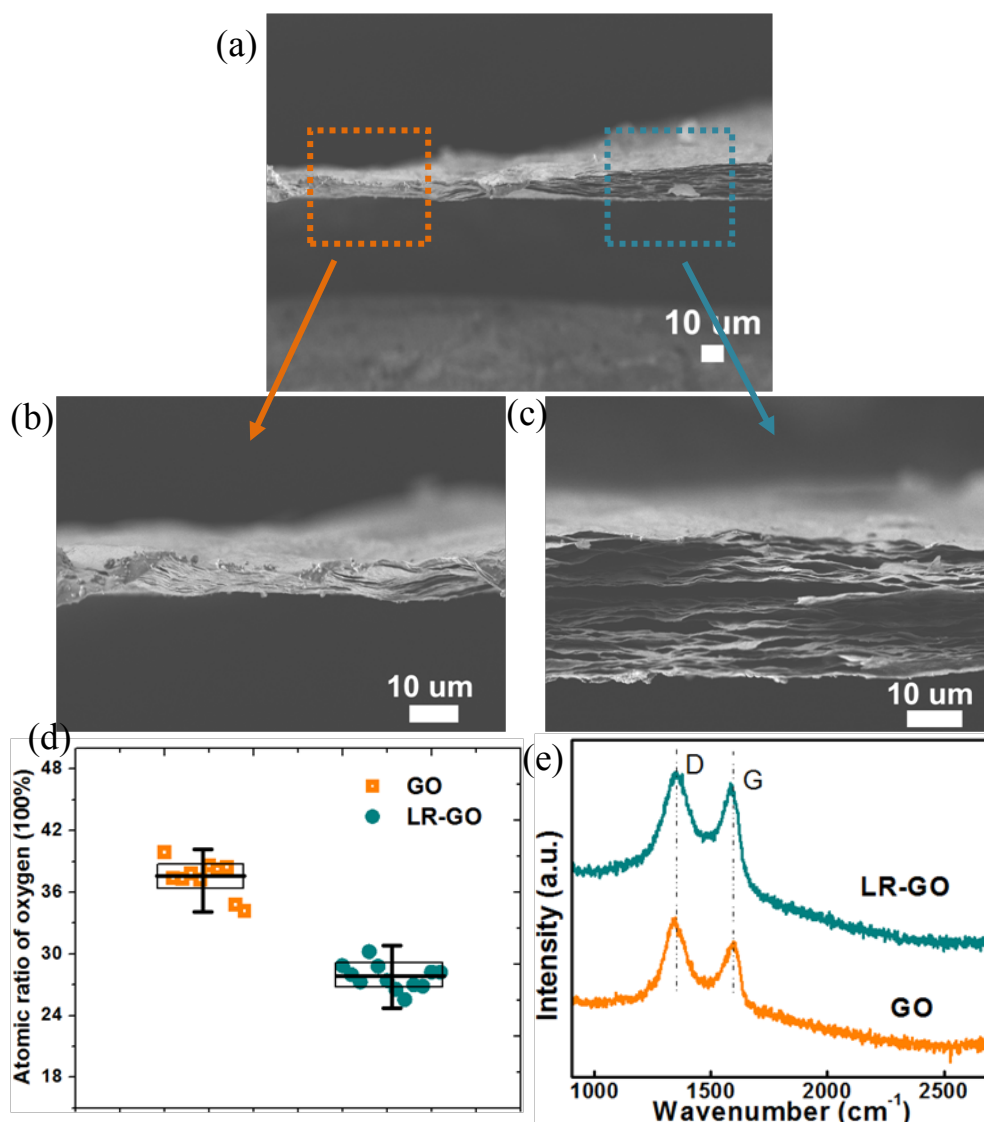


Figure 5.5 (a) SEM image of the cross sectional view of the GO film before (yellow box) and after (cyan box) laser reduction; (b) Zoom-in SEM view on the unreduced part; (c) Zoom-in SEM view on the reduced part, which shows a much expanded structure; (d) XEDS results collected on randomly picked areas on the surface and cross-section of the GO and the LR-GO films; (e) Raman spectra collected on the GO and LR-GO films.

The reduction of the GO film has also been confirmed by the Raman measurements. Raman spectra were collected using a laser with an excitation wavelength of 532 nm, showing that I_D/I_G decreased after the laser treatment (Figure 5.5e and Table 5.1). The D band is induced by the structural disorder while the G band is related to the aromaticity of the graphene lattice[18, 19]. The increasing of the intensity of G band indicates the formation of more graphitic lattice structures after laser reduction and is consistent with the enhanced electronic conductivity as measured on the LR-GO film.

Chemical identification of the GO and LR-GO film samples were addressed by XPS, and results are given in Table 5.1 and Figure 5.6. Comparing the C1s and O1s peaks in the survey scan (Figure 5.6a), the O/C ratio decreases from 0.41 to 0.32 (Table 5.1), confirming the reducing effect of the laser treatment.

Table 5.1 Characterization results of the GO films and LR-GO films.

| | XPS | | | | | | XEDS | Raman |
|-------|-------|--------------------|-----|------|------|------|----------|-----------|
| | Ratio | Atomic % | | | | | Atomic % | |
| | O/C | sp ² -C | C-N | C-O | C=O | COOH | Oxygen | I_D/I_G |
| GO | 0.41 | 53.9 | 0 | 25.7 | 16.1 | 4.2 | 37.42% | 1.63 |
| LR-GO | 0.32 | 67.3 | 7.2 | 8.4 | 10.1 | 6.9 | 27.75% | 1.40 |

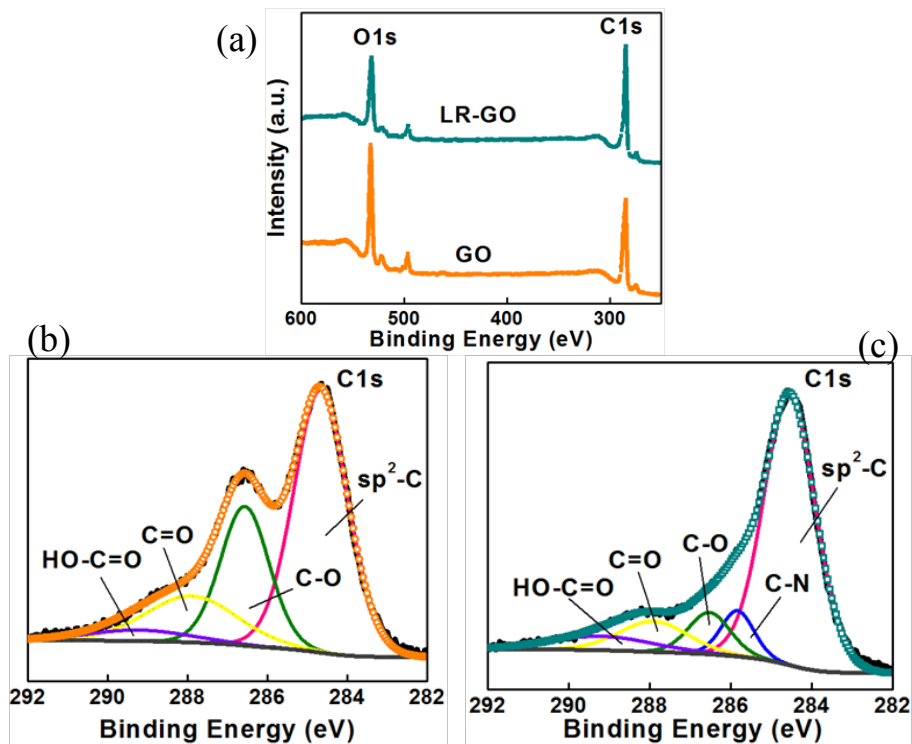


Figure 5.6 (a) XPS survey of the GO film and the LR-GO film; C 1s binding energy (BE) regions of (b) the GO film and (c) the LR-GO film.

Furthermore, deconvoluting the C 1s region in high-resolution scans (Figure 5.6b and c) reveals the existence of various functional groups including C-O (~286.5 eV), C=O (~287.9 eV), and COOH (~289.3 eV) [20-22]. Quantitative results on the percentage of each functional group are given in Table 5.1. For both the GO and LR-GO samples, sp² carbon takes up the major portion, from 53.9% of the GO film to 67.3% of the LR-GO film, while the percentage of oxygenated functional groups decreases significantly from a total of 46.1% of the GO film to 25.5% of the LR-GO film. The functional groups of C-N (~285.9 eV) are also present in the LR-

GO due to the usage of nitrogen as protection gas. Enhancement in the percentage of sp^2 carbon as well as the decrease in the functional groups indicates a better graphitization and restoration in the carbon lattice structures[23].

Based on the characterization results of XEDS, Raman, and XPS, the reduction effects of the laser treatment have been demonstrated by the reduced amount of functional groups and enhanced graphitization in the lattice structure. The obtained LR-GO film is with expanded, porous layering structures and contains ~25% of the functional groups. Prior to electrochemical characterizations, the LR-GO films are stored in a desiccator with a ~80% relative humidity for water adsorption through the hydrogen bonding with the functional groups[24].

5.4.2 Electrochemical Capacitive behaviors of the LR-GO EC

The as-prepared LR-GO film is directly used as an EC without using any other electrolytes. Galvanostatic charge/discharge curves (Figure 5.7a) and the CV cycles (Figure 5.7c) demonstrate the electrochemical capacitive behaviors of the LR-GO EC. Because of the large resistance from the highly restricted ionic mobility, the LR-GO EC can only be charged /discharged using a current density of $200 \text{ mA}\cdot\text{g}^{-1}$. The obtained energy density for the LR-GO EC is around $130 \text{ uAh}\cdot\text{g}^{-1}$ for the charging and $60 \text{ uAh}\cdot\text{g}^{-1}$ for the discharging (considering the total weight of the LR-GO film). The difference between the charge and discharge energy density should be the result of non-elastic interactions among ions during discharging, which consume the charged energy and dissipate as heat. The specific capacitance as converted from the energy density is $9.7 \text{ uF}\cdot\text{cm}^{-2}$ for the charging and $4.5 \text{ uF}\cdot\text{cm}^{-2}$ for the discharging (considering the area of the reduced surface). The energy density stored in the LR-GO

EC is substantially lower than other reported $0.4\text{-}2\text{ mF}\cdot\text{cm}^{-2}$ [3, 25, 26] or the obtained $\sim 0.86\text{ mF}\cdot\text{cm}^{-2}$ of the sandwiched GO film discussed in Chapter 6.

The LR-GO film consists of packed layers of partially reduced GO, where some functional groups still remain on the reduced GO layers. Because of the hydrophilicity of the heteroatoms and the polarized functional groups, water from the external environment can be adsorbed onto to the rGO layers, which generate moveable ions (such as H^+) through the hydrolysis of the functional groups[3].

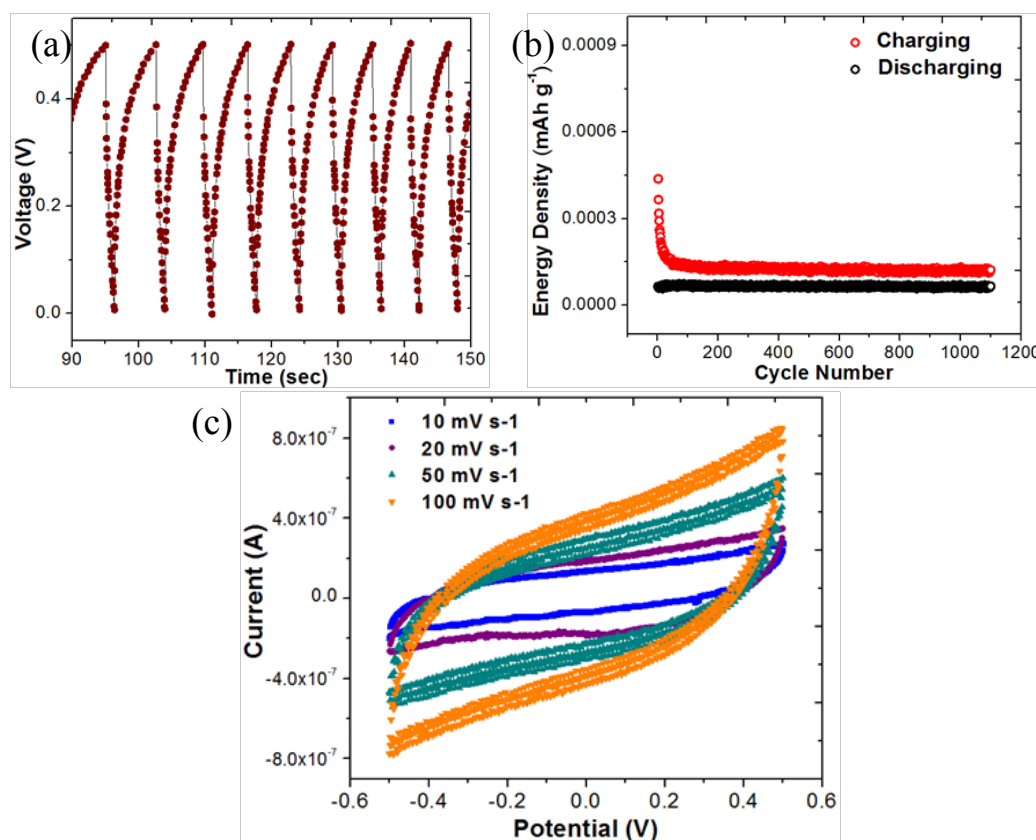


Figure 5.7 (a) Galvanostatic charge/discharge curves and (b) the corresponding charge/discharge energy densities of the LR-GO EC with a charge current density of $0.2\text{ mA}\cdot\text{g}^{-1}$. (c) CV curves of the LR-GO EC with different scan rate from 10 to 100 mV s^{-1} .

Together with residual metal ions (such as Na^+ , Fe^{2+} from the Hummer's synthesis and detected by the XEDS), ions including H^+ should exist in the LR-GO film. Meanwhile, the water molecules can also incorporate into the ionic conducting skeleton or wrap around those ions, assisting the ionic diffusion[27-29]. Hence, in the LR-GO film based ECs, it is expected that energy is stored through the movement of the ions under the assistance of water molecules. The ions/molecules with charge form double layers on the rGO layers, and the double layers on the numerous rGO layers contribute to the total energy storage. Laser reduction greatly decreases the amount of the originally inserted water molecules and functional groups between the GO layers, leading to a limited ionic mobility and, therefore the low energy density.

As the voltage window is limited within 0.5 V, no obvious redox reactions present in the galvanostatic charge/discharge curves as well as in the CV curves, therefore the pseudocapacitance can be ruled out of the dominating capacitive mechanisms for the LR-GO film based ECs, and this leaves us with two possible driving forces: the ionic concentration gradient $\partial c/\partial x$ and the potential field ΔE . As a result of the ultra-low specific capacitance, a small driving force of the ionic concentration gradient $\partial c/\partial x$ is expected.

5.4.3 Self-discharge behaviors of the LR-GO EC

The self-discharge curves of the LR-GO EC are given in Figure 5.8. As shown in Figure 5.8a, a large IR drop of ~ 0.22 V from the set 0.5 V is observed, suggesting a poor charge transportation within the LR-GO EC. On the other hand, with holding the voltage at 0.5 V for 12 hours prior to self-discharge, the IR drop is only 0.03 V, and self-discharge proceeds in a much slower rate. The phenomenon indicates that the stabilization effects of constant charging with small charge current during the voltage

holding, and it should be related to a more dense distribution of ions in the double layers, similar to the “blocking effects” of the ACF-LiPF₆ EC when the EC is charged with a small I_C (Section 2.4.3.1).

Fitting of the self-discharge curves demonstrates that the LR-GO EC is dominated by the “DPD to SPD” model (proposed for the SWNT-TEABF₄ EC in Chapter 3), where potential field ΔE acts as the dominant driving force due to the

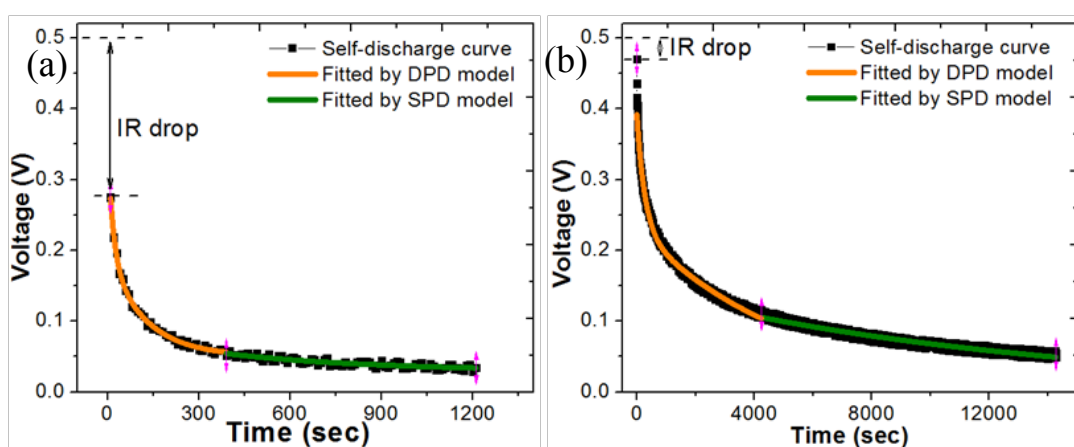


Figure 5.8 Self-discharge curves of the LR-GO films, with charge current density of $0.2 \text{ mA} \cdot \text{g}^{-1}$, (a) self-discharge after two and a half cycle of charge/discharge; (b) self-discharge after holding the voltage at 0.5 V for 12 hours following the two and a half cycle of charge/discharge.

Table 5.2 Fitting parameters calculated based on the DPD to SPD model.

| Self-discharge curve | $V_{initial}$ (V) | $V_f/V_{initial}$ | τ_f (sec) | τ_s (sec) |
|----------------------|-------------------|-------------------|----------------|----------------|
| A | 0.28 | 0.59 | 18 | 122 |
| B | 0.47 | 0.34 | 270 | 5314 |

*Curve A and curve B are the self-discharge curves displayed in Figure 5.8a and b.

small ionic concentration gradient $\partial c/\partial x$. The parameters calculated based on the fitting are given in Table 5.2. The fitting again demonstrates that the ECs with a poor specific capacitance and a relatively high voltage are expected to self-discharge under the potential field driving.

As demonstrated in Chapter 4, in the SWNT-TEABF₄ ECs, division in the potential driving process is ascribed to the functional groups attached on the SWNT surfaces, which create varied interactions between electrolytic ions and the charged electrode surfaces. While in the LR-GO ECs, the coverage of the functional groups on the rGO layer is ~35% (C-N included). The ratio of $V_f/V_{initial}$ represents the percentage of the weak-bonded ions (Section 3.4.2.2 and Section 4.4.2). As given in Table 5.2, $V_f/V_{initial} = 0.34$ for the self-discharge process after holding the voltage. The ratio is very close to the coverage of the functional groups and further indicates the stabilization effects of voltage holding, where the ions achieve full interaction with the intact graphene surfaces and the surfaces where functional groups present. Conclusively, the DPD model of the LR-GO EC is ascribed to the existence of the functional groups.

5.4.4 Electrochemical impedance spectroscopy

EIS was performed over the frequency range from 100 kHz to 10 mHz. Unlike the usual Nyquist plots obtained on ECs, there is no obvious semi-circle on the high frequency side from the Nyquist plot (Figure 5.9a), suggesting the poor capacity of the LR-GO EC. Moreover, instead of the Warburg line expected at the low frequency side, it exhibits a line with curvature in Figure 5.9a. Straight Warburg line indicates a good ionic diffusion of EC systems. Therefore, the absence of the straight Warburg line indicates the poor ionic diffusion in the LR-GO EC. More details on the ionic

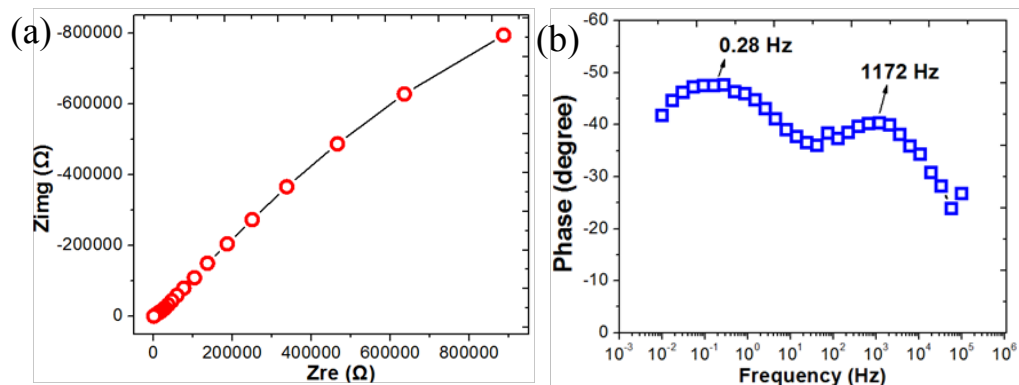


Figure 5.9 (a) EIS spectra and (b) the Bode Phase plot of the LR-GO film.

movement in the GO based solid electrolyte are discussed in the Chapter 6.

Two peaks are observed in the Bode phase plot (Figure 5.9b) based on the EIS test, with one at ~ 1172 Hz and the other at ~ 0.28 Hz. The existence of two peaks instead of one suggests the existence of two groups of ions with different mobility [30, 31] and is consistent with the DPD model. Same as the SWNT-TEABF₄ ECs in Chapter 4, the peak at the higher frequency side is assigned to the tight-bonded ions; and the other peak is assigned to the loose-bonded ions [30, 31].

5.5 Conclusions

Flexible capacitors with a thickness of tens of micrometers can be feasibly fabricated on the GO films using controllable laser reduction techniques. The prepared LR-GO films without introducing any electrolytes exhibit a small specific capacitance of $\sim 9.7 \text{ uF}\cdot\text{cm}^{-2}$ due to the poor ionic conductivity. The small specific capacitance and the subsequent small driving force of the ionic concentration gradient lead the self-discharge of LR-GO EC to proceed under the potential field driving. It is further

confirmed that the dominant self-discharge model is determined by the competition of the two driving forces, the potential field ΔE and the ionic concentration gradient $\partial c/\partial x$; and the ECs with a high initial voltage ($\Delta E = V$) and a low specific capacitance C (small $\partial c/\partial x$ by $Q = C \times V$) tends to be dominated by the potential driving model. Moreover, the DPD model dominates the self-discharge of the LR-GO EC because of the existence of a large amount of functional groups.

The successful repeatability of the scenario with LR-GO ECs not only extends its applicability to a wider range of capacitor types; but also offers valuable information on the ionic diffusion in the GO based solid-state electrolyte, which would be vital for future study on the GO based ECs.

ACKNOWLEDGMENTS

The author wishes to thank the following individuals for their contributions to this chapter. Taoli Gu performed the Raman measurements on the GO and LR-GO films. Robert Forest performed the XPS measurements on the GO and LR-GO films.

REFERENCES

- [1] Zhang, Q., et al., *The governing self-discharge processes in activated carbon fabric-based supercapacitors with different organic electrolytes*. Energy & Environmental Science, 2011. **4**(6): p. 2152-2159.
- [2] Zhang, Q., J. Rong, and B. Wei, *A divided potential driving self-discharge process for single-walled carbon nanotube based supercapacitors*. RSC Advances, 2011. **1**(6): p. 989-994.
- [3] Gao, W., et al., *Direct laser writing of micro-supercapacitors on hydrated graphite oxide films*. Nature Nanotechnology, 2011. **6**(8): p. 496-500.
- [4] Zhang, Q., et al., *Anomalous Capacitive Behaviors of Graphene Oxide Based Solid State Supercapacitors*. Nano letters, 2014. **14**(4): p. 1938-1943.
- [5] Choucair, M., P. Thordarson, and J.A. Stride, *Gram-scale production of graphene based on solvothermal synthesis and sonication*. Nature Nanotechnology, 2008. **4**(1): p. 30-33.
- [6] Hernandez, Y., et al., *High-yield production of graphene by liquid-phase exfoliation of graphite*. Nature Nanotechnology, 2008. **3**(9): p. 563-568.
- [7] Cho, J., et al., *Atomic-scale investigation of graphene grown on cu foil and the effects of thermal annealing*. ACS Nano, 2011. **5**(5): p. 3607-3613.
- [8] Kim, K.S., et al., *Large-scale pattern growth of graphene films for stretchable transparent electrodes*. Nature, 2009. **457**(7230): p. 706-710.
- [9] Li, X., et al., *Large-area graphene single crystals grown by low-pressure chemical vapor deposition of methane on copper*. Journal of the American Chemical Society, 2011. **133**(9): p. 2816-2819.
- [10] Li, X., et al., *Large-area synthesis of high-quality and uniform graphene films on copper foils*. Science, 2009. **324**(5932): p. 1312-1314.
- [11] Hontoria-Lucas, C., et al., *Study of oxygen-containing groups in a series of graphite oxides: physical and chemical characterization*. Carbon, 1995. **33**(11): p. 1585-1592.

- [12] Lv, W., et al., *Low-temperature exfoliated graphenes: vacuum-promoted exfoliation and electrochemical energy storage*. ACS Nano, 2009. **3**(11): p. 3730-3736.
- [13] Huang, H.C., et al., *Photocatalytically reduced graphite oxide electrode for electrochemical capacitors*. The Journal of Physical Chemistry C, 2011. **115**(42): p. 20689-20695.
- [14] El-Kady, M.F., et al., *Laser scribing of high-performance and flexible graphene-based electrochemical capacitors*. Science, 2012. **335**(6074): p. 1326-1330.
- [15] Wu, Q., et al., *Supercapacitors based on flexible graphene/polyaniline nanofiber composite films*. ACS Nano, 2010. **4**(4): p. 1963-1970.
- [16] Yu, D. and L. Dai, *Self-assembled graphene/carbon nanotube hybrid films for supercapacitors*. The Journal of Physical Chemistry Letters, 2009. **1**(2): p. 467-470.
- [17] Zhang, L.L., et al., *Highly conductive and porous activated reduced graphene oxide films for high-power supercapacitors*. Nano Letters, 2012. **12**(4): p. 1806-1812.
- [18] Moon, I.K., et al., *Reduced graphene oxide by chemical graphitization*. Nature Communications, 2010. **1**: p. 73.
- [19] Tung, V.C., et al., *High-throughput solution processing of large-scale graphene*. Nature Nanotechnology, 2008. **4**(1): p. 25-29.
- [20] Kundu, S., et al., *Thermal stability and reducibility of oxygen-containing functional groups on multiwalled carbon nanotube surfaces: a quantitative high-resolution XPS and TPD/TPR study*. The Journal of Physical Chemistry C, 2008. **112**(43): p. 16869-16878.
- [21] Okpalugo, T., et al., *High resolution XPS characterization of chemical functionalised MWCNTs and SWCNTs*. Carbon, 2005. **43**(1): p. 153-161.
- [22] Martinez, M., et al., *Sensitivity of single wall carbon nanotubes to oxidative processing: structural modification, intercalation and functionalisation*. Carbon, 2003. **41**(12): p. 2247-2256.
- [23] Pulido, A., et al., *Reconstruction of the carbon sp² network in graphene oxide by low-temperature reaction with CO*. Journal of Materials Chemistry, 2012. **22**(1): p. 51-56.
- [24] Zhu, H. and B. Wei, *Direct fabrication of single-walled carbon nanotube macrofilms on flexible substrates*. Chemical Communications, 2007. **29**: p. 3042-3044.

- [25] Pech, D., et al., *Ultra-high-power micrometre-sized supercapacitors based on onion-like carbon*. Nature Nanotechnology, 2010. **5**(9): p. 651-654.
- [26] El-Kady, M.F. and R.B. Kaner, *Scalable fabrication of high-power graphene micro-supercapacitors for flexible and on-chip energy storage*. Nature Communications, 2013. **4**: p. 1475.
- [27] Cai, W., et al., *Synthesis and solid-state NMR structural characterization of ¹³C-labeled graphite oxide*. Science, 2008. **321**(5897): p. 1815-1817.
- [28] Lerf, A., et al., *Hydration behavior and dynamics of water molecules in graphite oxide*. Journal of Physics and Chemistry of Solids, 2006. **67**(5): p. 1106-1110.
- [29] Buchsteiner, A., A. Lerf, and J.r. Pieper, *Water dynamics in graphite oxide investigated with neutron scattering*. The Journal of Physical Chemistry B, 2006. **110**(45): p. 22328-22338.
- [30] Li, X., J. Rong, and B. Wei, *Electrochemical behavior of single-walled carbon nanotube supercapacitors under compressive stress*. ACS Nano, 2010. **4**(10): p. 6039-6049.
- [31] Brevnov, D.A. and T.S. Olson, *Double-layer capacitors composed of interconnected silver particles and with a high-frequency response*. Electrochimica Acta, 2006. **51**(7): p. 1172-1177.

Chapter 6

ANOMALOUS CAPACITIVE BEHAVIORS OF ALL SOLID-STATE GRAPHENE BASED ELECTROCHEMICAL CAPACITORS

6.1 Introduction

ECs are considered as a major component in electrochemical energy storage nowadays besides the rechargeable batteries, and they are widely used in areas requiring a high power capability and reliability[1, 2]. There is another type of electric capacitors, DCs, where no ionic diffusion exists and the energy is stored through the dielectric polarization under an external potential field.

An interesting contradiction between appreciable energy density and unrecognizable ionic diffusion is observed in the solid-state capacitors of sandwiched structures made from the GO films, which challenges the fundamental charge storage mechanisms proposed for both ECs and DCs. A new capacitive model is proposed, which combines the two distinct charge storage mechanisms of DCs and ECs, to explain the contradiction of high energy capacity yet undetectable ionic diffusion, seen in the GO based electric capacitors.

6.2 ECs and DCs

Schematics of the typical structures of EC and DC are given in Figure 6.1. As shown in Figure 6.1a, the energy storage in ECs is accomplished through the transportation and accumulation of electrolytic ions to the oppositely charged electrode surfaces, constructing the double-layer structures.

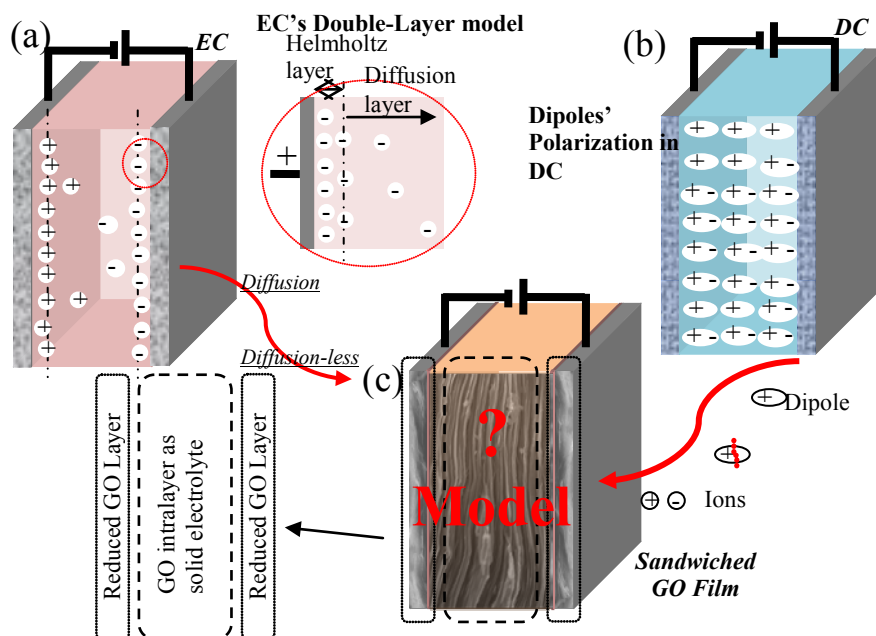


Figure 6.1 Schematics of charge storage mechanisms. (a) The EC, which stores energy through ionic diffusion under electrostatic attraction to form one or two atomic layers of compact electrolytic ions followed by a relatively uncondensed diffusion layer. (b) The DC, where dipoles in dielectric polarize under external potential field. (c) The GO-capacitor with the sandwiched structure of rGO/GO/rGO that behaves abnormally, where ions exist in the system yet without detectable ionic diffusion.

DCs are usually built with two opposing metal plates as current collectors, separated by a dielectric medium (such as a ceramic with a high dielectric constant)[3]. In DCs (Figure 6.1b), energy is stored through potential field-induced polarization of the dielectric medium, where the dipoles cannot be physically moveable.

There are no chemical reactions during the cycles of charging/discharging for both ECs and DCs, and the fundamental difference between ECs and DCs lies in two aspects: one is the existence of the diffusible electrolytic ions and the other is the

specific surface area of the electrode materials. As a result of the diffusible ions and the tremendous electrode/electrolyte interfaces in ECs, ECs normally hold an energy density of tens or even hundreds of farads per gram or per cm^2 [4-6], while DCs can only contain an energy density of tens of microfarads per cm^2 [3, 7].

According to the Stern-Grahame model, the double layers of ECs consist of the compact Helmholtz layers and a diffusion layer. The diffusion layer results from the thermal fluctuation of the electrolytic ions. Cases have never been observed before on any EC where the energy is stored with ionic diffusion yet without diffusion layers presenting. However, an interesting phenomenon has been observed on the GO based solid-state capacitors (Figure 6.1c). An appreciable energy density was obtained while ionic diffusion was undetectable, despite of the ultra-wide frequency range applied for testing. Fundamental understanding on the possible new charge mechanisms on electrical capacitors is needed to explain the contradiction of high storage capacity yet dismissible ionic diffusion, seen in the GO based capacitors.

6.3 Experimental Section

6.3.1 Sample preparation

GO was prepared by the modified Hummer's method: natural graphite flakes (10 mesh, Alfa Aesar) served as the carbon sources. After 5 days of oxidization and exfoliation with KMnO_4 in a concentrated sulfuric acid, brownish-colored colloidal dispersion of GO was obtained. Extensive washing with centrifuge and dialysis were followed to remove the excess acids and salts.

The preparation of the GO film is given in detail in Figure 6.2. Lightscribing digital video disc (DVD) was first layered with an aluminum foil. The deposition of

the purified GO aqueous solution ($\sim 10 \text{ mg}\cdot\text{mL}^{-1}$, $\text{pH}\sim 2.83$) was carried out by a simple drop-casting on the aluminum foil. After air drying, a free-standing, flexible GO thin film can be easily peeled off the foil. The thickness of the GO films ranges within tens of micrometers by adjusting the dosage of the GO solution.

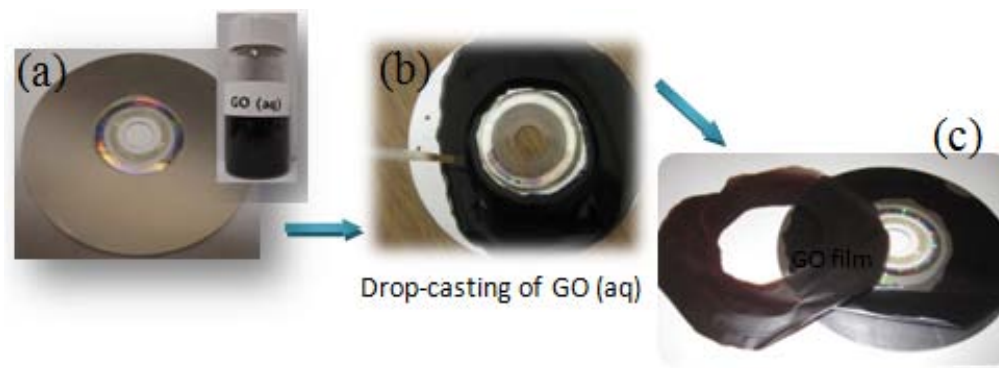


Figure 6.2 Schematic flow of sandwiched GO film fabrication: (a) the lightscribing DVD disk with aluminum foil attached on and the GO (aq). (b) Drop-casting GO (aq) onto the aluminum foil; (c) Air drying of the GO films.

6.3.2 Lightscribing reduction

Lightscribing CD/DVD optical drive was applied here as an inexpensive and feasible laser source (output power $P=38 \text{ mW}$, wavelength $\lambda =780 \text{ nm}$). The lightscribing technique of DVD labeling can provide a mild and controllable method for GO reduction. The process for the reduction is schematically illustrated in Figure 6.3, similar to the lightscribing reduction method reported by El-Kady, *et al*[8]. After finishing reduction on one side, the GO film was detached from the aluminum foil and flipped over for reduction on the other side. The reduced films with rGO/GO/rGO sandwiched structure are called GO capacitor films or capacitor films.

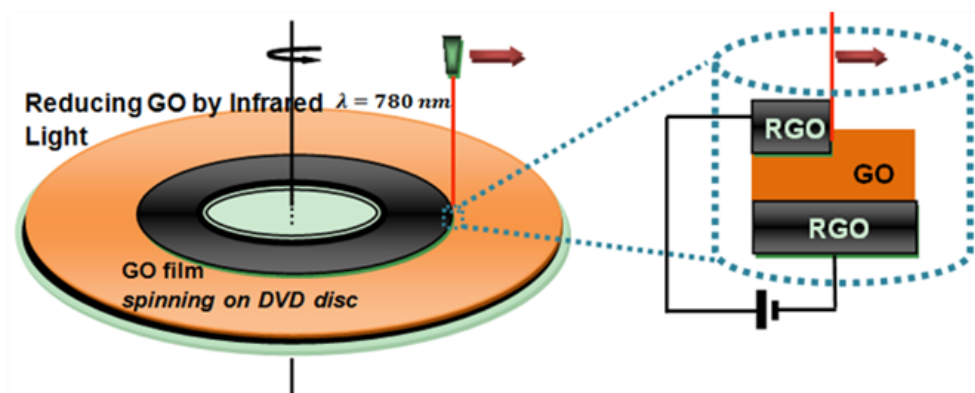


Figure 6.3 Schematic of the lightscribing process.

6.3.3 Characterizations of the GO films and the sandwiched GO films

Structural characterizations have been conducted on the GO films and the sandwiched GO films, including atomic force microscopy (AFM, SPM-Dimension3100), transmission electron microscopy (TEM, JEM 2010F), SEM (JSM-7400F field emission SEM) and X-ray diffraction (XRD, Philips X'Pert X-ray diffractometer).

XRD diffraction was measured from 0 to $80^\circ (2\theta)$ in $0.01^\circ (2\theta)$ steps at 0.5 sec per step, using $\text{Cu } K\alpha$ radiation (1.542 \AA).

Electrical conductivity test (four-point probe I-V electrical measurements) has been applied to measure the electrical conductivity of the film before and after reduction.

Chemical identifications have been applied on the GO films and the sandwiched GO films, including TGA (METTLER TGA/DSC), Raman spectroscopy (Bruker Senterra AFM/Raman Microscope), and nuclear magnetic resonance (NMR).

TGA experiments were designed from room temperature to 1000 °C at a heating rate of 2 °C·min⁻¹, under nitrogen protection (60 mL·min⁻¹). In order to exclude the weight change from moisture desorption below 100 °C[9], the TGA results were analyzed from 100 °C to 1000 °C.

Raman spectra were collected with a laser excitation wavelength of 532 nm.

NMR was utilized to provide more detailed information on the chemical composition of the GO film and the sandwiched GO film. ¹³C single-pulse (SP) magic-angle-spinning (MAS), ¹³C cross-polarization (CP) MAS and ¹H MAS solid state NMR spectra were recorded using a Bruker AVIII 500 solid state NMR spectrometer operating at 10 kHz, and a 4mm HX double resonance MAS probe with zirconia rotors, 4mm in diameter driven by compressed air. The GO film and the sandwiched GO film were pulverized into homogeneous powders for packing.

6.3.4 Electrochemical characterizations of the sandwiched GO films

CV, galvanostatic charge/discharge/self-discharge, and EIS were used to characterize the electrochemical performance of the sandwiched GO capacitor films.

EIS was done using a sinusoidal signal with a mean voltage of 0 V and a bias of 10 mV over a frequency range from 3 MHz to 10 mHz. CV curves were scanned at voltage ramp rates from 2 to 200 mV·s⁻¹, from 0 to 0.5 V. Both EIS and CV measurements were performed in open air at room temperature. The Nyquist plot of EIS was fitted with Z-View. The galvanostatic charging/discharging was done for 5000 cycles together with self-discharging to demonstrate the electrochemical capacitive behaviors, with a charge current density of 200 mA·g⁻¹.

6.3.5 Measurement of dielectric constant for the GO films

GO film, without reduction, is electrically insulating and unlike the sandwiched GO film which can work as an electrochemical capacitive device. Therefore, in order to measure its dielectric constant, cyclic voltammetry (CV) for capacitor characterization cannot be applied; instead, the standard method for semi-conductor dielectric characterization is used here. The dielectric constant is measured from the ratio of the capacitance of the GO film as dielectric relative to that of the vacuum as dielectric. Two kinds of samples were prepared: GO film and gold sputtered GO film (gold sputtering is used to enhance the electric conduction from the GO film to the current collector). For the measurement, the film was sandwiched between two current collectors and the capacitance was recorded for voltage from -1.5 V to 1.5 V with a step of 0.1 V. In the capacitance-voltage curves (C-V curves), the capacitance is stable within the voltage range as capacitance is intrinsic and unrelated to the voltage applied. The dielectric constant ϵ_r is calculated by

$$\epsilon_r = \frac{C \times d}{A \times \epsilon_0} \quad \text{-----} \quad 6.1$$

where C is the measured capacitance, d is the thickness of the GO film, A is the area of the GO film, and ϵ_0 is the vacuum permittivity.

6.3.6 Measurement on the humidity effects

CV scanning was run on the sandwiched GO capacitor film before it was put into a sealed glass desiccator, in which the relative humidity was adjusted up to ~80% by saturated KNO_3 (aq). After a month, no appreciable weight increase was observed and CV scanning was carried out immediately after taking the film out of the humid

environment. Then the film was put in the open air for another ten days and tested by the CV scanning again. All CV scans were run with the same scan rate of $100 \text{ mV}\cdot\text{s}^{-1}$.

6.3.7 Simulation on the water structures and charge distribution in the gap of two graphene sheets

Figure 6.4 shows a schematic of the molecular dynamic (MD) simulation system, which consists of water, H^+ and OH^- ions bounded between two graphene sheets. The lateral size of the graphene sheets is $38.34 \times 39.35 \text{ \AA}^2$, corresponding to 576 C atoms. The distance between the graphene sheets (d) was 8 \AA , as determined in the experiment. Two types of graphene were used in the simulation. One is GO containing $\sim 30\%$ oxygen species and the other is rGO with 5% oxygen species (both contain 50% O and 50% OH in the calculation). About $7\text{wt}\%$ water ($38 \text{ H}_2\text{O}$ molecules) and 9 H^+ and 3 OH^- ions were placed in a three-dimensional (3D) domain with dimensions of $38.34 \times 39.35 \times 8 \text{ \AA}^3$; periodic boundary conditions were imposed in the x , y and z directions.

Water-water inter- and intra-molecular interactions was modeled with a flexible simple-point-charged (SPC) potential, which was specifically re-parameterized to reproduce the main trends of the infrared spectrum of water at ambient conditions [10]. Water-carbon forces have been assumed to be of the Lennard-Jones type with the same parameterization in studies of water near graphite [11]. O-H bonds were constrained using the Shake algorithm. Graphene sheets were described by using the second-generation reactive empirical bond-order potential (REBO) [12]. The C-O bonds on GO were described by a force field potential, and the

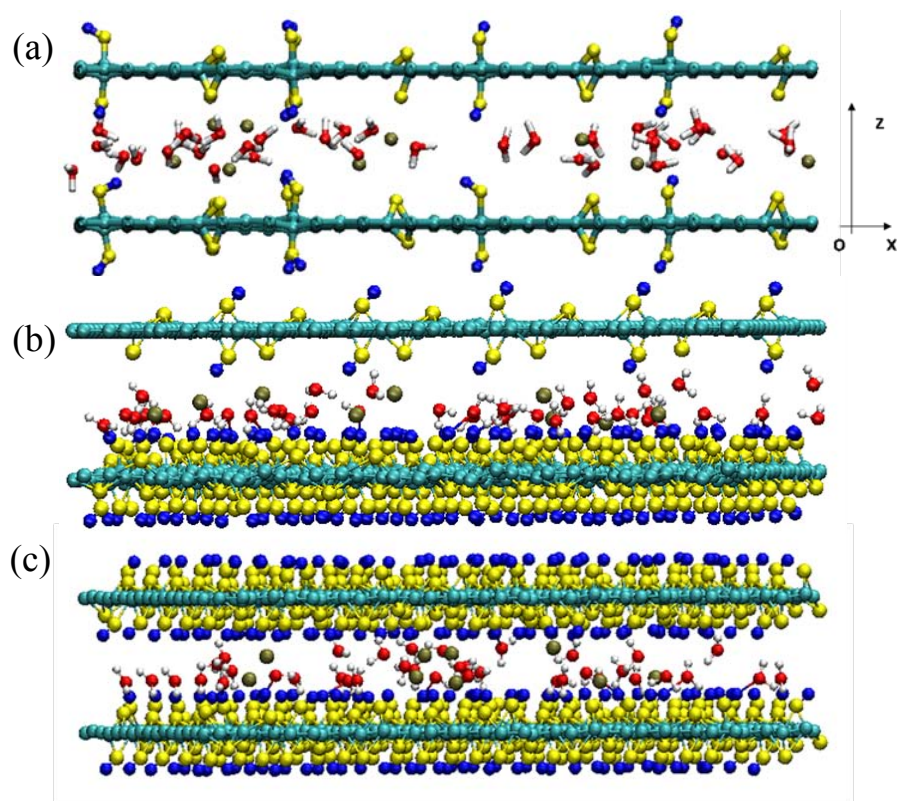


Figure 6.4 Molecular structure of water, H, and O confined along z-direction perpendicular to the graphene or GO sheets, in two rGO sheets (a), in one rGO and one GO sheets (b) and in two GO sheets (c).

charge distribution on graphene due to C-O or C-OH bonds were determined using the Vienna Ab initio Simulation Package (VASP) [13]. We used spherical cutoff radii of 10 Å for the vdW and Coulomb interactions, respectively. Electrostatic interactions beyond the cutoff radius of 10 Å were calculated using a particle-particle particle-mesh (PPPM) scheme in reciprocal space; the inter-slab interactions in the z direction were removed by inserting a large vacuum space between the graphene sheets. MD simulations were performed with the Large-scale Atomic/Molecular Massively Parallel Simulator (LAMMPS) program [14], and the velocity Verlet algorithm was

employed to integrate Newton's equation of motion with a time step of 0.5 fs. We ran MD at 300 K for 1 ns to equilibrate the system, and then applied an external field of $V=50 \text{ V}\cdot\text{mm}^{-1}$ (the same as in the experiment) to the system in the z-direction for 0.5 ns. All runs were in the NVT ensemble with the temperature controlled by a Nose-Hoover thermostat with a 100 fs damping parameter. The charge distribution and density were the average of 50 continuous samples obtained from the simulation.

6.4 Results and Discussion

6.4.1 Microstructure and chemical identification analysis

6.4.1.1 Microstructure: AFM, TEM and SEM

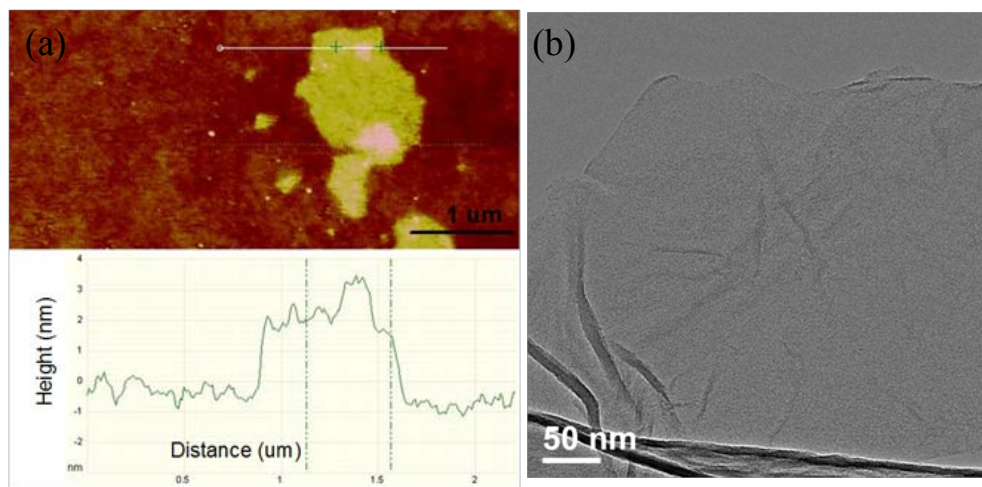


Figure 6.5 (a) AFM image of the GO samples on silicon wafers; (b) TEM images of the reduced GO with slightly wrinkles.

From AFM observations (Figure 6.5a), the measured thickness of the GO samples ranges within (1-5) nm, mostly 2 nm or 3 nm in thickness, indicating that the synthesized GO dispersion mostly contains few-layer GO [9]. The TEM image (Figure 6.5b) shows that the rGO sample also presents a layering structure.

Significant changes on the surface morphology are observed from SEM before and after the laser reduction. Comparing the top-view of the film before and after reduction (Figure 6.6a and b), the reduced surface exhibits a cracked morphology instead of the plainness of the unreduced sample surface as a result of heat initiated volatilization and volume-expansion reduction. From the cross-sectional views, the pristine GO film features well-stacked layering structure (Figure 6.6c). After

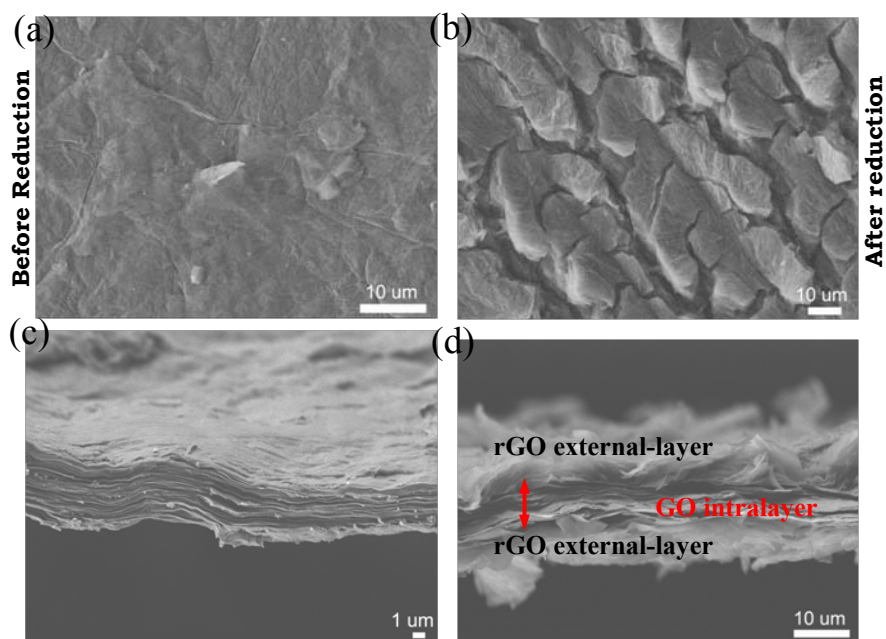


Figure 6.6 SEM images of the top-views of (a) GO film and (b) the sandwiched GO capacitor film. Cross-sectional view of (c) the GO film and (d) the sandwiched GO capacitor film. The thickness of the GO intralayer (indicated by the red arrow) is $\sim 9 \mu\text{m}$.

reduction (Figure 6.6d), the GO expands and becomes much more porous on the surfaces. The rGO surface evolves into a fluffy morphology comprised of reduced GO layers. The two-sided reduction grants the film a sandwiched structure of rGO/GO/rGO. Translucent rGO layers are commonly observed, further indicating the volume expansion during the laser reduction as well as the fine exfoliation of the rGO layers.

6.4.1.2 Dielectric constant of the GO film

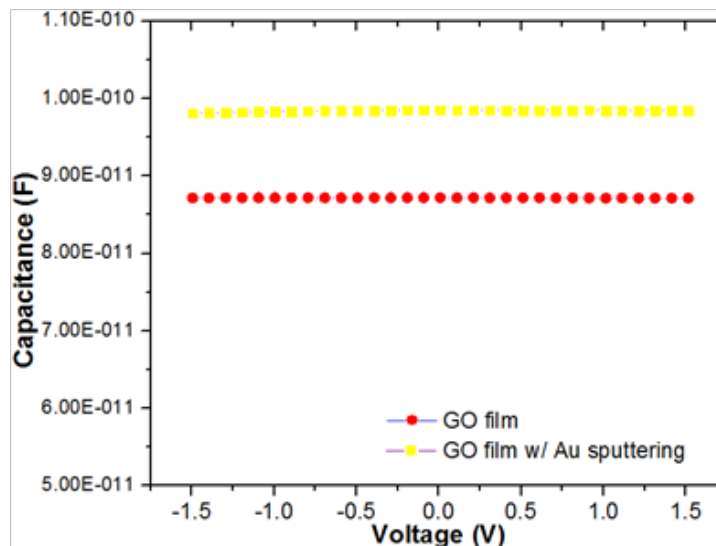


Figure 6.7 C-V curve measured on the GO film and the gold-sputtering GO film.

As shown in the C-V curves given in Figure 6.7, the capacitance is stable within the voltage range from -1.5 to 1.5 V. The capacitance is intrinsic and unrelated to the voltage applied. The average capacitance of GO film ($\sim 17.5 \mu\text{m}$ thick) is 8.72×10^{-11} F, and the average capacitance for gold sputtered GO film ($\sim 11.5 \mu\text{m}$ thick

before sputtering) is 9.84×10^{-11} F. The electrode area A is the same for both samples, $\sim 1.5 \text{ cm}^2$. According to Eqn. 6.1, the dielectric constants can be calculated as following:

$$\text{for the GO film, } \epsilon_r = \frac{C \times d}{A \times \epsilon_0} = \frac{8.72 \times 10^{-11} \text{ F} \times 17.5 \times 10^{-6} \text{ m}}{1.5 \times 10^{-4} \text{ m}^2 \times 8.854 \times 10^{-12} \text{ F} \cdot \text{m}^{-1}} = 1.15;$$

$$\text{for the gold sputtered GO film, } \epsilon_r = \frac{C \times d}{A \times \epsilon_0} = \frac{9.84 \times 10^{-11} \text{ F} \times 11.5 \times 10^{-6} \text{ m}}{1.5 \times 10^{-4} \text{ m}^2 \times 8.854 \times 10^{-12} \text{ F} \cdot \text{m}^{-1}} = 0.85.$$

The measured dielectric constants here are within the same order as reported values on graphene and GO[15, 16].

6.4.1.3 XRD, TGA and Raman

XRD results are given in Figure 6.8a. Both the GO film and the sandwiched GO film exhibit a sharp peak at $\sim 11.0^\circ(2\theta)$, corresponding to a d -spacing of $\sim 8.04 \text{ \AA}$. The enlarged interlayer distance results from the intercalation of molecules (water or functional groups) between graphitic layers during the Hummer's graphite oxidation. The sharp peak still exists for the sandwiched GO films after reduction as there is a significant portion of unreduced GO intralayer. The GO intralayer gives rise to the peak at $\sim 11.0^\circ(2\theta)$, when X-rays penetrate through the thin layer of rGO on the film surface. Moreover, a weak and broad peak near $\sim 25^\circ(2\theta)$, appears and is ascribed to the rGO because GO intend to restack after reduction when the intercalated ions and molecules are removed [5, 17].

Figure 6.8b presents the XEDS results as collected on multiple areas on the reduced GO external layers and the GO intralayers. After reduction, the oxygen content decreases from $\sim 38\%$ to $\sim 12\%$ in atomic ratio (the oxygen content in the GO intralayers is approximate to that in the GO film).

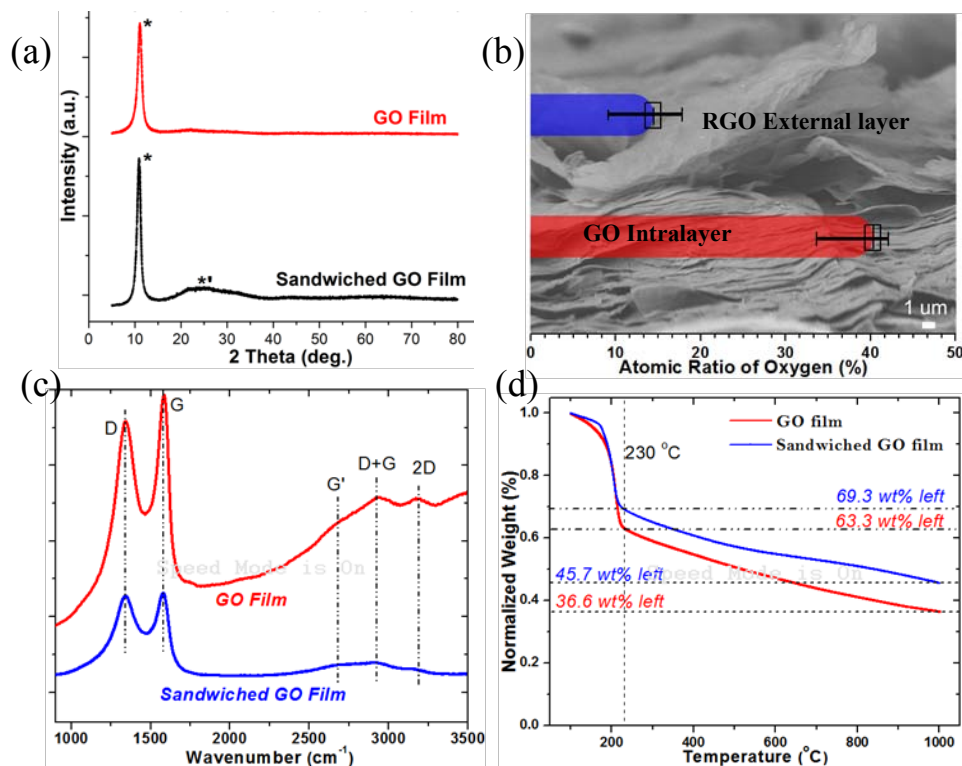


Figure 6.8 (a) XRD characterization of the GO film and GO-capacitor film. (b) XEDS analysis of the sandwiched GO film; (c) Raman spectra for the GO film and the sandwiched GO film, featuring five peaks. (d) TGA analysis from 100 °C to 1000 °C on the GO film and the sandwiched GO film. The TGA results prove a decrease in functional groups and water molecules in the sandwiched GO film.

Results from the Raman spectroscopy and TGA further demonstrate the reduction at the GO surface.

As shown in the Raman spectra in Figure 6.8c, there are two major bands: the D (defects) band at $\sim 1340\text{ cm}^{-1}$ as induced by the structural disorder and the G (graphitization) band at $\sim 1580\text{ cm}^{-1}$ as induced by the aromaticity of the graphene lattice [17, 18]. After reduction, the intensity ratio of D and G bands: D/G increases

from 0.91 to 0.97. According to Moon, *et al.*[17], the increase in the defect sites is because of the restoration of a highly defected lattice after removal of oxygen-containing functional groups.

TGA with nitrogen as the protective gas was performed to further confirm the decrease in oxygen-containing functional groups. As shown in Figure 6.8d, major weight loss is observed at around 220 °C due to decomposition of functional groups [9, 17, 19]. The GO film has a weight loss of 36.7 wt%, while the capacitor film has a weight loss of 30.7 wt%. Only 6 wt% change is observed because the reduction has only occurred on the film surfaces.

Overall, it has been confirmed that the GO film has been reduced into a sandwiched rGO/GO/rGO capacitor film, where the reduction is localized on the film surfaces, not through the entire film thickness as in the LR-GO film discussed in Chapter 5.

6.4.2 Electrochemical performances

6.4.2.1 Galvanostatic charge/discharge

The galvanostatic charge/discharge on the sandwiched GO capacitor film is given in Figure 6.9a, and demonstrates the electrochemical capacitive behavior, where energy can be stored and released through cycles of charging/discharging. Self-discharge with a large IR drop is also observed (Figure 6.9b) when the capacitor film is disconnected from external circuit, and the large IR drop indicates the poor electrical conductivity of the GO capacitor film, mainly due to the non-electrically conducting GO intralayer.

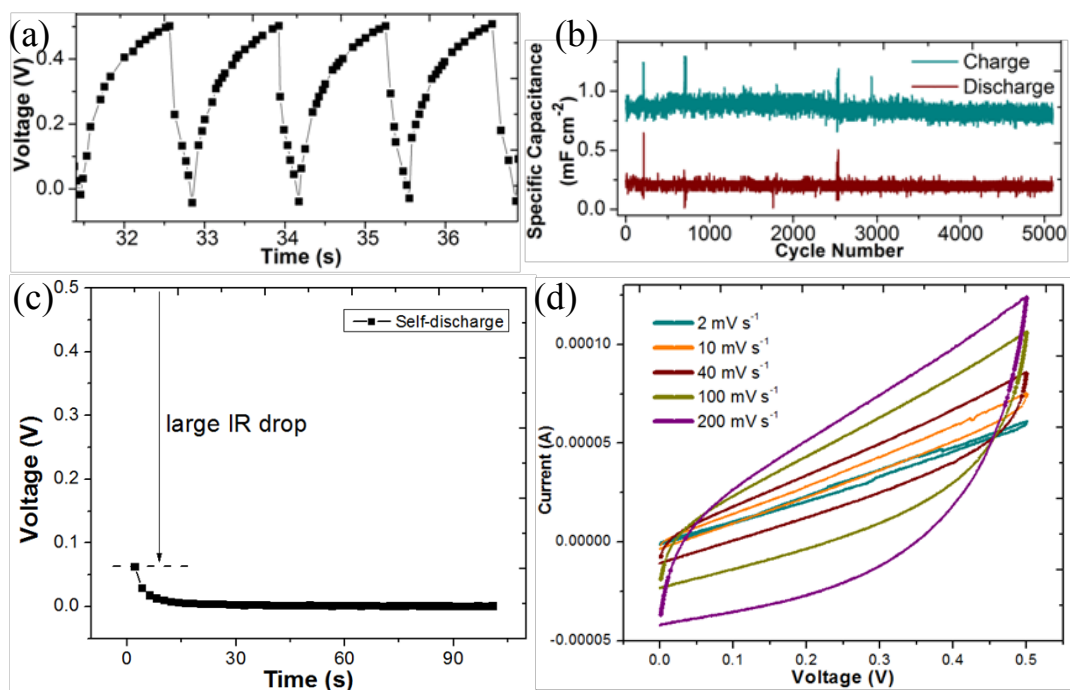


Figure 6.9 (a) The galvanostatic charge/discharge cycles (200 mA g^{-1}) of the GO-capacitor; (b) The corresponding specific capacitance for charging/discharging. (c) Self-discharge curve measured after two and a half charge/disharge cycles (from 0 V to 0.5 V) with a charge current density of $200 \text{ mA}\cdot\text{g}^{-1}$; (d) CV cycles from 0 to 0.5 V with different scan rates.

A fairly high specific capacitance up to $\sim 0.9 \text{ mF}\cdot\text{cm}^{-2}$ has been obtained (Figure 6.9b), consistent with the values calculated from the CV curves in Figure 6.9d. The specific capacitances corresponding to different scan rates are summarized in Table 6.1. The capacitance value falls between the reported values from 0.4 to $2 \text{ mF}\cdot\text{cm}^{-2}$ of the microcapacitors fabricated on carbon-based films[20-22]. It is impossible that the capacitance of such high value originates from the dielectric polarization of the GO sandwiched film, because the dielectric constant ϵ_r needs to be $\sim 10^7$ to achieve the as-measured capacitance of $\sim 0.9 \text{ mF}\cdot\text{cm}^{-2}$, while the ϵ_r measured from the

film is within the order of unity (Section 6.4.1.2). Therefore, the all solid-state GO capacitors cannot be categorized as DCs.

Table 6.1 Specific capacitance for the sandwiched GO Film, calculated from CV curves.

| scan rate ($mV \cdot s^{-1}$) | 2 | 10 | 40 | 100 | 200 |
|---------------------------------|------|------|------|------|------|
| C_A ($mF \cdot cm^{-2}$) | 0.86 | 0.45 | 0.39 | 0.33 | 0.26 |
| C_W ($mF \cdot mg^{-2}$) | 0.67 | 0.35 | 0.31 | 0.25 | 0.2 |

6.4.2.2 Electrochemical impedance spectroscopy

The EIS spectrum of the sandwiched GO capacitor film collected on extended range from 3 MHz to 10 mHz is shown in Figure 6.10. An equivalent circuit for the EIS fitting is also given and is composed of three parts in series due to the asymmetric shape of the second semicircle on the lower frequency side. The blue semicircle corresponds to the blue circled part in the circuit, the green semicircle corresponds to the green circled part and the orange semicircle corresponds to the orange circled part. Each semicircle comes from the response of the corresponding circuit part to the tested frequencies.

The double-layered charge mechanism of ECs has been applied to explain the origin of the charge storage in those either graphene based microcapacitors with a specific capacitance of $\sim 0.51 \text{ mF} \cdot \text{cm}^{-2}$ [20] or other carbon-based microcapacitors [21-24], where their EIS spectra consist of a semicircle at the high frequency region followed with a quasi-straight line at the low frequency region (frequency range from 500 kHz to 1 mHz) [5, 6, 24].

Unlike the previous reports on the carbon-based microcapacitors, the EIS spectrum as collected on extended frequency range gives two consecutive semicircles; no Warburg line has been detected despite the extended frequency range. The absence of the diffusion line has never been observed in ECs before, suggesting the abnormal

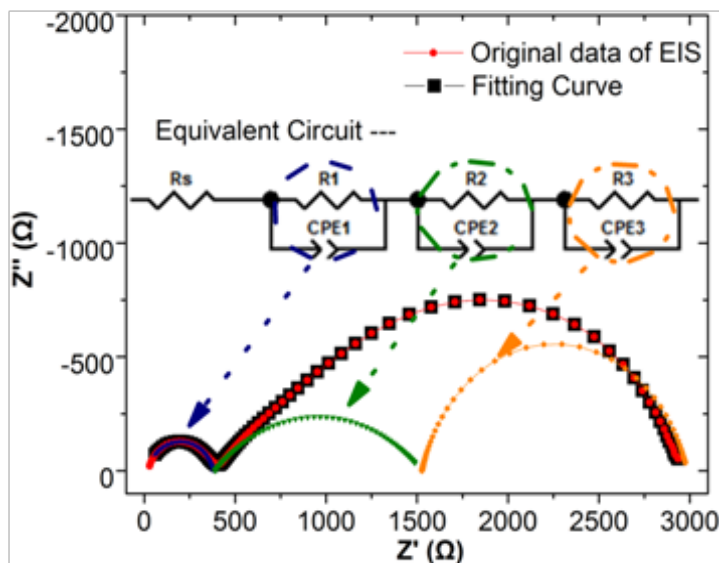


Figure 6.10 Nyquist plot of the GO capacitor film from 3 MHz to 10 mHz, giving two semicircles (fitted with the equivalent circuit above) without diffusion. The diffusion is typical for ECs and is represented by the Warburg line at a low frequency.

Table 6.2. Fitting Parameters of the Equivalent Circuit for EIS data.

| R_s / Ω | R_1 / Ω | CPE-1 | | R_2 / Ω | CPE-2 | | R_3 / Ω | CPE-3 | |
|---------------------|---------------------|------------|--------|---------------------|------------|--------|---------------------|------------|---------|
| 11.19 | 377 | CPE-1-T /F | 7.3E-8 | 1138 | CPE-2-T /F | 5.3E-4 | 1459 | CPE-3-T /F | 1.16E-3 |
| | | CPE-1-P | 0.7574 | | CPE-2-P | 0.5025 | | CPE-3-P | 0.8302 |

capacitive behaviors of the sandwiched GO film. Therefore, these all solid-state GO capacitors cannot be categorized as ECs.

In order to further investigate the energy storage mechanism of the GO capacitor films, NMR and MD simulations with the first-principle input have been conducted.

6.4.3 Solid state NMR spectroscopy

NMR results confirm the existence of functional groups and waters in the GO capacitor films.

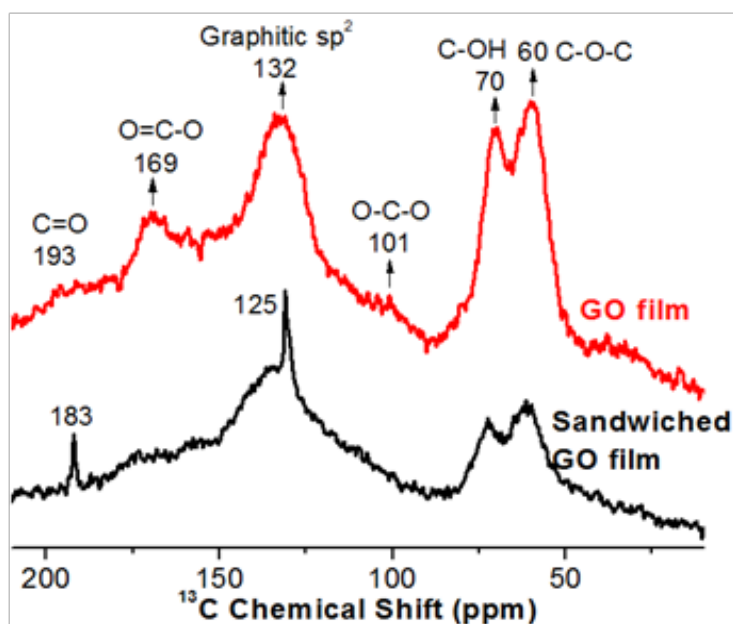


Figure 6.11 Solid-state ^{13}C single pulse (SP) MAS NMR spectra of GO film sample and the capacitor film sample at 10 kHz, confirms the existence of various functional groups.

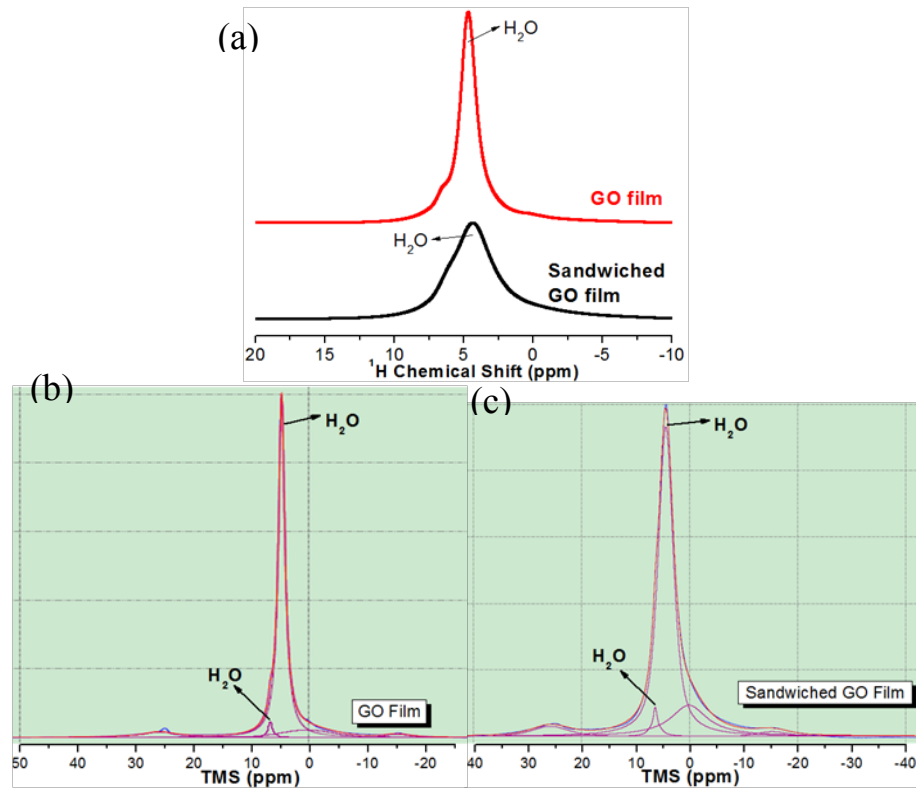


Figure 6.12 Solid-state ¹H NMR spectra of GO film sample and the sandwiched film sample at 10 kHz, confirms the existence of waters and various functional groups.

In the ¹³C SPMAS NMR spectra (Figure 6.11), both the GO film and the sandwiched GO capacitor film show distinguishable peaks[25], indicating the existence of various functional groups as denoted in the Figure 6.11.

Two sharp peaks are observed for the sandwiched GO film: one is around 125 ppm and the other is around 183 ppm. Due to the deoxygenation and the restoration of defective lattice structure, rGO is expected to possess a more ordered structure in the perpendicular-to-plane direction due to the restacking of those oxygen-removed aromatic planes, and in turn forms graphite-like micro-crystallites. Functional groups

sited at the well-defined structures of crystallites can give strong signals such as the two sharp peaks around 125 ppm and 183 ppm [26, 27].

As shown in Figure 6.12a, the solid state ^1H MAS NMR spectra exhibit similar resonance patterns for the GO film and the sandwiched GO film. Peak fitting results on the ^1H MAS NMR spectra are given in Figure 6.12b and c. The peak at ~ 4.6 ppm and the peak at ~ 6.6 ppm are assigned to water molecules [28, 29]. The latter is assigned to relatively confined water based on the assumption that the less-confined water or mobile water is easier to lose and the fitting results that the intensity ratio $I_{4.6\text{ ppm}}/I_{6.6\text{ ppm}}$ decreases from 33.2 to 23.9 after reduction.

The functional groups and the water molecules come from the preparation of the GO samples[25] and are crucial for the considerable capacitance of the sandwiched GO capacitors[20, 30, 31]: functional groups provide ions (such as protons from hydrolysis of the functional groups) and water molecules serve as pipelines/carriers for ions migration either *via* their hydrogen-bonding networks or in the free H_3O^+ form; the above two are the prerequisites for forming a charge separation when an external potential field is applied.

The restriction of the capacitance due to the limited water content is also indicated by the moisture effects on the CV curves as shown in Figure 6.13. The area enclosed within the CV curve corresponds to the capacitance of the tested sandwiched GO capacitor film. By comparing the black curve and the orange curve, a substantial increase in the capacitance is observed after the 30 days' humidity treatment; and then the CV curve shrinks a little after 10 days in the open air. Therefore, water content is of significance to the electrochemical performance of the sandwiched GO capacitor film. Limited amount of mobile water in the solid-state GO film restricts the ionic

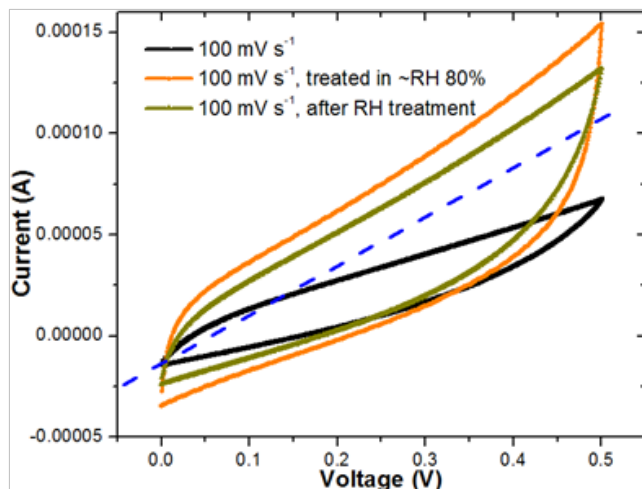


Figure 6.13 CV scanning of the sandwiched GO film before the humidity treatment, right after the 30 days' humidity treatment and ten days in the open air after the humidity treatment.

mobility and the capacitance, while increasing the water content can greatly enhance the capacitance.

To summarize, the sandwiched GO capacitor is an all solid-state film with layering structure; the layer-to-layer distance is within one nanometer, and functional groups together with water molecules are accommodated within these interlayer spacing. Without introducing any foreign electrolytes, the film capacitors exhibit considerable capacitances but no discernible ionic diffusion, which are different from the known ECs and DCs.

6.4.4 Modeling on the charge structure

In order to understand the abnormal capacitive behavior, the closely-packed structure within the GO film was simulated by employing the classical MD method

with the first-principle input. The charge distribution on GO or rGO was calculated using the density function theory (DFT) method and input into the MD models.

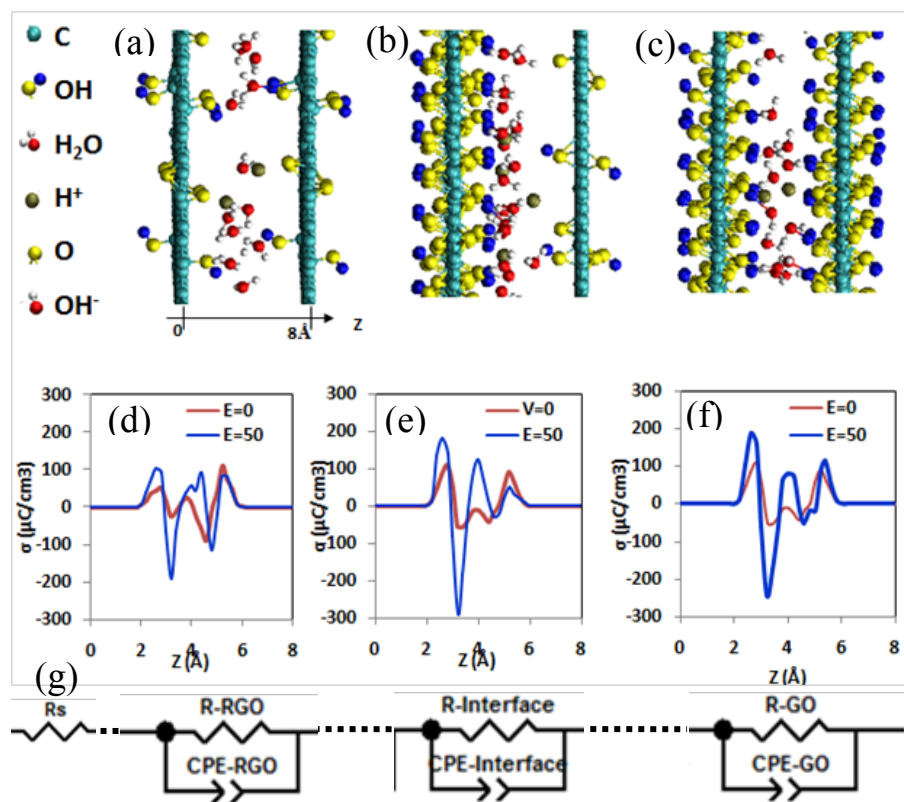


Figure 6.14 Molecular structures and charge distributions. a-c, Molecular structures of water confined within (a) two rGO sheets, (b) one GO and one rGO sheets, and (c) two GO sheets. d-f, Charge distributions (excluding the charge on graphene) along z-direction perpendicular to graphene plane under an external electrical field (E , unit Vnm^{-1}), showing in (d), (e) and (f) correspond to the rGO, rGO/GO, and GO systems, respectively. g, Three parts of the EIS equivalent circuit assigned to the rGO surface, the GO/rGO interface, and the GO intralayer according to the calculated parameters (Table. 6.4.2.2.1), the electrochemical performance is the collective result of all three parts.

Figure 6.14 shows molecular structures and charge density distribution between two rGO sheets, a GO and an rGO sheet, and two GO sheets with the same spacing of 0.8 nm (experimental results, Figure 6.8a), containing 7 wt% water and protons (in acidic state). For the rGO sheets, as shown in Figure 6.14a, the water molecules randomly distribute, but when an external electrical field (E) is applied to the system, the water molecules become aligned along z-direction with hydrogen atoms facing the rGO sheets. As a result, alternative positive and negative charge distribution occurs along z-direction (Figure 6.14d). Similar molecular structures and charge distribution were also found within the GO sheets (Figure 6.14c and f), in which the water molecules are much more ordered than those in the rGO and the rGO/GO systems (Figure 6.14b). Overall, the water molecules are much more ordered and accumulated near the left layer than near the right layer.

The above phenomena are closely related to the charge distribution on GO (rGO) due to the adsorbed functional groups (*e.g.*, C-O, C-OH) and the polarization of water molecules which are considered as dipoles. The DFT and MD calculations show that the adsorption of -O and -OH groups leads to polarization of GOs with positive charge on graphene and separated negative charges on O atoms. Thus, GO surfaces are negatively charged. When an external electrical field is applied, water molecules will rotate and align with hydrogen atoms facing negative electrode (left graphene layer) and oxygen facing positive electrode (right GO or rGO layer). Since graphene surfaces have negative charges, the GO layer (left layer in Figure 6.14a, b and c) will attract hydrogen atoms (with positive charges) while the GO layer (right layer in Figure 6.14a, b, and c) will repel the oxygen (with negative charges) in the water molecules. As a result, water molecules tend to accumulate and align near one (left) electrode.

The change in total positive charges stored within a GO gap was calculated after an external electrical field was applied. The calculation was done by integrating all the positive charges within GO/rGO gaps using the charge distributions shown in Figure 6.14d-f. Under the electrical field ($E=50 \text{ Vmm}^{-1}$, the same as the experimental value), the stored charge increases within the rGO, the rGO/GO, and the GO sheets are 281, 355, and 388 $\mu\text{C}\cdot\text{cm}^{-3}$, respectively. Compared with the rGO system, the charge separation is significantly enhanced within the GO sheets because of the existence of more O and OH species adsorbed on the graphene sheets. In the interfacial region of the rGO/GO, the charge distributions are the mixture of above two cases. The increase in stored charge stems from the synergetic effect of the electric field and the charged GOs, which makes the water much more ordered near a GO. For a GO with more functional groups, a stronger surface charge leads to the ordering of water near it even before the electrical field is applied, as shown in Figure 6.14e and f. When an external electrical field is applied, the water becomes much more ordered near the GO, significantly increasing electrical charge storage.

In all cases, the water molecules confined within the nano-gaps become more ordered, depending on the amount of O and OH species attached to the graphene sheets and the magnitude of the external electrical field. The formation of the ordered water structure within these nano-gaps does not need a long-range diffusion. Based on the above discussion, a new model, namely “Charge Close-Packed model” (CCP model), as shown in Figure 6.14, is proposed and explains the abnormal capacitive behavior of the sandwiched GO film.

6.4.5 Charge Close-Packed model

In the CCP model, extensive numbers of layers of alternatively packed positive and negative charges are periodically ordered, without the presence of the diffusion regions. Due to the confinement of the GO (rGO) layers together with the poor ionic mobility, the diffusion length of the ions has been restricted within the nanoscaled interlayer spacing, which are within the same scale as the double layered structures in ECs. This restriction leads to a less-than-0.8 nm diffusion length for the ions and eliminates the possibility of building up a diffusion layer. The absence of Warburg line in the EIS (Figure 6.10) also confirms this undetectable ionic diffusion. Moreover, the ordered, polarized/separated water molecules between the GO or rGO layers form a proton-conducting skeleton. Under charging, ions migrate with a very limited distance along the external potential field direction and accumulate onto the water skeleton, and the charge density peaks at those locations (Figure 6.14). This unique structure of alternatively packed positive and negative charge within the graphene nano-gaps strongly enhances the total energy storage.

It should be noted that the low Coulombic efficiency observed from the galvanostatic charge/discharge of the sandwiched GO film (Figure 6.9b) is different from the nearly symmetric behavior of ECs between charging/discharging. We speculate that this phenomenon may be attributed to the new energy storage model though a thorough understanding of the phenomenon is not available and worthy of further investigation.

Based on the CCP model depicted in Figure 6.14, the physical meanings of the three circuit parts in series (Figure 6.10) can be interpreted as corresponding to three different regions possessed by the sandwiched GO film: the rGO external layers, rGO/GO interfaces and GO intralayers, as shown in Figure 6.14g. Because of the

reduction, the three parts exhibit varied electrical conductivity and hold different amount of functional groups and water molecules (i.e., different charge densities, Figure 6.14d-f); Comparing the fitting parameters (Table 6.2) with the electrical conductivity/ionic mobility in each structural part, the GO intralayers with the poorest electrical conductivity and the highest charge density are assigned to the third circuit with the largest resistance and the highest capacitance.

6.5 Conclusions

The one-body, all solid-state capacitors are successfully fabricated on the GO films using lightscribing techniques, which grant the reduced film a delicate sandwiched structure rGO/GO/rGO within micro-scales.

The sandwiched GO film can be directly used as capacitors. Interesting contradiction has been found on the sandwiched GO film with a considerable energy density but without detectable ionic diffusion, which challenges the convention definitions of electric capacitors. In order to explain the contradiction, the CCP model is proposed based on the experimental results and theoretical modeling.

CCP model describes the nanoscaled ionic diffusion as localized by the layered structures and the poor ionic mobility within the sandwiched GO film, which eliminates the possibility of building up a diffusion layer. On the other hand, the periodically packed charge due to the layering structure of GO (rGO) layers contributes to a promising energy capacity.

The CCP model combines and challenges the conventional definitions on DCs and ECs, and is a step of significance for approaching to a more accurate definition on the electric capacitors. Moreover, the meticulous investigation provides useful

information of the structures and molecular dynamics of the sandwiched GO films, which would benefit further research in the related area.

ACKNOWLEDGMENTS

The author wishes to thank the following individuals for their contributions to this chapter. Kathryn Scrafford helped with the device fabrication. Mingtao Li and Zhenhai Xia conducted the modelling and analyzed the relevant data. Zeyuan Cao helped with the TEM and the conductivity measurements. This chapter was previously published in ref. [32] (<http://pubs.acs.org/doi/abs/10.1021/nl4047784>). Reprinted with permission, Copyright 2014 American Chemical Society.

REFERENCES

- [1] Zhang, L.L. and X. Zhao, *Carbon-based materials as supercapacitor electrodes*. Chemical Society Reviews, 2009. **38**(9): p. 2520-2531.
- [2] Miller, J.R. and P. Simon, *Electrochemical capacitors for energy management*. Science, 2008. **321**(5889): p. 651-652.
- [3] Conway, B., *Electrochemical supercapacitors: scientific fundamentals and technological applications (POD)*. 1999: Kluwer Academic/Plenum: New York.
- [4] Simon, P. and Y. Gogotsi, *Materials for electrochemical capacitors*. Nature Materials, 2008. **7**(11): p. 845-854.
- [5] Liu, C., et al., *Graphene-based supercapacitor with an ultrahigh energy density*. Nano Letters, 2010. **10**(12): p. 4863-4868.
- [6] Zhu, Y., et al., *Carbon-based supercapacitors produced by activation of graphene*. Science, 2011. **332**(6037): p. 1537-1541.
- [7] van Dover, R.B., L. Schneemeyer, and R. Fleming, *Discovery of a useful thin-film dielectric using a composition-spread approach*. Nature, 1998. **392**(6672): p. 162-164.
- [8] El-Kady, M.F., et al., *Laser scribing of high-performance and flexible graphene-based electrochemical capacitors*. Science, 2012. **335**(6074): p. 1326-1330.
- [9] Dubin, S., et al., *A one-step, solvothermal reduction method for producing reduced graphene oxide dispersions in organic solvents*. ACS Nano, 2010. **4**(7): p. 3845-3852.
- [10] Gong, X., et al., *A charge-driven molecular water pump*. Nature Nanotechnology, 2007. **2**(11): p. 709-712.
- [11] Gordillo, M. and J. Marti, *Hydrogen bond structure of liquid water confined in nanotubes*. Chemical Physics Letters, 2000. **329**(5): p. 341-345.
- [12] Brenner, D.W., et al., *A second-generation reactive empirical bond order (REBO) potential energy expression for hydrocarbons*. Journal of Physics: Condensed Matter, 2002. **14**(4): p. 783.
- [13] <http://www.vasp.at/>

- [14] <http://lammps.sandia.gov/>
- [15] Wu, X., et al., *Epitaxial-graphene/graphene-oxide junction: an essential step towards epitaxial graphene electronics*. Physical Review Letters, 2008. **101**(2): p. 026801.
- [16] Hwang, E. and S.D. Sarma, *Dielectric function, screening, and plasmons in two-dimensional graphene*. Physical Review B, 2007. **75**(20): p. 205418.
- [17] Moon, I.K., et al., *Reduced graphene oxide by chemical graphitization*. Nature Communications, 2010. **1**: p. 73.
- [18] Tung, V.C., et al., *High-throughput solution processing of large-scale graphene*. Nature Nanotechnology, 2008. **4**(1): p. 25-29.
- [19] Becerril, H.A., et al., *Evaluation of solution-processed reduced graphene oxide films as transparent conductors*. ACS Nano, 2008. **2**(3): p. 463-470.
- [20] Gao, W., et al., *Direct laser writing of micro-supercapacitors on hydrated graphite oxide films*. Nature Nanotechnology, 2011. **6**(8): p. 496-500.
- [21] Pech, D., et al., *Ultrahigh-power micrometre-sized supercapacitors based on onion-like carbon*. Nature Nanotechnology, 2010. **5**(9): p. 651-654.
- [22] El-Kady, M.F. and R.B. Kaner, *Scalable fabrication of high-power graphene micro-supercapacitors for flexible and on-chip energy storage*. Nature Communications, 2013. **4**: p. 1475.
- [23] Chmiola, J., et al., *Monolithic carbide-derived carbon films for micro-supercapacitors*. Science, 2010. **328**(5977): p. 480-483.
- [24] Lin, J., et al., *3-dimensional graphene carbon nanotube carpet-based microsupercapacitors with high electrochemical performance*. Nano Letters, 2012. **13**(1): p. 72-78.
- [25] Cai, W., et al., *Synthesis and solid-state NMR structural characterization of ¹³C-labeled graphite oxide*. Science, 2008. **321**(5897): p. 1815-1817.
- [26] Freitas, J.C., T.J. Bonagamba, and F.G. Emmerich, *Investigation of biomass-and polymer-based carbon materials using ¹³C high-resolution solid-state NMR*. Carbon, 2001. **39**(4): p. 535-545.
- [27] Wilkie, C.A., T.C. Ehlert, and D.T. Haworth, *A solid state ¹³C-NMR study of diamonds and graphites*. Journal of Inorganic and Nuclear Chemistry, 1978. **40**(12): p. 1983-1987.

- [28] Lerf, A., et al., *¹³C and ¹H MAS NMR studies of graphite oxide and its chemically modified derivatives*. Solid State Ionics, 1997. **101**: p. 857-862.
- [29] Lerf, A., et al., *Structure of graphite oxide revisited*. The Journal of Physical Chemistry B, 1998. **102**(23): p. 4477-4482.
- [30] Lerf, A., et al., *Hydration behavior and dynamics of water molecules in graphite oxide*. Journal of Physics and Chemistry of Solids, 2006. **67**(5): p. 1106-1110.
- [31] Buchsteiner, A., A. Lerf, and J.r. Pieper, *Water dynamics in graphite oxide investigated with neutron scattering*. The Journal of Physical Chemistry B, 2006. **110**(45): p. 22328-22338.
- [32] Zhang, Q., et al., *Anomalous Capacitive Behaviors of Graphene Oxide Based Solid State Supercapacitors*. Nano letters, 2014. **14**(4): p. 1938-1943.

Chapter 7

CONCLUSION AND FUTURE WORK

7.1 Summary of the Research Contributions

This dissertation covers the original work in the area of the self-discharge of ECs. Understanding the underlying self-discharge mechanisms is necessary and critical towards the potential applications of the self-discharge process. Concluded from the self-discharge research from Chapter 2 to Chapter 5 on various ECs built with ACF, SWNT and GO as electrodes, and different electrolytes from organic electrolytes to the GO based solid electrolyte, self-discharge mechanisms are determined by the structures of the ECs in terms of the accessible SSA and the charge transportation. High accessible SSA leads to high specific capacitance, *i.e.*, the large driving force of ionic concentration gradient $\partial c/\partial x$; while excellent charge transportation corresponds to a high initial voltage, *i.e.*, the large driving force of the potential field ΔE . The dominant mechanism of a self-discharge process is determined on the competition of the two driving forces. Therefore, ECs with a high initial voltage and a low specific capacitance tend to be dominated by the potential driving model; while ECs with a high specific capacitance and a low initial voltage tend to be dominated by the diffusion control model. Other factors such as the charge current density and the self-discharge temperature are irrelevant to the self-discharge mechanisms; however, they do affect certain characteristics of a self-discharge process, especially the self-discharging rate.

In Chapter 2, investigations of the self-discharge process of the ACF based ECs with different organic electrolytes demonstrate that the ACF-LiPF₆ EC is under the diffusion control; an interesting phenomenon has been observed for the ACF-TEABF₄ EC that the driving force changes during its self-discharge from ΔE to $\partial c/\partial x$. This observation leads to the proposal of a DM self-discharge model. The DM model indicates that self-discharge is an evolving process along with the competition between two driving forces. The ionic mobility difference between the two electrolytes leads to the variation in the self-discharge mechanisms between the ACF-LiPF₆ EC and the ACF-TEABF₄ EC. Moreover, up to 70% voltage retention has been obtained by the ACF-TEABF₄ EC for 36 hours, even at a high charge current density of 1000 mA·g⁻¹, indicating that this type of ECs are promising in serving as a highly reliable, fast-charging energy storage devices.

SWNT exhibits excellent electrical conductivity and charge transferring on the electrode/electrolyte interface compared to ACF. Therefore, as discussed in Chapter 3, ECs built with SWNT and the same electrolyte 1M TEABF₄/PC admit potential field dominating self-discharge processes. A division in the potential driving model, *i.e.*, the DPD model, has been discovered based on the self-discharge curve fitting, and confirmed to be resulted from the surface functional groups on the SWNT. The relation between the DPD model and the functional groups has been further demonstrated in Chapter 4. In Chapter 4, through tailoring the quantities of the functional groups (ranging from 22.1% to 8.9%), the self-discharge time required from 2.0V to 1.0 V is extended by 5 times. This is the first demonstration on the tunability of the self-discharge. Through realizing control over the self-discharge process, designing ECs for specific energy retention requirements could be addressed.

Chapter 5 demonstrates that partially reduced LR-GO films can be used as solid-state ECs with self-contained water and functional groups as electrolyte. By successfully applying the DPD model to the LR-GO ECs with highly restricted ionic mobility, *i.e.*, the small $\partial c/\partial x$ compared to the mediocre ΔE , the proposed relation between the EC structures and the self-discharge models is extended to solid-state ECs, as well as the relation between the functional groups and the DPD model. Self-discharge study in Chapter 5 on the LR-GO ECs indicates the applicability of the proposed mechanisms to broader types of ECs.

Chapter 6 presents another GO based solid-state capacitor with a sandwiched structure (rGO/GO/rGO), which exhibits anomalous capacitive behaviors of considerable specific capacitance yet dismissible ionic diffusion that cannot be defined as either a DC or an EC. Systematical characterizations have been applied on the sandwiched GO film. DFT and MD simulations have been used to investigate the sandwiched GO film. Based on the results, the Charge Close-Packed model has been proposed to explain the charge storage mechanism in the sandwiched GO films. The primary characteristic of this model include the nanoscaled ionic diffusion as localized by the layered structures and the poor ionic mobility. The Charge Close-Packed model breaks the conventional definitions on ECs and DCs, and has fundamental meanings for future research on establishing, even re-defining the boundary conditions between different types of electric capacitors.

7.2 Future Work

The self-discharge of ECs is a relatively new topic in the area of energy storage but is highly important. This dissertation covers from understanding the underlying mechanisms to several attempts for the practical applications of carbon

materials based ECs. The critical point and purpose of self-discharge study is to control the self-discharge for desired energy retentions for various applications. We have demonstrated that the ACF-TEABF₄ EC can hold 70% of the charge voltage for 36 hours; though for many potential applications, higher energy retention for a longer time may be required. Therefore, it is important to search for an EC structure which can possess a longer self-discharge time. With the incomparable advantages in the high power density and the ultra-long service life, ECs with superior energy retention will be a promising competitor in the market of energy storage devices.

On the other hand, as demonstrated in Chapter 4, self-discharge process can be tuned; therefore, another promising direction on the self-discharge research is to realize precise control on the self-discharge rate, *i.e.*, the accurate prediction of the voltage value after a certain self-discharge time (even down to micro seconds). This research should benefit widely in electric circuit design, where precise control on the signal response is preferred other than high voltage or energy.

It has been confirmed that different electrolytes will lead to different self-discharge models. Therefore, fundamental research on how electrolytes affect the self-discharge mechanisms is another important topic. Factors such as the size of electrolytic ions, the viscosity of the solvents, and the ionic mobility of the electrolytes should be investigated in terms of their effects on the self-discharge mechanisms of the ECs. This fundamental research could provide vital information for designing ECs with desired energy retention.

As a transitional state between conventional ECs and DCs, CCP model proposed based on the sandwiched GO capacitor film fills the seemingly insurmountable gap between ECs and DCs. However, on which critical point can the

CCP model based on the sandwiched GO film change to a conventional double layer structures as in ECs is still unclear. Fundamental research on investigating the boundary conditions between the ECs and the CCP model, as well as between the CCP model and the DCs, would be an exciting challenge to conquer.

Appendix A

SCIENTIFIC AND TECHNICAL CONTRIBUTIONS DURING PH.D.

Published Papers

1. **Q. Zhang**, K. Scrafford, M. Li, Z.Y. Cao, Z. Xia, P.M. Ajayan, B.Q. Wei, Anomalous Capacitive Behaviors of Graphene Oxide Based Solid State Supercapacitors, *Nano Letters*, 14(4), 1938-1943 (2014).
2. **Q. Zhang**, C. Cai, J.W. Qin, B.Q. Wei, Tunable Self-discharge Process of Carbon Nanotube Based Supercapacitors, *Nano Energy*, 4, 14-22 (2014).
3. K. Liang, N. Wang, M. Zhou, Z.Y. Cao, T. Gu, **Q. Zhang**, X. Tang, W. Hu, B.Q. Wei, Mesoporous LaNiO₃/NiO Nanostructured Thin Films for High-performance Supercapacitors. *Journal of Materials Chemistry A*, 1, 9730-9736 (2013).
4. J.W. Qin, **Q. Zhang**, Z. Y. Cao, X. Li, C.W. Hu, and B.Q. Wei, MnOx/SWCNTs Macro-film as Flexible Binder-free Anodes for High-performance Li-ion Batteries. *Nano Energy*, 4, 733-741 (2012).
5. W. Gao, N. Singh, L. Song, Z. Liu, A.L.M. Reddy, L. Ci, R. Vajtai, **Q. Zhang**, B.Q. Wei, and P.M. Ajayan, Direct Laser Writing of Micro-supercapacitors on Hydrated Graphite Oxide Films. *Nature Nanotechnology*, 6, 496-500 (2011).
6. Y. Chen, C. Li, Y.G. Wang, **Q. Zhang**, C.Y. Xu, B.Q. Wei, and L.N. An, Self-assembled Carbon–silicon Carbonitride Nanocomposites: High-performance Anode Materials for Lithium-ion Batteries. *Journal of Material Chemistry*, 21, 18186-18190 (2011).
7. **Q. Zhang**, J. Rong, B.Q. Wei, A Divided Potential Driving Self-discharge Process for Single-Walled Carbon Nanotube Based Supercapacitors. *RSC Advances*, 1(6), 989-994 (2011).
8. **Q. Zhang**, J. Rong, D. Ma, B.Q. Wei, The Governing Self-discharge Process in Activated Carbon Fabric-based Supercapacitors with Different Organic Electrolytes. *Energy & Environmental Science*, 4, 2152-2159 (2011).

Appendix B

AWARDS DURING PH.D.

1. Professional Development Award, University of Delaware (2013)
2. Student Travel Grant, Battery Division of the Electrochemical Society Biannual Meeting (2013)
3. Graduate Student Fellowship, NSF CMMI Engineering Research and Innovation Conference (2012)

Appendix C

PERMISSION LETTERS

1. Reprinted permission for Figure 1.4d.

HomeAccount InfoHelp



Title: Supercapacitors from Activated Carbon Derived from Banana Fibers
Author: V. Subramanian et al.
Publication: The Journal of Physical Chemistry C
Publisher: American Chemical Society
Date: May 1, 2007
Copyright © 2007, American Chemical Society

Logged in as:
Qing Zhang
Account #:
3000769290

Logout

PERMISSION/LICENSE IS GRANTED FOR YOUR ORDER AT NO CHARGE

This type of permission/license, instead of the standard Terms & Conditions, is sent to you because no fee is being charged for your order. Please note the following:

- Permission is granted for your request in both print and electronic formats, and translations.
- If figures and/or tables were requested, they may be adapted or used in part.
- Please print this page for your records and send a copy of it to your publisher/graduate school.
- Appropriate credit for the requested material should be given as follows: "Reprinted (adapted) with permission from (COMPLETE REFERENCE CITATION). Copyright (YEAR) American Chemical Society." Insert appropriate information in place of the capitalized words.
- One-time permission is granted only for the use specified in your request. No additional uses are granted (such as derivative works or other editions). For any other uses, please submit a new request.

If credit is given to another source for the material you requested, permission must be obtained from that source.

BACKCLOSE WINDOW

Copyright © 2014 [Copyright Clearance Center, Inc.](#) All Rights Reserved. [Privacy statement.](#) Comments? We would like to hear from you. E-mail us at customer@copyright.com

2. Reprinted permission for Figure 1.4e.

Home Account Info Help



Title: Rapid growth of well-aligned carbon nanotube arrays
Author: Xianfeng Zhang, Anyuan Cao, Bingqing Wei, Yanhui Li, Jinqun Wei, Cailu Xu, Dehai Wu
Publication: Chemical Physics Letters
Publisher: Elsevier
Date: 19 August 2002
Copyright © 2002, Elsevier

Logged in as:
Qing Zhang
Account #: [3000769290](#)
Logout

Order Completed
Thank you very much for your order.

This is a License Agreement between Qing Zhang ("You") and Elsevier ("Elsevier"). The license consists of your order details, the terms and conditions provided by Elsevier, and the [payment terms and conditions](#).

[Get the printable license.](#)

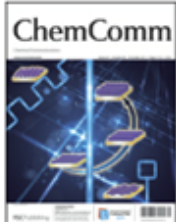
| | |
|----------------------------------------------|-------------------------------------------------------------------------------------|
| License Number | 3366000150337 |
| License data | Apr 11, 2014 |
| Licensed content publisher | Elsevier |
| Licensed content publication | Chemical Physics Letters |
| Licensed content title | Rapid growth of well-aligned carbon nanotube arrays |
| Licensed content author | Xianfeng Zhang, Anyuan Cao, Bingqing Wei, Yanhui Li, Jinqun Wei, Cailu Xu, Dehai Wu |
| Licensed content date | 19 August 2002 |
| Licensed content volume number | 362 |
| Licensed content issue number | 3-4 |
| Number of pages | 6 |
| Type of Use | reuse in a thesis/dissertation |
| Portion | figures/tables/illustrations |
| Number of figures/tables/illustrations | 1 |
| Format | both print and electronic |
| Are you the author of this Elsevier article? | No |
| Will you be translating? | No |
| Title of your thesis/dissertation | Self-discharge of Carbon Materials-based Electrochemical Capacitors |
| Expected completion date | Apr 2014 |
| Estimated size (number of pages) | 170 |
| Elsevier VAT number | GB 494 6272 12 |
| Permissions price | 0.00 USD |
| VAT/Local Sales Tax | 0.00 USD / 0.00 GBP |
| Total | 0.00 USD |

ORDER MORE... CLOSE WINDOW

Copyright © 2014 [Copyright Clearance Center, Inc.](#) All Rights Reserved.
[Privacy statement.](#)
Comments? We would like to hear from you. E-mail us at customercare@copyright.com

3. Reprinted permission for Figure 3.1c.

Home Account Info Help



Title: Direct fabrication of single-walled carbon nanotube macro-films on flexible substrates
Author: Hongwei Zhu, Bingqing Wei
Publication: Chemical Communications (Cambridge)
Publisher: Royal Society of Chemistry
Date: Apr 20, 2007
Copyright © 2007, Royal Society of Chemistry

Logged in as:
Qing Zhang
Account #: [3365990052958](#)
[Logout](#)

Order Completed

Thank you very much for your order.

This is a License Agreement between Qing Zhang ("You") and Royal Society of Chemistry. The license consists of your order details, the terms and conditions provided by Royal Society of Chemistry, and the [payment terms and conditions](#).

[Get the printable license.](#)

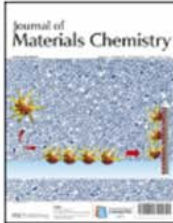
| | |
|----------------------------------|----------------------------------------------------------------------------------------|
| License Number | 3365990052958 |
| License date | Apr 11, 2014 |
| Licensed content publisher | Royal Society of Chemistry |
| Licensed content publication | Chemical Communications (Cambridge) |
| Licensed content title | Direct fabrication of single-walled carbon nanotube macro-films on flexible substrates |
| Licensed content author | Hongwei Zhu, Bingqing Wei |
| Licensed content date | Apr 20, 2007 |
| Issue number | 29 |
| Type of Use | Thesis/Dissertation |
| Requestor type | publisher |
| Portion | figures/tables/images |
| Number of figures/tables/images | 1 |
| Distribution quantity | 500 |
| Format | print and electronic |
| Will you be translating? | no |
| Order reference number | |
| Title of the thesis/dissertation | Self-discharge of Carbon Materials-based Electrochemical Capacitors |
| Expected completion date | Apr 2014 |
| Estimated size | 170 |
| Total | 0.00 USD |

[ORDER MORE...](#) [CLOSE WINDOW](#)

Copyright © 2014 [Copyright Clearance Center, Inc.](#) All Rights Reserved.
[Privacy statement.](#)
Comments? We would like to hear from you. E-mail us at customercare@copyright.com

4. Reprinted permission for Figure 3.1d.

Home Account Info Help



Title: Tearing open nitrogen-doped multiwalled carbon nanotubes
Author: Mark S. Meier,Rodney Andrews,David Jacques,Kelby B. Cassity,Dali Qian
Publication: Journal of Materials Chemistry
Publisher: Royal Society of Chemistry
Date: Aug 5, 2008
Copyright © 2008, Royal Society of Chemistry

Logged in as:
Qing Zhang
Account #: 3000769290
[LOGOUT](#)

Order Completed

Thank you very much for your order.

This is a License Agreement between Qing Zhang ("You") and Royal Society of Chemistry. The license consists of your order details, the terms and conditions provided by Royal Society of Chemistry, and the [payment terms and conditions](#).

[Get the printable license.](#)

| | |
|----------------------------------|-----------------------------------------------------------------------|
| License Number | 3365991511465 |
| License date | Apr 11, 2014 |
| Licensed content publisher | Royal Society of Chemistry |
| Licensed content publication | Journal of Materials Chemistry |
| Licensed content title | Tearing open nitrogen-doped multiwalled carbon nanotubes |
| Licensed content author | Mark S. Meier,Rodney Andrews,David Jacques,Kelby B. Cassity,Dali Qian |
| Licensed content date | Aug 5, 2008 |
| Volume number | 18 |
| Issue number | 35 |
| Type of Use | Thesis/Dissertation |
| Requestor type | publisher |
| Portion | figures/tables/images |
| Number of figures/tables/images | 1 |
| Distribution quantity | 500 |
| Format | print and electronic |
| Will you be translating? | no |
| Order reference number | |
| Title of the thesis/dissertation | Self-discharge of Carbon Materials-based Electrochemical Capacitors |
| Expected completion date | Apr 2014 |
| Estimated size | 170 |
| Total | 0.00 USD |

[ORDER MORE...](#) [CLOSE WINDOW](#)

Copyright © 2014 [Copyright Clearance Center, Inc.](#) All Rights Reserved.
[Privacy statement.](#)
Comments? We would like to hear from you. E-mail us at customercare@copyright.com